1-1-2011

Improving the Dispersive Optical Model toward a Dispersive Self-energy Method

Seth Waldecker
Washington University in St. Louis

WASHINGTON UNIVERSITY

Department of Physics

Dissertation Examination Committee:
Willem H. Dickhoff Chair
Mark Alford
R.J. Charity
Michael C. Ogilvie
Demetrios G. Sarantites
Lee G. Sobotka

Improving the Dispersive Optical Model toward a Dispersive Self-energy Method

by

Seth Waldecker

A dissertation presented to the
Graduate School of Arts and Sciences
of Washington University in
partial fulfillment of the
requirements for the degree
of Doctor of Philosophy

December 2011

Saint Louis, Missouri

ABSTRACT OF THE DISSERTATION

Improving the Dispersive Optical Model toward a Dispersive Self-energy Method

by

Seth Waldecker

Doctor of Philosophy in Physics

Washington University in St. Louis, 2011

Professor Willem H. Dickhoff, Chairperson

The connection between the dispersive optical potential and the irreducible nucleon self-energy from Green's function theory is improved, providing a tighter link between nuclear reactions and nuclear structure. In particular, since the self-energy is inherently nonlocal, an explicitly nonlocal term is incorporated in the real part of the dispersive optical potential, which has been assumed to be local in previous parametrizations. The explicit treatment of nonlocality allows for a proper solution of the Dyson equation, and the resulting propagator can then be used to calculate experimental observables associated with ground state properties, such as the charge density, particle number, and the energy per particle. Comparison of these quantities with data suggests additional ways in which the dispersive optical model can be improved. For example, a better treatment of short-range correlations is needed, and explicitly including the nonlocality of the imaginary potential appears to be necessary for particle number conservation. Comparison of the dispersive optical potential with microscopic calculations of the self-energy is also made and suggests further improvements. Thus, increasing the correspondence between the potential from the dispersive optical model and the self-energy increases the amount of feedback from theory and experiment and provides a method for systematically improving the description of the empirical self-energy for both stable and rare isotopes. The dispersive optical model is also applied to transfer reactions, which are proving to be a useful tool for studying the nuclear structure of rare isotopes.

Acknowledgements

I am very grateful for Wim Dickhoff, whose patience and guidance, along with his expertise and enthusiasm for many-body physics, have greatly contributed to making my time in graduate school a positive experience. His investment in my education has been invaluable.

I would like to thank Mark Alford, Bob Charity, Demetrios Sarantites, Lee Sobotka and Li Yang for being on my committee. I would particularly like to thank Bob Charity, who helped me considerably with my work, and Lee Sobotka, for his helpful advice and feedback. I would also like to thank those who have been a part of the nuclear physics group. Our group meetings and informal discussions have been an important part of my growth as a physicist.

Over the years I have collaborated with a number of people. I would like to thank Carlo Barbieri for providing his FRPA calculations and his time. I would also like to acknowledge the support from the JUSTIPEN program and the hospitality of RIKEN, both of which made my collaboration with Carlo Barbieri possible.

I give thanks to Filomena Nuñes and Ngoc Nguyen for inviting me to collaborate with them and for receiving me well at Michigan State University. I give thanks to Arturo Polls and Herbert Müther for providing their $\mathcal{G}$-matrix calculations and to Helber Dussan for his assistance in the analysis of these calculations. My research could not have been possible without the financial support of the university and the National Science Foundation.

The support from family and friends has been essential during my time in graduate school. I am especially grateful for my father, Gary, my mother, Phyllis, and my siblings, Micah, Andrea and Audrey. They are a constant source of encouragement and joy in my life. I have made many good friends here in St. Louis. For lack of space and for fear of leaving someone out I shall refrain from mentioning names, but know that you all are dear to my heart. My professors from my undergraduate institution, Don Petcher and Phil Broussard, have continued to provide guidance and encouragement, for which I am grateful.

I would like to give the greatest thanks to Jesus Christ, my Lord and my God, who has guided me through every step in graduate school and in all my life. He has been teaching me to have both a joyful and humble attitude during times of frustration and during times of success.

Contents

Abstract **iii**

Acknowledgements **iv**

List of Figures **x**

List of Tables **xi**

1 Introduction **1**

2 Formalism **7**
2.1 Introduction 7
2.2 Propagator Formalism 7
2.2.1 Hamiltonian 7
2.2.2 The Propagator of a Many-Body System and its Relation to Experimental Quantities. 9
2.2.3 Perturbation Expansion 12
2.2.4 The Irreducible Self-energy and the Dyson Equation 14
2.2.5 Propagator in Coordinate Space 19
2.3 DOM Formalism 21
2.3.1 Dispersion Relation 22
2.3.2 Local-equivalent Potential 23
2.3.3 Parametrization of the Self-energy 24
2.3.4 Solution of the Dyson Equation 26

3 Nonlocality in the DOM **29**
3.1 Procedure 30
3.1.1 Nonlocal Hartree-Fock Term 31
3.1.2 Fitting 32
3.2 Results for ^{40}Ca 33
3.2.1 Spectral Strength 34
3.2.2 Comparison of Quasiparticle Properties 36
3.2.3 Charge Distribution 41
3.2.4 High-momentum Content in the DOM 42
3.2.5 Binding Energy per Particle 48

3.3 Other Isotopes . . . 49
3.3.1 Extrapolations . . . 49
3.3.2 Other Ground-state Properties . . . 62
3.4 Beyond Nonlocal HF Description . . . 63

4 DOM and Transfer Reactions 68
4.1 Introduction . . . 68
4.2 ADWA . . . 69
4.3 Link with DOM . . . 71
4.4 Results . . . 71
4.4.1 Details of the calculations . . . 71
4.4.2 Transfer Cross Sections . . . 75
4.4.3 Spectroscopic Factors . . . 84
4.5 Conclusions . . . 86

5 FRPA and DOM 88
5.1 Ingredients of the FRPA . . . 89
5.2 Connecting the DOM and FRPA Self-energies . . . 92
5.3 Calculation Details . . . 96
5.4 Results . . . 97
5.4.1 Angular-Momentum Dependence . . . 97
5.4.2 Parity Dependence . . . 105
5.4.3 Asymmetry Dependence . . . 109
5.4.4 Analysis of radial dependence . . . 113
5.5 Conclusions . . . 117

6 Including SRC in DOM 119
6.1 Details of the Microscopic Calculation . . . 119
6.1.1 Solution of the Dyson Equation . . . 122
6.2 Results . . . 125
6.2.1 Spectral Functions . . . 125
6.2.2 Quasiholes and quasiparticles . . . 131
6.2.3 Momentum Distribution . . . 133
6.2.4 Natural Orbits . . . 137
6.2.5 Charge Distribution . . . 144
6.2.6 Ground-state Energy . . . 145
6.2.7 Analysis of CDBonn self-energy . . . 148
6.3 Conclusions . . . 153

7 Summary and Outlook 156

Bibliography 165

List of Figures

2.1 a) The first-order diagram in the perturbation expansion of the propagator and b) an example of a second-order diagram. 14
2.2 a) HF b) 2p1h c) 2h1p intermediate states. 15
2.3 Expansion of the propagator in terms of the irreducible self-energy Σ^*. The double line represents the full propagator, and the single line represents the unperturbed propagator. 16
2.4 Propagator in terms of the self-consistent self-energy diagrams. 17
2.5 Examples of the energy dependence of the volume (black) and surface (red) terms of the imaginary part of the DOM potential. 26

3.1 Comparison of proton $s_{1/2}$ spectral strength with the nonlocal (solid) and local potential with the spurious energy dependence (dashed). . . 35
3.2 Spectral functions for all mostly occupied ℓj combinations in ^{40}Ca together with the $f_{7/2}$ result. 37
3.3 $S_{n\ell j}(E)$ for the proton $0s_{1/2}$ in ^{40}Ca (red) with the peak fitted by a Gaussian (black). 41
3.4 Experimental charge density of ^{40}Ca (solid) compared with the DOM result (dashed). 43
3.5 Comparison of the total momentum distribution calculated according to Eq. (3.17) (dashed) with the one obtained from the quasihole contributions (solid). 45
3.6 Momentum-space spectral function for $d_{3/2}$ quantum numbers at different energies. 46
3.7 Momentum-space spectral function for $s_{1/2}$ quantum numbers at energies corresponding to the ones used in Fig. 47
3.8 Spectroscopic factors for the valence holes of the minority species in the Ca isotopes obtained from experiment (circles), nonlocal DOM (squares) and local DOM (diamonds). The points to the left of the dashed vertical line are for the neutron holes in ^{36}Ca. 52
3.9 Schematic level diagrams illustrating the effect of the continuum on the strength of the absorption below the Fermi energy. 53
3.10 Spectroscopic factor of the neutron $1s_{1/2}$ hole state of ^{36}Ca as function of Δ, the energy interval between the threshold energy for the imaginary potential at negative energies and the $1s_{1/2}$ hole state. . . 54

3.11 Spectral strength of the neutron $1s_{1/2}$ hole state of ^{36}Ca for different values of Δ. 55
3.12 Comparison of energy levels of neutrons in ^{133}Sn obtained experimentally and with the DOM. The spectroscopic factors obtained with FR-ADWA-CH and the local DOM are also compared. 59
3.13 *Top Panel*: sp neutron states above the ^{208}Pb core. *Bottom Panel*: sp neutrons states above the ^{132}Sn core. In each panel, the levels are labeled on the left and the corresponding spectroscopic factors are given on the right. 65
3.14 Strength functions of the $0g_{9/2}$ proton orbit in different Sn isotopes obtained with the nonlocal calculations. 66
3.15 *Top Panel*: Experimental ^{124}Sn charge density (solid red) compared with the nonlocal DOM result (dashed blue). *Bottom Panel*: Experimental ^{208}Pb charge density (solid red) compared with the nonlocal DOM result (dashed blue). 67

4.1 Comparison of the square of the single-neutron overlap functions for ^{41}Ca obtained with a Woods-Saxon potential φ_{WS} (solid), with the local DOM corrected for nonlocality $\bar{\varphi}$ (dashed), and with the DOM containing nonlocal HF term φ_{NL} (dot-dashed). 73
4.2 Same as in Fig. 4.1, but for ^{49}Ca. 74
4.3 Angular distributions are shown for the reaction ^{40}Ca$(d,p)^{40}$Ca at $E_d =$ 20 MeV. Theory predictions have been normalized to the data at the peak. 76
4.4 Angular distributions are shown for the reaction ^{40}Ca$(d,p)^{40}$Ca at $E_d =$ 56 MeV. 77
4.5 Angular distributions are shown for the reaction ^{48}Ca$(d,p)^{49}$Ca at $E_d =$ 2 MeV. 78
4.6 Angular distributions are displayed for the reaction ^{48}Ca$(d,p)^{49}$Ca at $E_d = 19.3$ MeV. 79
4.7 Angular distributions for the reaction ^{48}Ca$(d,p)^{49}$Ca at $E_d = 56$ MeV are displayed. 80
4.8 Angular distributions for the ^{132}Sn$(d,p)^{133}$Sn reaction at a deuteron energy of $E_d = 9.46$ MeV are shown normalized at the peak of the experimental cross section. 81
4.9 Angular distributions for the ^{208}Pb$(d,p)^{209}$Pb reaction are shown at a deuteron energy of $E_d = 20$ MeV and normalized at the peak of the experimental data. 82
4.10 Comparison of the CH89 (solid) and the purely local DOM (dashed) optical potentials for n-^{132}Sn (red) and p-^{132}Sn (blue) at an energy of 4.7 MeV (half the deuteron energy). The real component is shown in panel (a) and the imaginary component in panel (b). 83

5.1 The self-energy $\Sigma^\star(E)$ separates exactly into a static (mean-field) term, Σ^∞, and the polarization propagators $R^{(2p1h/2h1p)}(E)$ for the 2p1h/2h1p motion. 89
5.2 Expansion of the ph propagator $\Pi(E)$ in a series of ring diagrams. . . 90
5.3 Example of one of the diagrams for $R^{(2p1h)}(E)$ that are summed to all orders by means of the Faddeev method. Each of the ellipses represent an infinite sum of rings ($\Pi(E)$) or ladders ($g^{II}(E)$). 91
5.4 Imaginary volume integral $J_W^\ell(E)$ of the ^{48}Ca self-energy calculated with model spaces of different sizes.The top (bottom) panels refer to the scattering of a neutron with angular momentum ℓ=1 (ℓ=3). Dashed, dot-dashed and full lines refer to model spaces of 6, 8, and 10 oscillator shells, respectively. 98
5.5 Angular momentum dependence for the volume integrals $J_V^\ell(\varepsilon_F)$ (solid squares), J_F^ℓ (diamonds) and $J_{HF}^{DOM,\ell}$ (circles), which should be compared with $J_V^\ell(\varepsilon_F)$. The results shown are for neutrons in ^{40}Ca. . . . 99
5.6 Separate partial wave contributions of J_W averaged over ℓ-channels with 4 (solid), 3 (long-dashed), 2 (dot-dashed), and 1 (short-dashed) harmonic-oscillator orbits in the model space. 100
5.7 Imaginary volume integrals of the volume part of a DOM self-energy with a local Woods-Saxon form factor replaced by a nonlocal form proposed by Perey and Buck. 101
5.8 The FRPA results for the average over all ℓ-channels (dashed) are compared with the DOM result (solid), corrected for nonlocality. . . . 103
5.9 Volume Integrals of Re Σ_0^ℓ for neutrons in ^{40}Ca. The horizontal, dashed lines are the volume integrals of $\Sigma_0^{\infty,\ell}(\varepsilon_F)$. 104
5.10 Comparison of the FRPA (red) and DOM (blue) subtracted dispersive corrections. 106
5.11 J_W averaged over even ℓ-channels (solid) is compared with Jw averaged over odd ℓ-channels (dashed). 107
5.12 $J_D^\ell(E)$ for $\ell = 0$ (black) and $\ell = 1$ (red) for neutrons in ^{40}Ca. 108
5.13 Asymmetry dependence of the absorption for neutrons and protons and dependence on tensor correlations. 109
5.14 Effect of the tensor force and charge exchange on correlations on the proton-^{48}Ca self-energy. 111
5.15 Diagonal part of FRPA imaginary self-energy for protons at $E-\varepsilon_F$=44 MeV (solid) and the corresponding parametrized self-energy (dashed). 115
5.16 *Left panels:* FRPA imaginary self-energy integrated over r' for protons in ^{40}Ca (solid), ^{48}Ca (dashed), ^{60}Ca (dot-dashed). *Right panels:* For comparison, the DOM imaginary potentials at the same energy are shown for ^{40}Ca and ^{48}Ca. 116

6.1 Graphical representation of the BHF (a), the two-particle–one-hole contribution (b) and one-particle–two-hole term (c) to the self-energy of the nucleon. 121
6.2 Momentum-space spectral function for neutron $d_{3/2}$ quantum numbers at different energies in ^{40}Ca. 126
6.3 Comparison of spectral functions from present work shown in panel (a) with those from a DOM analysis using a nonlocal potential in panel (b). 127
6.4 Momentum distribution for neutrons in ^{40}Ca weighted by k^2. 134
6.5 CDBonn momentum distribution with $\ell_{max} = 3$ (dashed) and $\ell_{max} = 4$ (solid) compared with the DOM result including all partial waves including $f_{7/2}$ (dash-dot) 135
6.6 Quasihole contribution to the momentum distribution for the CDBonn (solid) compared to the DOM result (dashed). 136
6.7 Comparison of wave functions for the $s_{1/2}$ quasihole result (solid) and the corresponding natural orbit (dashed) without a node. 139
6.8 As in Fig. 6.7 but showing $s_{1/2}$ wave functions with one node. 140
6.9 As in Fig. 6.7, but with the corresponding $d_{3/2}$ wave functions. 141
6.10 Occupation numbers of natural orbits that are fully occupied in the IPM. Results are shown for the CDBonn calculation (diamonds), the DOM calculation (circles) 143
6.11 Charge density distribution for ^{40}Ca from the CDBonn self-energy (dashed) compared to experiment (solid). 146
6.12 Diagonal part of CDBonn imaginary self-energy at 65 MeV (solid), and the corresponding parametrized self-energy (dashed). 149
6.13 CDBonn imaginary self-energy at 65 MeV integrated over r' (solid), and the corresponding integrated parametrized self-energy (dashed). . 150
6.14 Imaginary volume integrals for the CDBonn self-energy at 65 MeV (circles), and the corresponding result for the parametrized self-energy (squares). 151
6.15 Imaginary volume integrals for the CDBonn self-energy as a function of energy for different ℓ-values. 153

List of Tables

3.1 Parameters for the local energy-dependent Woods-Saxon potential and the nonlocal version with gaussian nonlocality for ^{40}Ca. 34
3.2 Quasihole energies for proton orbits in ^{40}Ca for the local and nonlocal DOM implementation compared with experiment. 38
3.3 Spectroscopic factors for proton orbits in ^{40}Ca for the local and nonlocal DOM implementation. 39
3.4 Spectroscopic factors for the proton and neutron valence hole levels in ^{36}Ca. 51
3.5 Energy levels for sp neutron levels in ^{133}Sn. Energies are in MeV . . . 58
3.6 Spectroscopic factors for sp neutron levels in ^{133}Sn. 58
3.7 Spectroscopic factors (relative to the IPM predictions) and occupation numbers n for the $0g_{9/2}$ proton orbit in Sn isotopes using the nonlocal (NL) and local (L) versions of the DOM. 62
3.8 Binding energies per particle for various isotopes. 63

4.1 Properties of overlap functions with a comparison among φ_{WS}, $\bar{\varphi}$, and φ_{NL}. 72
4.2 Spectroscopic factors obtained from the FR-ADWA analysis. The deuteron kinetic energy E_d (lab. frame) is in MeV. 84

5.1 Particle-Hole Gaps in MeV. 105
5.2 Parameters from nonlocal fits to the imaginary part of the proton self-energy at $E - \varepsilon_F$=44 MeV for ^{40}Ca, ^{48}Ca, and ^{60}Ca. 114

6.1 Neutron sp strength for the various ℓj combinations. 129
6.2 Neutron sp strength for different ℓ states up to $\ell = 3$. 131
6.3 Quasihole energies for neutron orbits in ^{40}Ca. 132
6.4 Quasihole spectroscopic factors and occupation numbers for the CD-Bonn self-energy compared to the corresponding DOM results. 132
6.5 Occupation numbers of natural orbits. 142
6.6 Occupation numbers of natural orbits calculated with the DOM. . . . 142
6.7 Parameters from nonlocal fits to the imaginary part of the proton self-energy at different energies. 152

7.1 Summary Table 158

Chapter 1

Introduction

An important goal in the study of nuclear physics is understanding the single-particle (sp) motion of a nucleon in the presence of other nucleons, *i.e.* in a medium as opposed to in the vacuum. Because the nucleon-nucleon interaction is strong, the propagation of a particle in the medium is strongly correlated with the motion of all the other particles. Nonetheless, the independent particle model (IPM), which pictures the nucleons moving independently of each other inside a common potential, has had success in explaining the shell structure of nuclei and the appearance of magic numbers [1]. Hence, the IPM is also referred to as the simple shell model. The common potential can be interpreted as the average effect of a nucleon's interactions with all the other nucleons. For this reason, this potential is also referred to as the mean field.

However, the IPM is not able to account for certain experimental results. In particular, $(e, e'p)$ experiments [2–5] have clearly demonstrated that the sp strength of particular shell model orbitals is *fragmented* over several energies, whereas according to the IPM, the sp strength should be found at only one energy. A consequence of this fragmentation is that the probability for removing a particle from a state that is filled in the IPM can be less than one, whereas the IPM predicts a removal probability of 1. For energy levels near the Fermi energy, the bulk of the sp strength is concentrated at one energy, but is still reduced by 30-40% with respect to the IPM [5, 6]. For the

more deeply bound states the sp strength is distributed over a much wider range of energies. Thus, for the deeply bound states the notion of an independent particle loses its meaning.

This reduction of sp strength is a clear indication of the importance of correlations beyond the mean field. These correlations can be classified into two categories. Long-range correlations (LRC) are responsible for the coupling of a particle to low-lying excitations and giant resonances. Short-range correlations (SRC) become important at high excitation energies when the relative momentum between two nucleons is high enough for the nucleons to experience the repulsive core of the nucleon-nucleon interaction. These correlations are responsible for the presence of high-momentum components in the ground state of nuclei [7]. The effects of both LRC and SRC are needed to quantitatively explain the reduction observed in $(e, e'p)$ experiments [8, 9]. LRC cause a depletion of about 20% for orbits near the Fermi energy, while SRC cause a global depletion of 10-15%.

An important topic that is currently much discussed in the field [10, 11] is how nuclear correlations change with neutron-proton asymmetry. Nuclei far from stability, or rare isotopes, are sometimes referred to as exotic nuclei because they often exhibit phenomena unobserved in stable isotopes. The existence of halo nuclei [12] and the appearance of new magic numbers [13] are just two examples of the very different properties of nuclei at the extremes of stability. These differences have posed challenges for theoretical nuclear physics, and one of the main goals within the field of nuclear physics worldwide is to understand their origin.

One of the motivations for this goal is to gain a greater fundamental understanding of the nuclear many-body problem and the strong interaction. Another motivation is to understand the formation of elements heavier than ^{56}Fe. Some of these elements are believed to be formed in supernovae by neutrons being captured onto seed nuclei, such as ^{56}Fe. The rapid neutron-capture process (r-process) is one way that this accretion can take place and occurs when the rate of neutron capture is faster than the rate of beta decay. Once the neutron number reaches a certain point, however,

an added neutron will become particle unbound, and the neutron rich nucleus will begin decaying to stability. This limit in neutron number is known as the neutron drip line and is an important factor in the production of heavy elements. There is also a proton drip line.

Currently, neutron drip-lines are known only for light nuclei, such as Li, He, and O [14]. Therefore, for the heavier nuclei, astrophysical calculations presently rely on extrapolations. A good understanding of the neutron-proton asymmetry dependence is then essential for predicting the properties of exotic nuclei for which there are currently no experimental data.

Some of the experiments relevant for studying the sp properties of nuclei, besides $(e, e'p)$ reactions, are neutron and proton elastic-scattering reactions and transfer reactions in which a single nucleon is added to or removed from the target nucleus. The first kind of experiments primarily probe the scattering states of the target nucleus and can be used to study the nucleon-nucleus interaction at positive energies. The second kind of experiments probe the bound states of the target nucleus and can be used to study the nucleon-nucleus interaction at negative energies.

Data from elastic scattering experiments are most often analyzed with optical potentials, which parametrize the effective interaction between the projectile and the target with real and imaginary parts. The imaginary part models the absorption of particles into inelastic channels, and there is unambiguous evidence that the imaginary part is important for describing the experimental cross-sections [15–17]. This observation further points to the importance of correlations and demonstrates the limitation of the simple shell-model, which is real and independent of energy.

Important transfer reactions for the study of exotic nuclei are the (d, p) and (p, d) reactions. In the first reaction, a deuteron (d) incident on a target transfers a neutron to the target, and the outgoing proton (p) is detected. In the second, a neutron is removed. Employing these reactions in inverse kinematics provides a way to study neutron states in unstable nuclei. Optical potentials are also often used to analyze transfer reactions, but the optical potentials for probes with $A > 1$, where A is the

number of nucleons, are more difficult to interpret than nucleon optical potentials. However, the adiabatic distorted wave approximation (ADWA) [18] has allowed for the use of nucleon optical-potentials for the description of the interaction of the deuteron with the target in both (d, p) and (p, d) reactions [19, 20].

One of the drawbacks of most optical potentials is they cannot simultaneously describe both scattering and bound-state data. As a result, they cannot be used to reliably predict nuclear structure, which is essential for drip-line physics. This shortcoming also affects the analysis of transfer reactions since the overlap functions for adding or removing a neutron are needed and cannot be provided by the optical potentials. Therefore, there is a need for a better link between nuclear reactions and nuclear structure.

In principle, data from scattering experiments also yield information about bound-state data because of the coupling of sp degrees of freedom with core excited states, such as particle-hole (ph) excitations. In Green's function theory, the irreducible nucleon self-energy takes into account this relationship between the motion of a particle above the Fermi sea and that of a hole, which occurs below the Fermi sea. This self-energy can be thought of as the effective interaction of a particle or a hole with the medium. As in the simple shell-model, the self-energy has a static term, which is real; and like optical potentials, it has a dynamic (energy-dependent) term, which is complex. However, unlike optical potentials, the dynamic term exists at all energies, both positive and negative.

A key property of the self-energy is that the real part of the dynamic term is related to the imaginary part through a Kramers-Kronig dispersion integral. This dispersion relation expresses the link between nucleon propagation at positive and negative energies and is merely a consequence of the correct time ordering for adding and removing a nucleon. Thus it represents a constraint imposed by causality.

The reason that most optical potentials fitted to scattering data do not adequately describe bound state data is that they neglect this important relationship between the real and imaginary parts of the potential. In order to bring together the optical

model and the shell model, Mahaux and Sartor developed a model that incorporates this dispersion relation [21]. This model is now called the dispersive optical model (DOM) and is extensively reviewed in Ref. [22].

Aside from the additional constraint from the dispersion relation, Mahaux and Sartor used standard parametrizations for their DOM potential, separating the potential into surface, volume and spin-orbit terms, and obtained fits capable of simultaneously describing scattering and bound-state data [22]. Thus, the DOM combines the success of the shell-model in describing nuclear structure and the success of optical models in describing nuclear reactions. However, the DOM does better than the simple shell-model because it includes the effects of correlations beyond the mean-field. Indeed, the DOM yields a reduction of sp strength of valence states that is close to $(e, e'p)$ results [22–24].

Recent applications of the DOM have concentrated on the nucleon asymmetry dependence by simultaneously fitting data pertaining to different calcium isotopes [23, 25] and to spherical isotopes up to tin and ^{208}Pb [24]. An analysis of a chain of isotopes can be utilized to predict properties of isotopes with larger nucleon asymmetry by extrapolating DOM potentials. Such data-driven extrapolations present a reliable strategy to approach and predict properties of isotopes toward the respective drip lines, since they can be tested by performing appropriate experiments.

It is also important, however, to test the DOM against microscopic approaches for calculating optical potentials in order to gain insight and guidance to the functional forms of the DOM potentials. Of particular importance is the behavior of the DOM at negative energies since there is far less data available than at positive energies. It was shown in Ref. [26] that optical model potentials can be formally identified with the irreducible, nucleon self-energy. Some microscopic approaches, such as the Feshbach formalism [27, 28] and the G-matrix folding approximation [29], focus more on the scattering of two particles and do not adequately take into account the dynamical aspects of hole propagation. Therefore, they cannot be used to study the sp properties of the $(A-1)$ system, where A is the number of nucleons in the target nucleus.

The Green's function method, on the other hand, is ideally suited to pursue a microscopic understanding of the nucleon self-energy at both positive and negative energies [8]. Because of the inclusion of the dispersion relation in the DOM, the DOM potential is more directly related to the microscopic, nucleon self-energy than other optical potentials. In the past however, certain approximations and assumptions have been made which limit the comparison. For example, the DOM potentials, like most optical potentials, have been typically assumed to be local, whereas the self-energy is inherently nonlocal. The main goal of the work presented in this dissertation is to strengthen the correspondence of the DOM potentials with the nucleon self-energy with an emphasis on negative energies.

In Chapter 2, some relevant aspects of the Green's function formalism are introduced and the DOM is presented. Chapter 3 discusses the issue of nonlocality and its importance for a proper description of the nucleon self-energy. Chapter 4 presents results on using DOM potentials to analyze (d, p) reactions. Chapter 5 compares the DOM potential with a microscopic calculation that does a good job of describing LRC but that does not yet describe the full effects of SRC. Chapter 6 compares the DOM potential with a microscopic calculation that emphasizes the role of SRC but does not yet fully describe LRC. In Chapter 7, the results and conclusions are summarized.

Most of the results in Sec. 3.2 have been published in Ref. [30]. The results in Ch. 4 have been published in Ref. [31], most of the results in Ch. 5 have been published in Ref. [32], and most of the results in Ch. 6 can be found in Ref. [33].

Chapter 2

Formalism

2.1 Introduction

Optical potentials for nucleons scattering off a nucleus are meant to model the nucleon-nucleus effective interaction. From the perspective of the Green's function formalism, the propagation of a nucleon through a nuclear medium can be naturally framed in terms of the nucleon experiencing an effective interaction. This effective interaction is called the irreducible self-energy, and its properties can be studied in a systematic way. The goal of the DOM is to take advantage of these properties. The purpose of this chapter is to introduce some of the key concepts and quantities pertaining to the Green's function description of the many-body problem in nuclear physics and relate them to the DOM.

2.2 Propagator Formalism

2.2.1 Hamiltonian

The Hamiltonian for a bound nucleus is given by

$$\hat{H} = \hat{T} + \hat{V} = \sum_{\alpha\beta} \langle \alpha | \, T \, | \beta \rangle \, a^\dagger_\alpha a_\beta + \frac{1}{4} \sum_{\alpha\beta\gamma\delta} \langle \alpha\beta | \, V \, | \gamma\delta \rangle \, a^\dagger_\alpha a^\dagger_\beta a_\delta a_\gamma, \tag{2.1}$$

where $\hat{T}$ is the kinetic energy operator, V is the bare nucleon-nucleon interaction and $a^\dagger, a$ are the creation and annihilation operators, respectively. The Greek indices denote the quantum numbers for an arbitrary single-particle (sp) basis. Three-body forces have been suppressed for simplicity, but their inclusion doesn't change the DOM analysis. The Hamiltonian acting on the ground state of a nucleus with A nucleons yields

$$\hat{H}\left|\Psi_0^A\right\rangle = E_0^A\left|\Psi_0^A\right\rangle, \tag{2.2}$$

where $|\Psi_0^A\rangle$ is the exact many-body wave function for the ground state and E_0^A is the ground-state energy. The Hamiltonian also gives the energy for excited states, not only for the system with A nucleons but for any nucleus. In particular, for a nucleus with $A \pm 1$ nucleons, the Hamiltonian gives

$$\hat{H}\left|\Psi_n^{A\pm1}\right\rangle = E_n^{A\pm1}\left|\Psi_n^{A\pm1}\right\rangle, \tag{2.3}$$

where the state $|\Psi_n^{A\pm1}\rangle$ is the many-body wave function in the $A\pm1$ system, and $n > 0$ denotes an excited state of the $A \pm 1$ system. In principle, one can solve the many-body problem by solving the Schrödinger equation for the A-body wave function. This strategy is employed in the Green's Function Monte Carlo (GFMC) approach, which builds up the many-body wave function from realistic nucleon-nucleon and 3-nucleon interactions; but due to computational constraints this method is currently restricted to light nuclei up to $A = 12$ and is limited to low-lying bound states [34]. In self-consistent mean-field (SCMF) models, the many-body wave function is built up at the mean-field level but from effective nucleon-nucleon interactions, such as the Skyrme and Gogny interactions [35]. This approach has had success in describing nuclear structure [35] for heavier nuclei, but it is not capable of describing nuclear reactions. In addition, extensions of SCMF models beyond the mean-field picture are somewhat restricted since the effects of correlations are already included in the effective interactions and care is needed to avoid double counting.

The strategy of the Green's function method is to cast the many-body problem

into a perturbation expansion in terms of the nucleon-nucleon interaction V. Since this interaction is very strong, the expansion cannot be truncated but requires at least one infinite partial summation. The terms in the expansion can be represented pictorially as Feynman diagrams, which can be classified into 1st-order, 2nd-order, and higher-order diagrams. Approximations can then be made by choosing certain sets of diagrams to include in the infinite summation. Thus, the Green's function method provides a systematic way of studying correlations beyond the mean field.

2.2.2 The Propagator of a Many-Body System and its Relation to Experimental Quantities.

The central quantity in the Green's function formalism is the propagator, which can be constructed for single-particle (sp), two-particle (tp) and, in general, n-particle propagation.The work presented in this dissertation is focused primarily on the sp propagator, which in the context of nuclear physics describes the motion of a particle (hole) above (below) the Fermi sea of nucleons. Note that the notation "sp" refers to holes as well as particles. The particle propagator is given by

$$G^{+}(\alpha,\beta;t-t') = -\frac{i}{\hbar}\theta(t-t')\left\langle \Psi_0^A \right| a_{\alpha_H}(t) a^{\dagger}_{\beta_H}(t') \left| \Psi_0^A \right\rangle , \tag{2.4}$$

where $a_{\alpha_H}(t), a^{\dagger}_{\beta_H}(t')$ are the annihilation and creation operators, respectively, in the Heisenberg picture, *i.e.*

$$a_{\alpha_H}(t) = e^{i\hat{H}t/\hbar} a_\alpha e^{-i\hat{H}t/\hbar} \tag{2.5}$$

$$a^{\dagger}_{\beta_H}(t) = e^{i\hat{H}t/\hbar} a^{\dagger}_\beta e^{-i\hat{H}t/\hbar}. \tag{2.6}$$

The step function in Eq. (2.4) ensures that the addition of a particle occurs before a particle is removed. Physically, Eq. (2.4) represents the probability amplitude for a particle to travel in the presence of a nucleus initially in its ground state and exit leaving the nucleus in its ground state. Similarly, one can define the hole propagator,

which is given by

$$G^{-}(\alpha,\beta;t-t') = \frac{i}{\hbar}\theta(t'-t)\left\langle \Psi_0^A\right| a^{\dagger}_{\beta_H}(t')a_{\alpha_H}(t)\left|\Psi_0^A\right\rangle . \tag{2.7}$$

The creation and annihilation operators have been switched so that now a hole is added first and then removed. The step function has changed accordingly. The difference in sign of G^- and G^+ comes from switching the order of the operators, since they represent fermions, which obey the anti-commutation relation $\{a^{\dagger}_{\beta}, a_{\alpha}\} = \delta_{\alpha\beta}$. Physically, Eq. (2.7) represents the probability amplitude for a hole to propagate in a nucleus for a time $\Delta t = t' - t$ and leave the nucleus in its ground state.

The total propagator is simply the sum of the particle and hole propagators and can be written as

$$\begin{aligned} G(\alpha,\beta;t-t') &= G^{+}(\alpha,\beta;t-t') + G^{-}(\alpha,\beta;t-t') \\ &= -\frac{i}{\hbar}\left\langle \Psi_0^A\right| \mathcal{T}[a_{\alpha_H}(t)a^{\dagger}_{\beta_H}(t')]\left|\Psi_0^A\right\rangle , \end{aligned} \tag{2.8}$$

where $\mathcal{T}$ is the time-ordering operator and places the creation and annihilation operators in order of increasing time from right to left.

In practice, the energy formulation is usually employed. Inserting complete sets of states in the $A\pm1$ systems in Eqs. (2.4) and (2.7) and performing a Fourier transform of Eq. (2.8), one obtains the Lehmann representation of the nucleon propagator with respect to the A-body ground state

$$\begin{aligned} G(\alpha,\beta;E) &= \sum_m \frac{\left\langle \Psi_0^A\right| a_\alpha \left|\Psi_m^{A+1}\right\rangle \left\langle \Psi_m^{A+1}\right| a^{\dagger}_{\beta}\left|\Psi_0^A\right\rangle}{E-(E_m^{A+1}-E_0^A)+i\eta} \\ &+ \sum_n \frac{\left\langle \Psi_0^A\right| a^{\dagger}_{\beta} \left|\Psi_n^{A-1}\right\rangle \left\langle \Psi_n^{A-1}\right| a_{\alpha}\left|\Psi_0^A\right\rangle}{E-(E_0^A-E_n^{A-1})-i\eta}. \end{aligned} \tag{2.9}$$

Although a discrete sum has been used, there are continuum solutions in the $A\pm1$ systems as well, and these are implied in the completeness relations. The numerators of the particle and hole components of the propagator represent the products of

overlap functions associated with adding or removing a nucleon from the A-body ground state. The $+i\eta$ term in the denominator of the first term in Eq. (2.9) comes from the Fourier transform of the step function and is a consequence of the condition that $t > t'$, *i.e.* the particle travels forward in time. Similarly, the $-i\eta$ term is a consequence of the condition $t < t'$, which can be interpreted to mean that a particle travels backward in time.

For the case of a finite nucleus, it is convenient to define the hole Fermi energy ε_F^- and the particle Fermi energy ε_F^+:

$$\varepsilon_F^- = E_0^A - E_0^{A-1} \tag{2.10}$$

$$\varepsilon_F^+ = E_0^{A+1} - E_0^A. \tag{2.11}$$

The former corresponds to the energy required to remove a particle from the A system and leaving the $A-1$ system in its ground state, while the latter corresponds to the binding energy associated with adding a particle to the A system and leaving the $A+1$ system in its ground state. The average Fermi energy ε_F is defined by

$$\varepsilon_F \equiv \frac{1}{2}[\varepsilon_F^- + \varepsilon_F^+]. \tag{2.12}$$

A very useful quantity is the one-hole spectral function, which can be obtained from the imaginary part of the propagator in Eq. (2.9):

$$S_h(\alpha) = \frac{1}{\pi}\text{Im } G(\alpha; E) \tag{2.13}$$

$$= \sum_n |\langle \Psi_n^{A-1}| a_\alpha |\Psi_0^A\rangle|^2 \delta(E - \varepsilon_n^-), \tag{2.14}$$

where $\varepsilon_n^- = E_0^A - E_n^{A-1}$ is the energy of the hole and $|\langle \Psi_n^{A-1}| a_\alpha |\Psi_0^A\rangle|^2$ is the probability for removing a particle with quantum numbers α from the ground state and leaving the $A-1$ system in a state $|\Psi_n^{A-1}\rangle$. These quantities can be related to experimental data [2]. Thus, the spectral function is useful for understanding the distribution of

sp strength both theoretically and experimentally.

The absolute spectroscopic factor for a particular excited state is given by

$$S_n = \sum_\alpha |\left\langle \Psi_n^{A-1} \right| a_\alpha \left| \Psi_0^A \right\rangle|^2. \tag{2.15}$$

The occupation number for a sp state with quantum numbers α reads

$$n_\alpha = \left\langle \Psi_0^A \right| a_\alpha^\dagger a_\alpha \left| \Psi_0^A \right\rangle = \int_{-\infty}^{\varepsilon_F^-} \mathrm{d}E S_h(\alpha), \tag{2.16}$$

The integration is only up to ε_F^- since there are no contributions to $S_h(\alpha)$ above this energy. The total number of particles is

$$A = \sum_\alpha n_\alpha. \tag{2.17}$$

2.2.3 Perturbation Expansion

The expansion of the exact propagator is obtained by first finding an approximate propagator $G^{(0)}$ with a Hamiltonian $\hat{H}_0$. $G^{(0)}$ is called the unperturbed propagator and $\hat{H}_0$ is called the unperturbed Hamiltonian. The full Hamiltonian is

$$\hat{H} = \hat{H}_0 + \hat{V}', \tag{2.18}$$

where $\hat{V}'$ is the residual interaction. The unperturbed propagator is

$$G^{(0)}(\alpha, \beta; t - t') = -\frac{i}{\hbar} \left\langle \Phi_0^A \right| \mathcal{T}[a_{\alpha_I}(t) a_{\beta_I}^\dagger(t')] \left| \Phi_0^A \right\rangle, \tag{2.19}$$

where $|\Phi_0^A\rangle$ is the ground-state wave function associated with $\hat{H}_0$. The time dependence of the operators is now given in the interaction picture, instead of the Heisenberg picture. For an arbitrary operator $\hat{O}$, its time dependence in the interaction picture is

$$\hat{O}_I(t) = e^{i\hat{H}_0 t/\hbar} \hat{O} e^{-i\hat{H}_0 t/\hbar} \tag{2.20}$$

which is the same as the Heisenberg picture when $\hat{V}'$ is neglected. Beginning with the time-dependent Schrödinger equation, one can show that the exact propagator is

$$\begin{aligned} G(\alpha,\beta;t-t') &= -\frac{i}{\hbar}\sum_{m}^{\infty}\left(\frac{-i}{\hbar}\right)^{m}\frac{1}{m!}\int dt_1\int dt_m \\ &\times \langle\Phi_0^A|\,\mathcal{T}\left[\hat{V}'(t_1)..\hat{V}'(t_m)a_\alpha(t)a_\beta^\dagger(t')\right]|\Phi_0^A\rangle_{connected}\,, \end{aligned} \tag{2.21}$$

where all the operators are in the interaction picture, but the subscript I has been dropped. The subscript labeled *connected* indicates that only connected Feynman diagrams contribute to the full propagator.

The unperturbed Hamiltonian is typically chosen so that $|\Phi_0^A\rangle$ represents a system of non-interacting particles. Then, the action of the creation and annihilation operators on $|\Phi_0^A\rangle$ is known, since the sp states are either fully occupied or completely empty. The many-body state $|\Phi_0^A\rangle$ is then called the non-interacting ground state and $G^{(0)}$ the non-interacting propagator. The simplest case is $\hat{H}_0 = \hat{T}$. This choice is not useful for a finite nucleus, however, and usually an auxiliary potential $\hat{U}$ is used, so that $\hat{H}_0 = \hat{T} + \hat{U}$ and $\hat{V}' = \hat{V} - \hat{U}$.

Using a non-interacting ground state, the terms in Eq. (2.21) are readily obtained using Wick's theorem [36]. The term with $m = 0$ is just the non-interacting propagator. Examples of the 1st and 2nd order terms are shown in Fig. 2.1. The single lines with arrows represent the non-interacting propagator and the dashed lines represent the interaction $\hat{V}$. In the time formulation, time flows from bottom to top, whereas in the energy formulation the arrows simply show the flow of energy. The diagram in Fig. 2.1 a) leads to the Hartree-Fock (HF) approximation when summed to all orders. Figure 2.1 b) represents a particle coupling to a two-particle-one-hole (2p1h) intermediate state, and corresponds to a particle knocking a nucleon in the medium into a state above the Fermi sea, leaving behind a hole in the nuclear medium. Thus, a particle-hole pair is created and propagates along with the other particle.

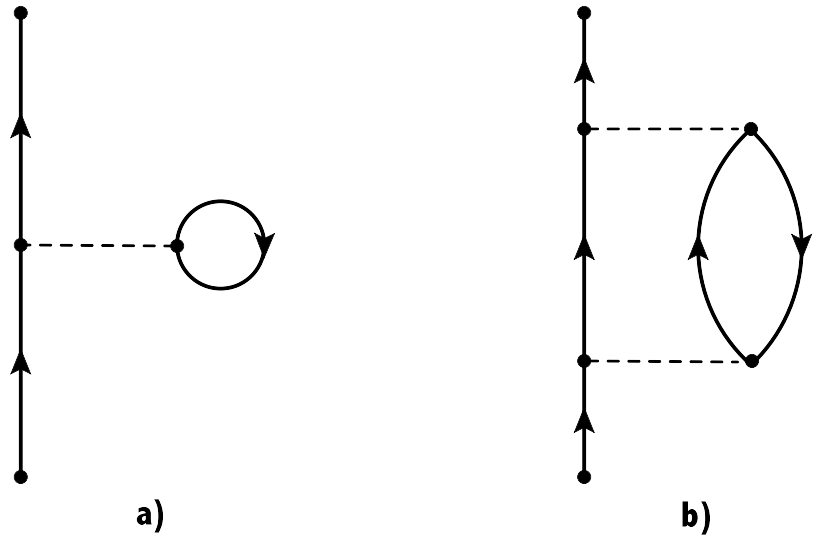

Figure 2.1: a) The first-order diagram in the perturbation expansion of the propagator and b) an example of a second-order diagram.

2.2.4 The Irreducible Self-energy and the Dyson Equation

The intermediate states shown in Fig. 2.1 are examples of self-energy diagrams, which illustrate the interaction of a particle or a hole with the medium. They are also examples of *irreducible* self-energy diagrams, which have the property that they cannot be broken into two other self-energy diagrams by removing a particle or a hole line. The sum of all irreducible self-energy diagrams to which a particle or a hole can couple is called the irreducible self-energy. A particle or a hole can couple to these states an infinite number of times, and summing up all these terms one obtains the reducible self-energy. The focus of the DOM is on the irreducible self-energy, so henceforth the irreducible self-energy will be referred to simply as the "self-energy". Some examples of irreducible self-energy diagrams are shown in Fig. 2.2. The first two diagrams were already encountered in Fig. 2.1. Figure 2.2 c) shows an intermediate two-hole-one-particle (2h1p) state. Figure 2.2 a) is energy-independent, but Figs. 2.2 b) and 2.2 c) are energy dependent and are responsible for redistributing sp strength. In par-

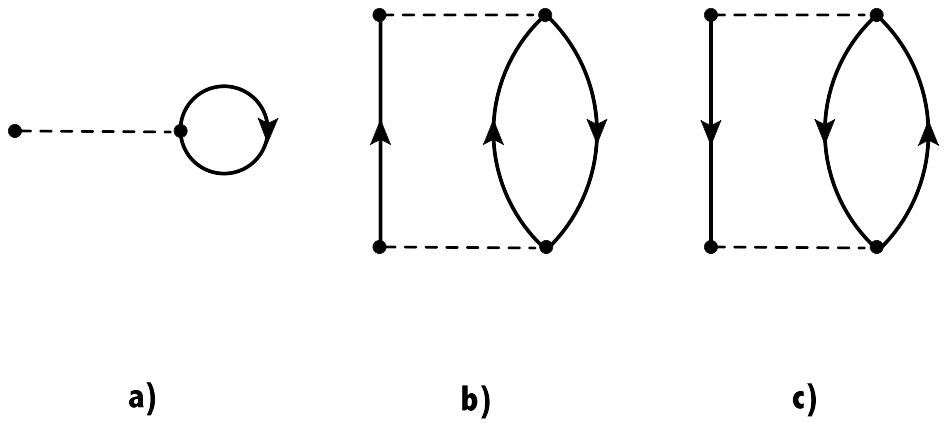

Figure 2.2: a) HF b) 2p1h c) 2h1p intermediate states.

ticular, the coupling to 2p1h states fragments the sp strength of the $A+1$ states and also removes strength from below the Fermi sea and places it above. The coupling to the 2h1p intermediate states leads to fragmentation of the sp strength of the $A-1$ states and creates a finite occupation of states that were originally empty in the non-interacting ground state.

The exact propagator can be expressed in terms of the self-energy as shown in Fig. 2.3. The exact propagator is shown as the double line, and the self-energy is denoted by the symbol Σ^*. Figure 2.3 conveys the idea of a quasiparticle. The propagation of a bare nucleon, represented by the single directed line, traveling through some nuclear medium affects the motion of other nucleons, which in turn affects the motion of the bare nucleon (hence the term "self-energy"). The effect of all these nucleons moving together is then represented by the double directed line. One can think of the bare nucleon being "dressed" by its interactions with the medium. For this reason, the propagator represented by the double lines is often referred to as the dressed propagator. This nomenclature is preferable to the "exact" propagator,

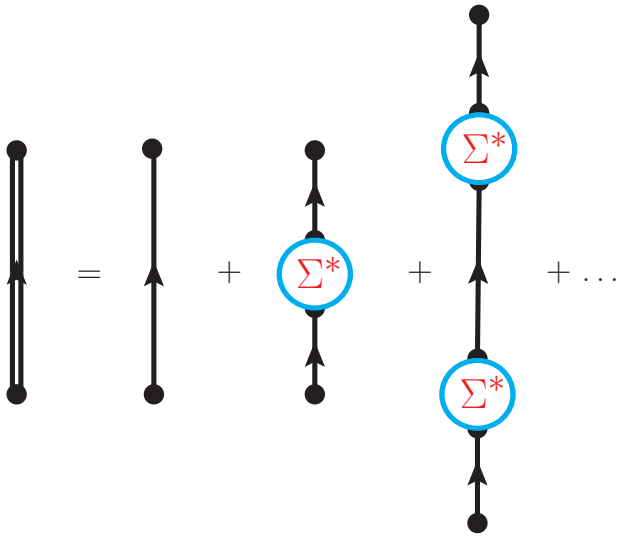

Figure 2.3: Expansion of the propagator in terms of the irreducible self-energy Σ^*. The double line represents the full propagator, and the single line represents the unperturbed propagator.

since the propagator is exact only if all possible self-energy diagrams are included. In practice, however, the self-energy is approximated by selecting only certain kinds of diagrams.

Mathematically, the expansion in Fig. 2.3 can be expressed as

$$G(\alpha,\beta;E) = G^{(0)}(\alpha,\beta;E) + \sum_{\gamma,\delta} G^{(0)}(\alpha,\gamma;E)\Sigma^*(\gamma,\delta;E)G(\delta,\beta;E). \tag{2.22}$$

This equation is known as the Dyson equation and introduces the idea of self-consistency. An approximation of the self-energy is obtained from a selection of diagrams. This self-energy is inserted in Eq. (2.22), whose solution yields the propagator G. The self-energy is then updated with this new propagator, and the Dyson equation can then be solved again for the propagator. This process can be repeated until the input propagator is the same as the propagator out within the desired accuracy. All contributions to the propagator are then generated by the Dyson equation itself. The solution of the Dyson equation generates all discrete poles corresponding to bound

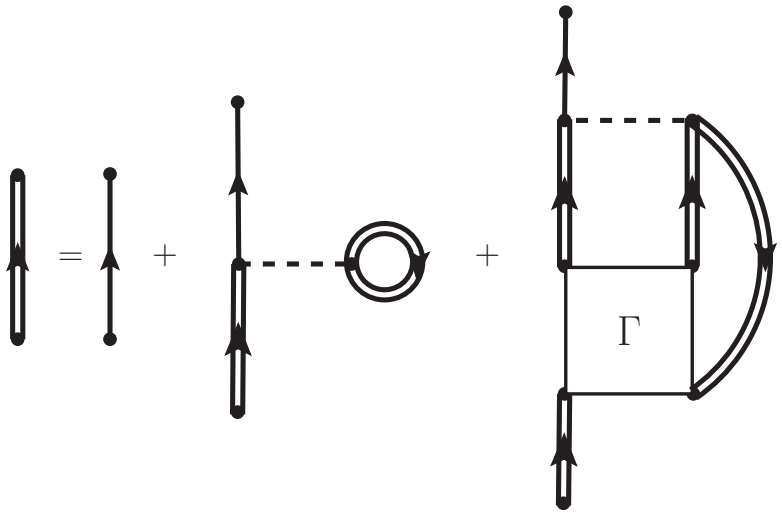

Figure 2.4: Propagator in terms of the self-consistent self-energy diagrams.

$A \pm 1$ states explicitly given by Eq. (2.9) that can be reached by adding or removing a particle with quantum numbers α.

The dressed propagator written in terms of the self-consistent self-energy diagrams is shown in Fig. 2.4. Note that dressed propagators are used for the intermediate states. The term Γ is the effective interaction between dressed particles in the medium. The self-consistent self-energy diagrams are obtained by removing the dressed propagator on the bottom and the unperturbed propagator on the top of the last two diagrams in Fig. 2.4. The aim of the DOM is to parametrize the self-consistent self-energy and constrain the parameters by a fit to data, thus obtaining an empirical self-energy.

In general, the self-energy is complex, nonlocal, and energy dependent. However, it can be divided into a static term Σ_s, which is real and energy independent, and a dynamic term Σ_d, which is complex and energy dependent. The static contribution arises from the correlated HF term, which is the intermediate state of the second diagram in Fig. 2.4, and the dynamic contribution arises from higher order correlations, which are contained in the contribution represented by the third diagram in Fig. 2.4.

The standard definition of the self-energy requires that its imaginary part is negative, at least on the diagonal, in the domain that represents the coupling to excitations in the $A+1$ system, while it is positive for the coupling to $A-1$ excitations [36]. This definition translates into an absorptive potential for elastic scattering at positive energy, where the imaginary part is responsible for the loss of flux in the elastic channel.

The real part of Σ_d is related to the imaginary part through a Kramers-Kronig type dispersion integral as follows:

$$\mathrm{Re}\Sigma_d(\alpha,\beta;E) = -\mathcal{P}\int_{\varepsilon_T^+}^{\infty}\frac{dE'}{\pi}\frac{\mathrm{Im}\Sigma_d(\alpha,\beta;E')}{E-E'} + \mathcal{P}\int_{-\infty}^{\varepsilon_T^-}\frac{dE'}{\pi}\frac{\mathrm{Im}\Sigma_d(\alpha,\beta;E')}{E-E'}, \tag{2.23}$$

where $\mathcal{P}$ represents the principal value and applies when E occurs in the interval of integration. The dynamic parts start and end at corresponding thresholds in the $A\pm1$ systems that have a larger separation than the corresponding difference between the Fermi energies for addition and removal of a particle, given by Eqs. (2.10) and (2.11). This feature is particular to a finite system and generates possibly several discrete quasiparticle and hole-like solutions of the Dyson equation in the domain where the imaginary part of the self-energy vanishes.

With Eq. (2.23), the total real part of the irreducible self-energy can be written as

$$\mathrm{Re}\Sigma^*(\alpha,\beta;E) = \Sigma_s(\alpha,\beta) + \mathrm{Re}\Sigma_d(\alpha,\beta;E). \tag{2.24}$$

In some cases it is useful to write the above equation in terms of some reference energy E_0. Evaluating $\mathrm{Re}\Sigma^*$ at E_0, then subtracting it from Eq. (2.24), we find that the static terms cancel and we are left with

$$\mathrm{Re}\Sigma^*(\alpha,\beta;E) - \mathrm{Re}\Sigma^*(\alpha,\beta;E_0) = \mathrm{Re}\Sigma_d(\alpha,\beta;E) - \mathrm{Re}\Sigma_d(\alpha,\beta;E_0),$$

which can be rewritten as

$$\mathrm{Re}\Sigma^*(\alpha,\beta;E) = \mathrm{Re}\Sigma^*(\alpha,\beta;E_0) + \mathrm{Re}\Sigma_d(\alpha,\beta;E) - \mathrm{Re}\Sigma_d(\alpha,\beta;E_0). \tag{2.25}$$

Inserting the relation for $\mathrm{Re}\Sigma_d$ in Eq. (2.23), we have

$$\begin{aligned}\mathrm{Re}\Sigma^*(\alpha,\beta;E) &= \mathrm{Re}\Sigma^*(\alpha,\beta;E_0) \\ &- \mathcal{P}\int_{\varepsilon_T^+}^{\infty}\frac{dE'}{\pi}\mathrm{Im}\Sigma_d(\alpha,\beta;E')\left[\frac{1}{E-E'}-\frac{1}{E_0-E'}\right] \\ &+ \mathcal{P}\int_{-\infty}^{\varepsilon_T^-}\frac{dE'}{\pi}\mathrm{Im}\Sigma_d(\alpha,\beta;E')\left[\frac{1}{E-E'}-\frac{1}{E_0-E'}\right].\end{aligned} \tag{2.26}$$

This form of the dispersion relation is known as the subtracted dispersion relation, and it is this form that is used in the DOM.

2.2.5 Propagator in Coordinate Space

DOM potentials are typically presented in coordinate space, primarily because the treatment of Coulomb is facilitated in this basis; so writing and developing a few of the above equations in coordinate space will help to make the connection between the propagator formalism and the DOM more apparent. In a basis with good radial position r, orbital angular momentum ℓ (parity), and total angular momentum j, the sum in Eq. (2.22) becomes an integral, and the Dyson equation takes on the following form

$$\begin{aligned}G_{\ell j}(r,r';E) &= G^{(0)}_{\ell j}(r,r';E) \\ &+ \int d\tilde{r}\ \tilde{r}^2 \int d\tilde{r}'\ \tilde{r}'^2 G^{(0)}_{\ell j}(r,\tilde{r};E)\Sigma^*_{\ell j}(\tilde{r},\tilde{r}';E)G_{\ell j}(\tilde{r}',r';E).\end{aligned} \tag{2.27}$$

In this expression the quantum numbers for isospin and for the projection of the total angular momentum have been suppressed. Beginning with the Dyson equation, one can show that for discrete states the overlap function obeys a Schrödinger-like

equation [36]. Introducing the notation

$$\psi^n_{\ell j}(r) = \langle \Psi^{A-1}_n | \, a_{r\ell j} \, | \Psi^A_0 \rangle \, , \tag{2.28}$$

for the overlap function for the removal of a nucleon at r with discrete quantum numbers ℓ and j, one finds

$$\left[\frac{p_r^2}{2m} + \frac{\hbar^2 \ell(\ell+1)}{2mr^2} \right] \psi^n_{\ell j}(r) + \int dr' \; r'^2 \Sigma^*_{\ell j}(r, r'; \varepsilon^-_n) \psi^n_{\ell j}(r') = \varepsilon^-_n \psi^n_{\ell j}(r), \tag{2.29}$$

where

$$\varepsilon^-_n = E^A_0 - E^{A-1}_n, \tag{2.30}$$

and in coordinate space the radial momentum operator is given by $p_r = -i\hbar(\frac{\partial}{\partial r} + \frac{1}{r})$. Equation (2.29) is for discrete states in the $A-1$ system, but a similar equation can be found for discrete states in the $A+1$ system. Discrete solutions to Eq. (2.29) exist in the domain where the self-energy has no imaginary part and these are normalized by utilizing the inhomogeneous term in the Dyson equation. For an eigenstate of the Schrödinger-like equation [Eq. (2.29)], the so-called quasihole state labeled by α_{qh}, the corresponding normalization or spectroscopic factor is given by [36]

$$S^n_{\ell j} = \left(1 - \left. \frac{\partial \Sigma_{\ell j}(\alpha_{qh}, \alpha_{qh}; E)}{\partial E} \right|_{\varepsilon^-_n} \right)^{-1}. \tag{2.31}$$

Discrete solutions in the domain where the self-energy has no imaginary part can therefore be obtained by expressing Eq. (2.29) on a grid in coordinate space and performing the corresponding matrix diagonalization.

For continuum energies, the solution of the Dyson equation in the form of Eq. (2.27), in the domain below the Fermi energy, can be formulated as a complex matrix inversion in coordinate space. Once the propagator is obtained, the hole spectral function is found from

$$S_{\ell j}(r; E) = \frac{1}{\pi} \mathrm{Im} \; G_{\ell j}(r, r; E). \tag{2.32}$$

The total spectral strength at E for a given ℓj combination,

$$S_{\ell j}(E) = \int_0^\infty dr\ r^2\ S_{\ell j}(r; E), \tag{2.33}$$

yields the spectroscopic strength per unit of energy, and is the equivalent of Eq. (2.31) for continuum energies.

Below the Fermi energy for the removal of a particle, ε_F^-, the corresponding discretization is limited by the size of the nucleus as can be inferred from the removal amplitude given in Eq. (2.28), which demonstrates that only coordinates inside the nucleus need to be considered. Such a finite interval therefore presents no numerical difficulty.

2.3 DOM Formalism

The Dyson equation in Eq. (2.22) is similar in form to the equation one would obtain for a particle propagating in an external potential. Thus, the self-energy can be thought of as an effective nucleon-nucleus interaction. The self-energy has many poles and the imaginary part can be represented as a series of δ functions at very low energies for strongly bound nuclei. However, for practical purposes optical potentials are parametrized as smooth functions of energy. Formally, smoothing the self-energy corresponds to evaluating $\Sigma^*(\alpha, \beta; E + i\Delta)$, where Δ is finite and real and possibly energy dependent [22]. The smoothed self-energy will be represented by

$$\mathcal{U} = \mathcal{V} + i\mathcal{W}, \tag{2.34}$$

where $\mathcal{V}$ is the real part and $\mathcal{W}$ is the imaginary part. The real part can be further subdivided into a static term, denoted by $\mathcal{V}_{HF}$, and a dynamic term, denoted by $\Delta\mathcal{V}$, which comes from the dispersion relation given in Eq. (2.26). This term is discussed in the next subsection.

2.3.1 Dispersion Relation

The propagator formalism described in the previous section provides a natural framework to describe both scattering and bound-state information. However, in most optical models the functional forms used to parametrize the potential do not adequately describe bound-state data when fit to elastic scattering data. Mahaux and Sartor realized that the optical potential for $E > 0$ should be related to the optical potential for $E < 0$ by means of the dispersion relation given in Eq. (2.23) [21, 22]. In practice, they employed the subtracted dispersion relation (2.26) with $E_0 = \varepsilon_F$, the average Fermi energy. In the $r\ell j$ basis, this subtracted dispersion relation becomes

$$\begin{aligned} \mathrm{Re}\Sigma^*_{\ell j}(r,r';E) &= \mathrm{Re}\Sigma^*_{\ell j}(r,r';\varepsilon_F) \\ &- \mathcal{P}\int_{\varepsilon_T^+}^{\infty}\frac{dE'}{\pi}\mathrm{Im}\Sigma^*_{\ell j}(r,r';E')\left[\frac{1}{E-E'}-\frac{1}{\varepsilon_F-E'}\right] \\ &+ \mathcal{P}\int_{-\infty}^{\varepsilon_T^-}\frac{dE'}{\pi}\mathrm{Im}\Sigma^*_{\ell j}(r,r';E')\left[\frac{1}{E-E'}-\frac{1}{\varepsilon_F-E'}\right]. \end{aligned} \tag{2.35}$$

The beauty of this representation was recognized by Mahaux and Sartor [21, 22] and lies in its ability to be readily linked with empirical information. The first term in Eq. (2.35) can be compared with a multitude of HF calculations which use effective nucleon-nucleon interactions. There are also experimental data, such as from proton and neutron scattering experiments, that put constraints on the imaginary part of the optical potential, which is then used to get the dynamic contribution to the real part by means of Eq. (2.35). This procedure requires further assumptions since detailed knowledge of the imaginary part of the self-energy below the Fermi energy has only become available with electron-induced proton knockout reactions [5].

Mahaux and Sartor call the first term in Eq. (2.26) the HF potential even though this term is not the true HF contribution to the self-energy. Nevertheless, in keeping with their notation, the following identification is made

$$\Sigma_{HF}(\alpha,\beta) = \Sigma^*(\alpha,\beta;\varepsilon_F), \tag{2.36}$$

When speaking of DOM potentials, this term will be referred to as the HF potential.

2.3.2 Local-equivalent Potential

Although the DOM potential is technically nonlocal, both the real and imaginary parts are typically approximated by local potentials. The HF potential from Eq. (2.36) then acquires an energy dependence that does *not* arise from a dispersion relation [22, 36–38]. In the DOM, the HF potential is separated into a spin-independent term and a spin-orbit potential. In a basis with vectors in coordinate space, the spin-independent term reads

$$\Sigma_{HF}(\boldsymbol{r}, \boldsymbol{r}'). \tag{2.37}$$

The corresponding form for the local-equivalent potential can then be written as

$$\Sigma_{HF}(\boldsymbol{r}, \boldsymbol{r}') \Rightarrow \mathcal{V}^{vol}_{HF}(r, E)\delta(\boldsymbol{r} - \boldsymbol{r}'), \tag{2.38}$$

where

$$\mathcal{V}^{vol}_{HF}(r, E) = V^{vol}_{HF}(E) f(r, r_{HF}, a_{HF}). \tag{2.39}$$

The superscript "*vol*" refers to "volume" and is present for reasons that will become clear in the next subsection. This potential is factorized into a part that contains all the energy dependence and a nuclear form factor that contains all the radial dependence. The unscripted V denotes the energy-dependent factor. The radial dependence is represented with a Woods-Saxon form factor

$$f(r, r_0, a_0) = \frac{1}{1 + \exp(\frac{r - r_0 A^{1/3}}{a_0})}. \tag{2.40}$$

where r_0 is radius parameter and a_0 is the diffuseness parameter. The factorized linear energy dependence can be parametrized by the corresponding effective mass

below the Fermi energy and can be represented by

$$V_{HF}(E) = V_{HF}(\varepsilon_F) + \left[1 - \frac{m^*_{HF}}{m}\right](E - \varepsilon_F)\,, \tag{2.41}$$

where m^*_{HF} is the effective mass below the Fermi energy and can be combined with the Woods-Saxon form factor to generate $m^*_{HF}(r)$. This version is inspired by the Skyrme implementation of the HF potential [22]. More generally, one may identify this effective mass with an energy-dependent version of the effective mass $\widetilde{m}^*(r;E)$ that governs the nonlocality of the self-energy and is sometimes referred to as the k-mass. It was shown in Ref. [39] that this effective mass is critical to reconcile the phenomenological (local) imaginary part of the optical potential with the microscopic one [36] and to explain the nucleon mean free path extracted from experiment. For finite nuclei, this implies that the DOM version of its local imaginary part $\mathcal{W}$ is related to the self-energy by

$$\mathcal{W}(r;E) = \frac{\widetilde{m}^*(r;E)}{m}\mathrm{Im}\Sigma(r;E). \tag{2.42}$$

2.3.3 Parametrization of the Self-energy

Typically, the DOM potential is parametrized with volume, surface, and spin-orbit terms, and in the case of protons the Coulomb potential is included as well. The energy-dependent terms are usually assumed to be factorized into a product of a function that depends only on the energy and one that depends on the radial coordinate, as is done in Eq. (2.39). For an implementation that uses local potentials, the HF component can be written as

$$\mathcal{V}_{HF}(r;E) = V^{vol}_{HF}(E)F^{vol}_{HF}(r) + V^{surf}_{HF}(E)F^{surf}_{HF}(r) + \boldsymbol{\ell}\cdot\boldsymbol{s}V^{so}_{HF}(E)F^{so}_{HF}(r), \tag{2.43}$$

where the functions $F_{HF}(r)$ are form factors describing the shape of the potential. As already mentioned, the volume part is usually parametrized with a Woods-Saxon

potential. The surface term F_{HF}^{surf} is chosen to be peaked at the surface of the nucleus, and a derivative of a Woods-Saxon is primarily used. Likewise, F_{HF}^{so} is also chosen to be surface peaked and modeled with the derivative of a Woods-Saxon. Generally speaking, the volume and spin-orbit terms are the dominant terms, and the surface term becomes important only at high positive energies [23, 24]. An energy dependence was assumed for V_{HF}^{so} in Ref. [23] but was found to be weak. No energy dependence was assumed in Ref. [24].

In a fashion similar to Eq. (2.43), the imaginary part can be written as

$$\mathcal{W}(r;E) = W^{vol}(E)F^{vol}(r) + W^{surf}(E)F^{surf}(r) + \boldsymbol{\ell}\cdot\boldsymbol{s}W^{so}(E)F^{so}(r). \qquad (2.44)$$

As for the HF terms, F^{vol} is usually represented with a Woods-Saxon while F^{surf} and F^{so} are represented with a derivative of a Woods-Saxon. For the imaginary potential, the dominant terms are the volume and surface terms. The typical energy dependence of the volume term $W^{vol}(E)$ and the surface term $W^{surf}(E)$ are shown in Fig. 2.5. At energies near the Fermi energy the surface term dominates and represents coupling to LRC. As energies become more negative (positive) the number of ways a hole (particle) can couple to 2h1p (2p1h) states increases, hence the rise in the absorption around the Fermi energy. At higher and more negative energies the volume term dominates and represents coupling to SRC. For increasing positive energies the volume term continues to increase. This effect is due to the increasing phase space for 2p1h states as energy increases. The coupling to these 2p1h states eventually goes to zero but only at much higher energies determined by the strength of the repulsive core of the nucleon-nucleon interaction. The point at which the coupling goes to zero is not known experimentally, but microscopic calculations give an energy $\simeq 1$ GeV or higher [36], depending on the underlying nucleon-nucleon interaction.

For large negative energies the volume term goes to zero more quickly. This effect is due to the fact that high-momentum components dominate the region of large negative energies, and the coupling of a hole to a high-momentum state becomes

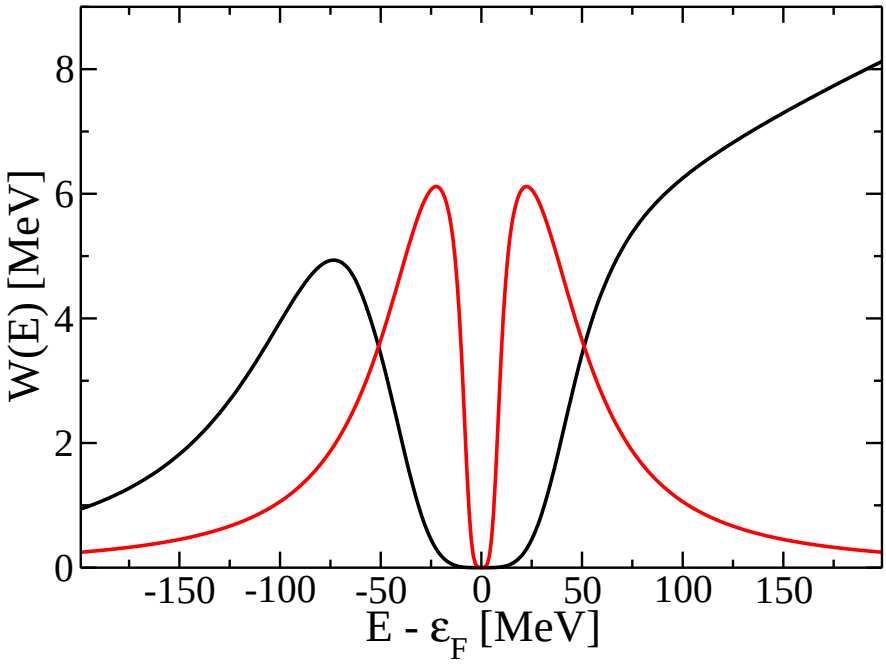

Figure 2.5: Examples of the energy dependence of the volume (black) and surface (red) terms of the imaginary part of the DOM potential.

increasingly difficult for increasing momentum. The imaginary spin-orbit term is generally quite small and only begins to have an effect at very high energies and very large negative energies.

2.3.4 Solution of the Dyson Equation

Current implementations of the DOM include scattering data up to 200 MeV, so a lowest-order relativistic correction is employed in solving the radial wave equation [40]

$$\left[\frac{d^2}{d\rho^2} + \left(1 - \frac{\widetilde{\mathcal{U}}(\rho, E)}{E_{tot} - M - m} - \frac{\ell(\ell+1)}{\rho^2}\right)\right]\varphi(\rho) = 0, \tag{2.45}$$

with $\rho = k\,r$, where $k = \frac{M}{E_{tot}}\sqrt{T(T+2m)}$, T is the laboratory kinetic energy, E_{tot} is the total energy in the center-of-mass frame, and M is the target mass. Due to the

lowest-order relativistic correction, a scaled potential has to be used, which is given by

$$\widetilde{\mathcal{U}} = \gamma \mathcal{U}, \gamma = \frac{2\left(E_{tot} - M\right)}{E_{tot} - M + m}. \tag{2.46}$$

The bound-state solutions to the radial wave equation are denoted by $\tilde{\varphi}_{n\ell j}\left(r\right)$, where n refers to the corresponding state in the $A\pm1$-system. The normalized wave functions corrected for nonlocality are then given by

$$\overline{\varphi}_{n\ell j}\left(r\right) = \sqrt{\frac{\widetilde{m}\left(r, \varepsilon_{n\ell j}\right)}{m}} \tilde{\varphi}_{n\ell j}\left(r\right), \tag{2.47}$$

where $\varepsilon_{n\ell j}$ is the discrete energy solution to Eq. (2.45). The relation between these corrected wave functions and the overlap functions is given by [30]

$$\sqrt{S_{n\ell j}} \overline{\varphi}_{n\ell j}(r) = r \psi^{n}_{\ell j}(r) \tag{2.48}$$

where

$$\int_0^\infty \overline{\varphi}^2_{n\ell j} dr = 1, \tag{2.49}$$

and $S_{n\ell j}$ is the spectroscopic factor. An approximate expression for the spectroscopic factor, proposed by Mahaux and Sartor [22], is

$$S_{n\ell j} = \int_0^\infty \overline{\varphi}^2_{n\ell j}\left(r\right) \frac{m}{\overline{m}(r, \varepsilon_{n\ell j})} dr, \tag{2.50}$$

and the energy-dependent effective mass is

$$\frac{\overline{m}\left(r, E\right)}{m} = 1 - \frac{m}{\widetilde{m}\left(r, E\right)} \frac{d\Delta\mathcal{V}(r, E)}{dE}, \tag{2.51}$$

which determines the reduction of strength from the mean-field value. The result for the spectroscopic factor in Eq. (2.50) was shown to be an excellent quantitative approximation to the corresponding solution of the Dyson equation in Ref. [30], which incorporates a nonlocal HF term (see Ch. 3).

The root-mean-square (rms) radius is given by

$$R_{n\ell j}^{rms} = \sqrt{\int_0^\infty \overline{\varphi}_{n\ell j}^2 (r)\, r^2 dr}. \tag{2.52}$$

With the background information given in this chapter, the results of the investigation on how to improve the DOM can now be discussed. The first topic to be addressed is the effect that a local approximation has on the interpretation of the DOM potential as the self-energy.

Chapter 3

Nonlocality in the DOM

In the Green's function formalism, all the energy dependence of the nucleon self-energy comes from the dynamic term, which includes the imaginary part and the real part arising from the dispersion relation in Eq. (2.23). This energy dependence is a consequence of the fact that the coupling of a nucleon in the medium to other states is energy dependent. If a nucleon has enough energy, for example, it can excite certain collective modes of the nucleus, such as surface vibrations.

In contrast, the energy dependence acquired by the static term when making a local approximation introduces an energy dependence in the potential that does not have a clear physical interpretation. In fact, as will be shown, this extra energy dependence has a number of unphysical consequences. In particular, this extra energy dependence yields solutions of the Dyson equation (*i.e.* overlap functions) that are not properly normalized. This distortion of the normalization then leads to difficulties in determining the sp strength distribution.

Using a non-local Hartree-Fock (HF) potential, however, removes the problems associated with the energy dependence of the local-equivalent HF potential of Eq. (2.38), and thus allows the DOM analysis to generate the nucleon propagator. Having a properly normalized Green's function is a big advantage because many quantities that are experimentally observable can be related to the propagator. Consequently, more data can be included in a DOM fit. Of particular interest is the inclusion of more data

pertaining to properties of nucleons below the Fermi energy because historically most of the data used in optical model fits are for $E > 0$. Constraining the empirical self-energy with more bound-state data, such as particle number, the charge density, and the binding energy per particle can provide valuable information about nuclear structure.

The purpose of this chapter is to show that including a truly nonlocal HF potential in the DOM formalism is an important step in establishing a greater correspondence between the empirical optical potential and the microscopic self-energy from the Green's function formalism, and that this greater correspondence opens up the possibility of including more data in a DOM fitting procedure to further constrain the empirical nucleon self-energy.

3.1 Procedure

As an initial step in understanding the effects of nonlocality, the local-equivalent potential $V_{HF}(r;E)$ was removed from a DOM potential obtained from a previous fit [23, 24] and replaced with a nonlocal, energy-independent potential $V_{HF}(\boldsymbol{r},\boldsymbol{r}')$. Only the volume contribution to the HF potential was replaced, since the other terms (*e.g.*, surface, spin-orbit) contained either no energy dependence or a relatively weak energy-dependence. Aside from the nonlocality correction factor given by Eq. (2.42), all parts of the fitted potential aside from the volume HF term were left unchanged. The nonlocal potential was then projected onto states with good orbital angular momentum and only the energy domain with $E < 0$ was studied.

Choosing an appropriate radial grid, Eqs. (2.27) and (2.29) were discretized. For continuum states, the propagator was obtained from a complex matrix inversion, as mentioned in Section 2, and for discrete states the propagator was obtained using Eq. (2.29). The location of the main fragments of the valence hole levels was then used to constrain the parameters of the non-local HF potential, which is described in the next section. The mean square radius of the charge distribution was also

used to constrain the parameters for nuclei where such experimental information was available. Only bound-state data were used to fit the nonlocal HF potential. Calculating cross sections with a nonlocal potential is computationally more involved and more expensive; however, nonlocality appears to be an important aspect of the nucleon self-energy, not only for the HF term (as will be discussed in this chapter), but also for the imaginary part. As shown in subsequent chapters, microscopically calculated self-energies exhibit substantial nonlocal imaginary parts.

3.1.1 Nonlocal Hartree-Fock Term

One form for the central nonlocal potential, proposed by Perey and Buck [37], is given by

$$V_{NL}(\boldsymbol{r},\boldsymbol{r}') = U\left(\frac{|\boldsymbol{r}+\boldsymbol{r}'|}{2}\right) H\left(\boldsymbol{r}-\boldsymbol{r}'\right). \tag{3.1}$$

The factor U is parametrized with a Woods-Saxon potential. Defining

$$r_f = \frac{1}{2}|\boldsymbol{r}+\boldsymbol{r}'| = \frac{1}{2}\sqrt{r^2+r'^2+2rr'\cos\gamma}, \tag{3.2}$$

where γ is the angle between the vectors $\boldsymbol{r}$ and $\boldsymbol{r}'$, U can be written as

$$U(r_f) = V_0 f(r_f), \tag{3.3}$$

where V_0 is the potential depth and f represents a Woods-Saxon shape with the dependence on the radius and diffuseness parameters implied. The factor H is a Gaussian function:

$$H\left(\boldsymbol{r}-\boldsymbol{r}'\right) = \frac{1}{\pi^{3/2}\beta^3}\exp\left(\frac{-|\boldsymbol{r}-\boldsymbol{r}'|^2}{\beta^2}\right). \tag{3.4}$$

The parameter β controls the degree of nonlocality of V_{NL}, and empirically has been determined to be on the order of 1 fm [22]. If Eq. (3.3) is used in Eq. (3.1), then projecting V_{NL} onto states with good total angular momentum requires a numerical

integration over $\cos\gamma$. The projection of H itself, however, has an analytical solution due to the relationship between the spherical Bessel functions j_ℓ and the Legendre polynomials P_ℓ:

$$j_\ell(z) = \frac{1}{2i^\ell}\int_{-1}^{+1} \mathrm{d}t e^{izt} P_\ell(t). \tag{3.5}$$

Thus, using a form in which U does not depend on γ is more tractable. In this case, we have

$$V_{NL}^\ell = U(r,r')\frac{1}{\pi^{1/2}\beta}\exp\left[-\frac{r^2+r'^2}{\beta^2}\right] K_\ell(x) \tag{3.6}$$

where

$$K_\ell(x) = 2i^\ell x j_\ell(-ix) = 2i^\ell x(-1)^\ell j_\ell(ix) \tag{3.7}$$

$$x = 2rr'/\beta^2. \tag{3.8}$$

One alternative, also proposed by Perey and Buck, is to approximate Eq. (3.2) with $r_f \approx (r+r')/2$. Another form, which gives results very close to that of Eq. (3.1) is to set

$$U(r,r') = V_0\sqrt{f(r)f(r')}. \tag{3.9}$$

3.1.2 Fitting

The nonlocal forms just discussed require 4 parameters: the three parameters defining the Woods-Saxon—V_0, r_0, a_0—and the non-locality parameter β. In the case of nuclei with $N \neq Z$, two parameters for the potential depth were used, V_n for the neutrons and V_p for the protons. These 4-5 parameters were the only ones that were adjusted.

As already mentioned, the data used to constrain these parameters were the bound levels, in particular the valence levels, and, if available, the mean square radius of the charge distribution. Once the propagator is known, the charge distribution can easily be obtained by calculating the one-body density matrix. The one-body density matrix element is found by integrating the imaginary part of the propagator up to the Fermi energy for each ℓj combination:

$$\begin{aligned} n_{\ell j}(r',r) &= \frac{1}{\pi}\int_{-\infty}^{\varepsilon_F} dE\ \mathrm{Im}G_{\ell j}(r,r';E) \\ &= \langle\Psi_0^A|\, a^\dagger_{r'\ell j} a_{r\ell j}\,|\Psi_0^A\rangle\,. \end{aligned} \tag{3.10}$$

For protons, the point charge distribution is thus obtained from the diagonal matrix elements of the one-body density matrix

$$\rho_p(r) = \frac{e}{4\pi}\sum_{\ell j}(2j+1)n_{\ell j}(r,r). \tag{3.11}$$

For some of the nuclei studied, such as ^{40}Ca, there are data for the charge density. For comparison with the experimental charge density it is necessary to fold Eq. (3.11) with the proton charge density. The procedure outlined in Ref. [41], which employs 3 gaussians for the proton, was used. The mean square radius of the resulting charge distribution is obtained from

$$\langle r^2\rangle = \frac{1}{Ze}\int_0^\infty dr\ r^2\rho_{ch}(r). \tag{3.12}$$

3.2 Results for ^{40}Ca

Using the procedure outlined in the previous section, the energy dependent HF term from the DOM potential in Ref.[23] was removed for ^{40}Ca and replaced with an energy-independent term of the form given by Eq. (3.1). The original, local DOM potential had previously been obtained from a global fit to both scattering and bound-state data of Calcium isotopes.

It should be noted here that no additional parameters were introduced. The local term that was replaced was defined by radius and diffuseness parameters and two parameters determining the energy-dependent potential depth—four parameters in all. So, in the nonlocal analysis, the same number of parameters were used. However, only the four parameters of the nonlocal HF potential were used for fitting. These

Table 3.1: Parameters for the local energy-dependent Woods-Saxon potential and the nonlocal version with gaussian nonlocality for ^{40}Ca. Published in Ref. [30].

	local	nonlocal
Depth [MeV]	-56.5	-92.3
Radius [fm]	1.19	1.05
Diffuseness [fm]	0.70	0.70
$\widetilde{m}^*_{HF}/m$	0.57	-
Nonlocality [fm]	-	0.91

parameters are shown in Table 3.1 and compared with the four parameters used in Ref. [23] to define the local HF potential at energies below the Fermi energy.

3.2.1 Spectral Strength

The normalization distortion resulting from the energy dependence of the local-equivalent HF potential is illustrated in Fig. 3.1, where the proton $s_{1/2}$ spectral strength calculated with a non-local potential is compared with that calculated with the local version from the original fit. The integration of the spectral strength up to the Fermi energy gives the number of particles with a specific ℓj. Integrating the solid, blue curve (non-local version) yields 3.4 $s_{1/2}$ particles; integrating the dashed, red curve (local version) yields about 6.7 $s_{1/2}$ particles, which is a substantial overestimate. Indeed, summing up the sp strength for the other partial waves in the local version leads to a total number of protons of more than 30.

Another problem associated with using a local-equivalent potential is that fitting deeply bound states, such as the $0s_{1/2}$ level in ^{40}Ca, is not easily done if the levels near the Fermi energy are to be adequately placed. This difficulty is due to the linear energy dependence that is often assumed for the local-equivalent potential below the Fermi energy. As the energy decreases (becomes more negative), the potential well becomes deeper. Using a nonlocal potential avoids this issue entirely and poses no difficulty in placing the $0s_{1/2}$ level in accordance with experimental observations from

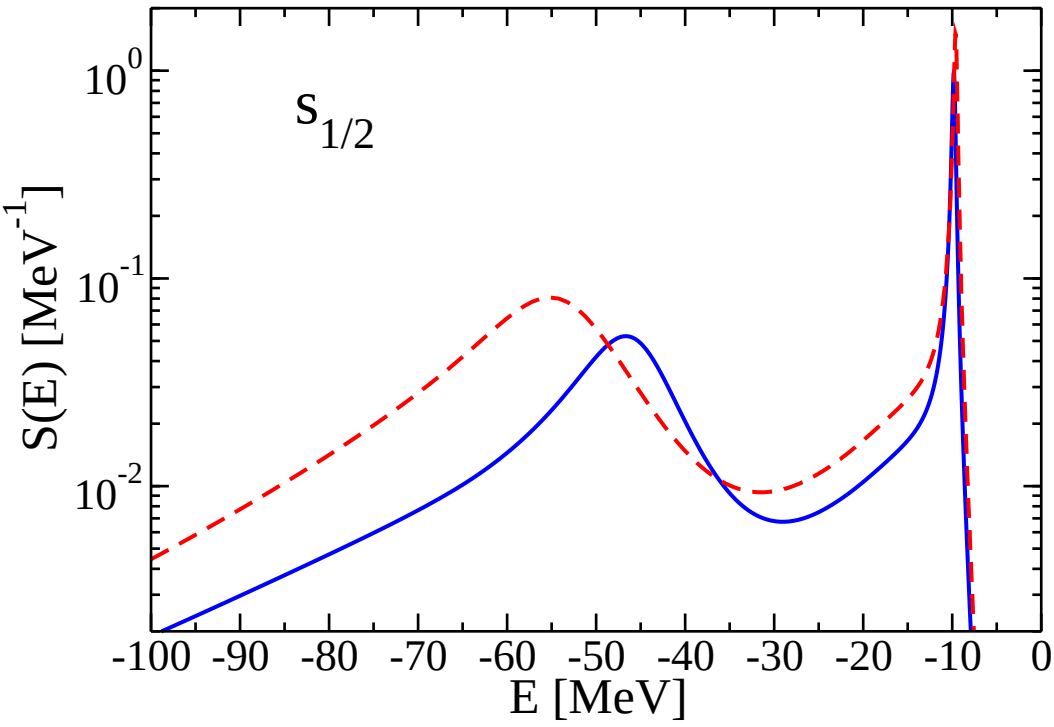

Figure 3.1: Comparison of proton $s_{1/2}$ spectral strength with the nonlocal (solid) and local potential with the spurious energy dependence (dashed). Note that the dashed curve even exceeds the number of mean-field $s_{1/2}$ particles by more than 50% illustrating the incorrect normalization when the local energy-dependent potential is used in the Dyson equation without proper corrections.

$(p, 2p)$ [42, 43] and $(e, e'p)$ experiments [44]. This improvement can also be seen in Fig. 3.1. The sharp peaks in Fig. 3.1 show the locations of the $1s_{1/2}$ energy levels in the two versions, and the broad peaks show the locations of the $0s_{1/2}$ energy levels. In the local version, the $0s_{1/2}$ level is too deeply bound (see also Table 3.2).

The correct strength distributions for the other ℓj channels relevant for calculations at negative energies, including $f_{7/2}$, are shown in Fig. 3.2. The peaks in panels (a)-(e) correspond to the orbits that are expected to be fully occupied in the mean-

field picture. The width of the each peak is related to the strength of the imaginary potential in the energy region around the peak, which represents the local mixing with more complicated states like 2h1p, *etc.* Since the imaginary potential is very small at energies near the Fermi energy, the $1s_{1/2}$ level, for example, is sharply peaked. Further below ε_F, the imaginary potential is stronger, so the $0s_{1/2}$ level has a larger width.

The $f_{7/2}$ orbit is empty in a mean-field picture, but the presence of the imaginary part of the self-energy below the Fermi energy allows some finite amount of $f_{7/2}$ strength to appear below the Fermi energy, as can be seen in panel (f). When integrating the total strength shown in Fig. 3.2 for all orbits except the $f_{7/2}$ and multiplying with the corresponding degeneracy factor of $2j + 1$, the summed strength is 19.48. While this may appear reasonable, it should be kept in mind that the assumed state independence of the DOM potential (apart from spin-orbit) and the ℓ-dependence of the nonlocal HF potential imply that some strength will also be generated for higher ℓ-values leading to an overestimate of the total proton number. Indeed, when the cut-off is placed at $\ell = 3$, *i.e.* the $f_{7/2}$ and $f_{5/2}$ contributions are also included, the total proton number becomes 21.43. This suggests that in future DOM work the total proton (neutron) number should be used as a further constraint on the potentials. The possibility of including some state dependence may also be explored, in particular by relying on microscopic input from FRPA calculations [8, 9, 45, 46].

3.2.2 Comparison of Quasiparticle Properties

Before discussing new results not available with the standard DOM implementation, several quasiparticle properties in the two approaches are first compared. Table 3.2 compares quasihole energies obtained with the local and nonlocal DOM with experimental data (for deeply-bound orbits Ref. [43] was used). The numbers quoted in the tables for quasiparticle properties using the local version of the DOM differ slightly from the ones generated in Ref. [23], since a small error in the calculation of the dis-

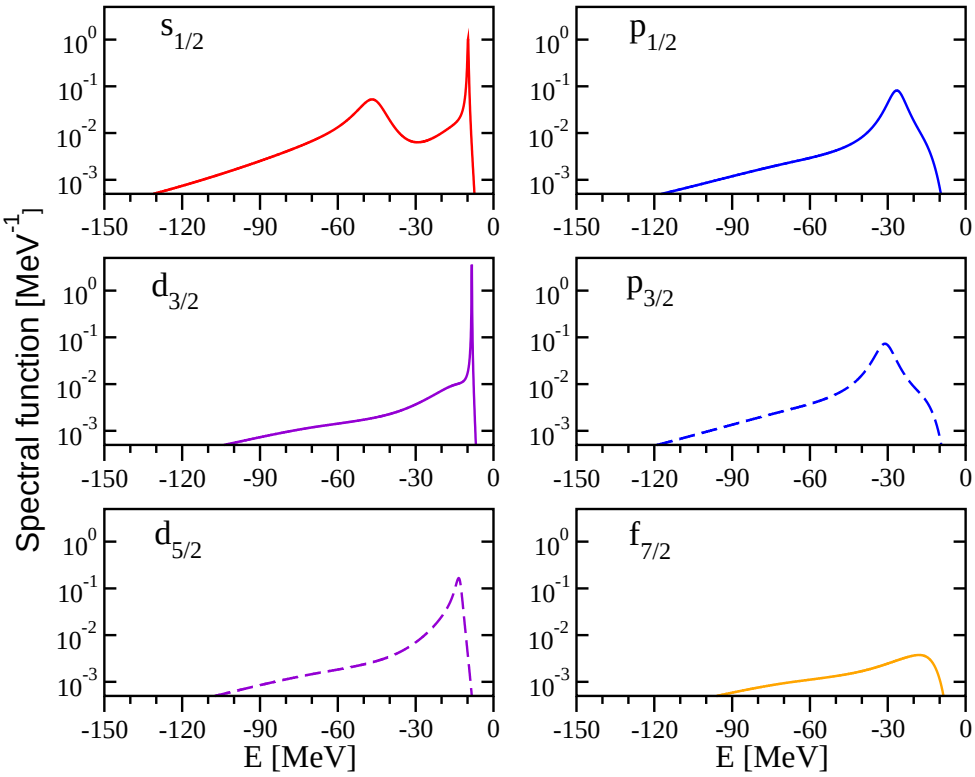

Figure 3.2: Spectral functions for all mostly occupied ℓj combinations in ^{40}Ca together with the $f_{7/2}$ result. These results exhibit similar peak locations and widths as observed in $(p, 2p)$ [42, 43] and $(e, e'p)$ experiments [44]. Published in Ref. [30].

Table 3.2: Quasihole energies for proton orbits in ^{40}Ca for the local and nonlocal DOM implementation compared with experiment. Published in Ref. [30].

	Energy [MeV]			
orbit	local	nonlocal	peak	experiment
$0s_{1/2}$	-57.3	-47.4	-46.7	∼-47
$0p_{3/2}$	-35.1	-31.4	-31.1	∼-30
$0p_{1/2}$	-30.3	-26.7	-26.4	∼-30
$0d_{5/2}$	-13.5	-13.8	-13.5	-13.5
$1s_{1/2}$	-9.5	-9.8	-9.8	-10.8
$0d_{3/2}$	-8.3	-8.3	-8.3	-8.3

persive volume contribution was corrected. The column labeled "local" reports the solutions of the eigenvalue equation for the local DOM potential without the imaginary part. This includes a self-consistency procedure since the potential is energy dependent, *i.e.* the chosen input energy has to coincide with the obtained eigenvalue. Such a calculation for the nonlocal DOM is reported in the column labeled nonlocal. The imaginary part is included in the column labeled "peak" which identifies the location of the peak of the spectral function for each orbit. As expected, there is little difference between the latter two approaches, especially close to the Fermi energy.

The largest difference between the local and nonlocal approach occurs for the lowest $s_{1/2}$ orbit. As discussed earlier, the nonlocal potential is better able to constrain the peak of the spectral $s_{1/2}$ strength to the correct value. Overall agreement for the peak location appears quite satisfactory for the nonlocal DOM although it may be necessary to consider some state dependence if a better fit for $1s_{1/2}$ quasihole energy is deemed appropriate. The results for neutrons are naturally not very different apart from the Coulomb shift to those for protons on account of isospin symmetry and are therefore not reported. However, one important thing to note is that the lowest neutron $s_{1/2}$ peak occurs at -56 MeV in the nonlocal DOM while in the local counterpart it is found at -67 MeV, confirming the discussion for the corresponding proton level that the local DOM tends to bind this orbit too deeply.

Table 3.3: Spectroscopic factors for proton orbits in ^{40}Ca for the local and nonlocal DOM implementation. Published in Ref. [30].

orbit	local	nonlocal
$0s_{1/2}$	1.11	0.98
$0p_{3/2}$	0.94	0.93
$0p_{1/2}$	0.95	0.94
$0d_{5/2}$	0.83	0.86
$1s_{1/2}$	0.67	0.65
$0d_{3/2}$	0.65	0.64

In Table 3.3 the spectroscopic factors are listed for the same orbits as in Table 3.2. These results were obtained for the local DOM by using the approximate expression for the spectroscopic factor given in Eq. (2.50). This expression does not guarantee that the resulting spectroscopic factor is less than 1 (as it should be), which is illustrated by the outcome for the $0s_{1/2}$ orbit. For the nonlocal DOM, Eq. (2.31) was used, where the derivative is taken at the eigenvalue obtained from Eq. (2.29) with neglect of the imaginary part of the potential. This procedure is also not appropriate in the domain where the imaginary part becomes substantial and is already suspect for the $d_{5/2}$ orbit. When the imaginary part is neglected, it is possible that the total real dispersive correction has a positive derivative at the energy corresponding to the self-consistent eigenvalue even in the nonlocal case, leading to an unphysical spectroscopic factor. The strength content of the peak for the $d_{5/2}$ orbit in Fig. 3.2 is more in line with the spectroscopic factors quoted for the $1s_{1/2}$ and $0d_{3/2}$ orbits and therefore substantially smaller than the 0.86 listed in Table 3.3. Only for the latter two orbits is the neglect of the imaginary part of the potential unimportant, since the content of the sharp peaks in Fig. 3.2 coincides with the spectroscopic factors given in Table 3.3. In addition, there is reasonable agreement with the local and nonlocal DOM results for these levels. It is only for these orbits then that the use of spectroscopic factors is sensible and unambiguous.

The spectroscopic factors for the more deeply bound quasihole states can be es-

timated for a corresponding $n\ell j$ by first extracting the spectral strength due to the state with quantum number n, $S_{n\ell j}(E)$, and then fitting the peak of the $S_{n\ell j}(E)$ contribution with an appropriate functional form. This contribution can be obtained by transforming the propagator from r-space to n-space:

$$S_{n\ell j}(E) = \frac{1}{\pi} \int \mathrm{d}r r^2 \int \mathrm{d}r' r'^2 \psi^n_{\ell j}(r) G_{\ell j}(r, r') \psi^n_{\ell j}(r'), \tag{3.13}$$

where $\psi^n_{\ell j}$ are overlap functions associated with the removal of a nucleon, but are normalized to unity. The spectral strength distribution for the $0s_{1/2}$ state is shown in Fig. 3.3 with the peak fitted with a Gaussian of the form

$$f(E) = S \frac{1}{\sigma\sqrt{2\pi}} e^{-(E-E_0)^2/2\sigma^2}.$$

The above Gaussian form is centered at the location of the quasihole peak E_0 and normalized to S. The normalization and the width were adjusted to approximate the height and width of the quasihole peak, resulting in a spectroscopic factor of $S = 0.66$ and a width $\Gamma = 13$ MeV (FWHM), where $\Gamma = 2\sqrt{2\ln 2}\sigma$. In the local DOM, Mahaux and Sartor calculate the width with the approximate expression

$$\Gamma_{n\ell j} = -2 \frac{\int \mathrm{d}r \bar{\varphi}^2_{n\ell j}(r) \mathcal{W}(r; E_{n\ell j})}{\int \mathrm{d}r \bar{\varphi}^2_{n\ell j}(r) \frac{m^*(r; E_{n\ell j})}{m}} \tag{3.14}$$

which yields a slightly larger width of 17 MeV for the $0s_{1/2}$ hole state. This larger width is also evident in Fig. 3.1. Based on the spectral strength distribution of this hole state deduced from $(p, 2p)$ and $(e, e'p)$ experiments [43, 47], the experimental width can be inferred to be $\Gamma_{\mathrm{exp}} \simeq 20$ MeV. Since the width is related to the strength of the imaginary potential, experimental widths for the deeply-bound states could be used to constrain the imaginary potential at negative energies far from the Fermi energy.

However, from a microscopic calculation of the self-energy (see Ch. 5), the strength of the absorption decreases with orbital angular momentum, and this ℓ-dependence is

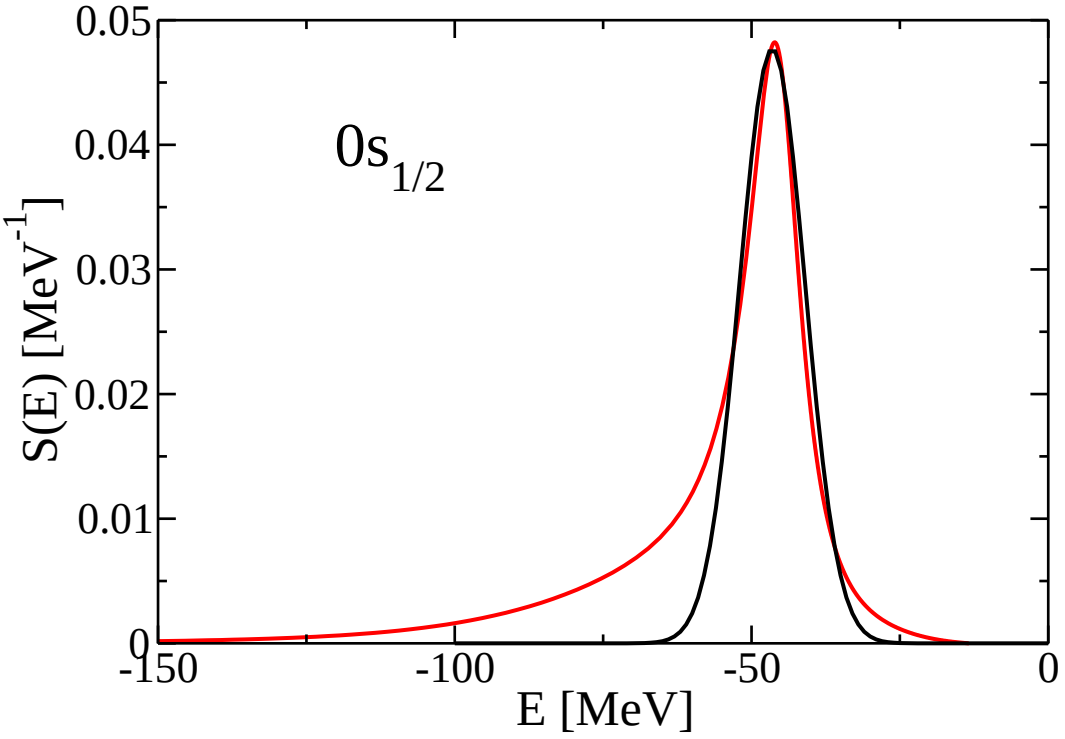

Figure 3.3: $S_{n\ell j}(E)$ for the proton $0s_{1/2}$ in ^{40}Ca (red) with the peak fitted by a Gaussian (black).

due in part to the nonlocality of the imaginary part of the self-energy. The microscopic self-energy suggests that the DOM absorption is too small for the $\ell = 0$ channel but too large for channels with $\ell > 1$. This lack of ℓ-dependence in the imaginary part of the DOM may then explain why the DOM result is smaller than indicated by experiment. Therefore, if the widths are to be fit, a nonlocal imaginary potential should probably be used.

3.2.3 Charge Distribution

The charge density of ^{40}Ca and its corresponding mean square radius are well known experimentally. The parameters in Table 3.1 generate a value of 3.45 fm compared

to the experimental result of 3.45 fm taken from the Fourier-Bessel analysis given in Ref. [48]. It was found that the experimental mean square radius was a significant constraint on the parameters of the nonlocal HF potential, strongly suggesting that this quantity should be included in future DOM fits.

The charge density calculated from Eq. (3.11) and folded with the proton charge density is compared with the experimental one in Fig. 3.4. The uncertainty of the experimental values are 1% or less [49], and the error bars in Fig. 3.4 reflect this uncertainty. They are not necessarily associated with actual data points. Obviously, there is still a significant discrepancy with the experimental charge density near the origin that requires further analysis. This discrepancy may be due in part to an incorrect treatment of SRC in the DOM. This topic will be discussed in the next section.

3.2.4 High-momentum Content in the DOM

The nucleon-nucleon interaction becomes repulsive at a small enough relative distance. In a nucleus, this repulsion results in some nucleons having high momentum. As discussed at length in Refs. [7, 50, 51], the presence of high-momentum components becomes more pronounced with decreasing energy (away from the Fermi energy), and this behavior has been experimentally confirmed in Ref. [52]. This behavior can be easily understood on the basis of simple considerations involving momentum conservation and the location of the relevant 2h1p states that are required for the admixture of high-momenta [8].

In order to see, then, whether the DOM also follows this behavior, the momentum distribution and momentum-space spectral function were studied. Since the DOM potential is given in coordinate space, the momentum-space spectral function was generated by performing a double Fourier-Bessel transform of the spectral function

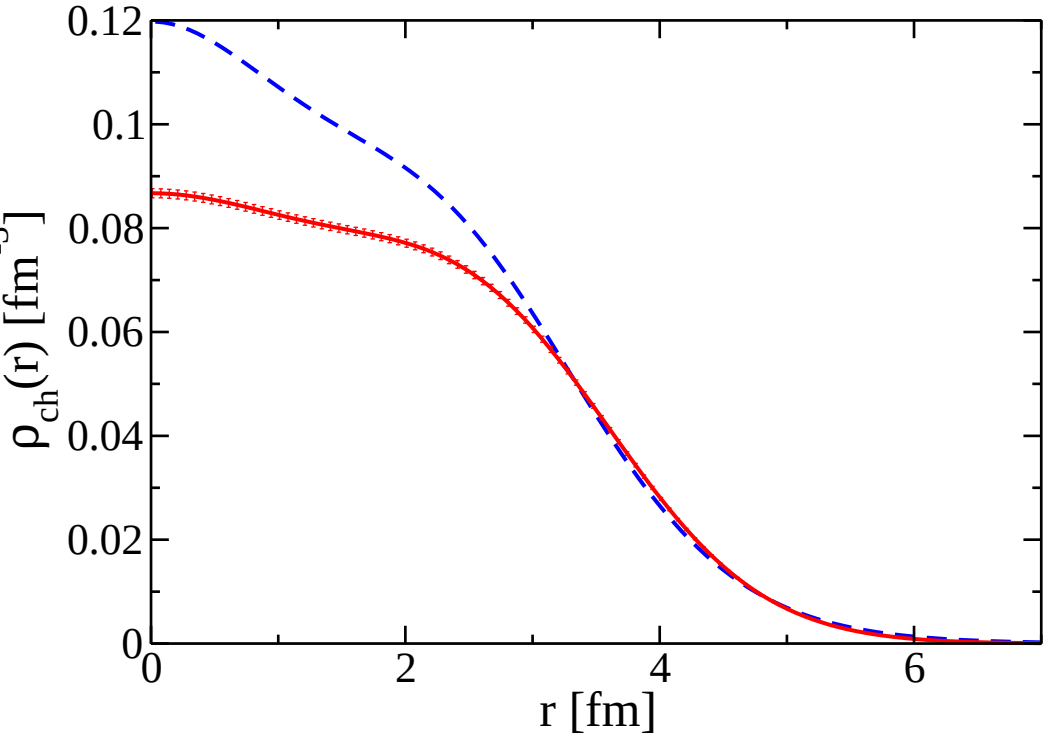

Figure 3.4: Experimental charge density of ^{40}Ca [48] (solid) compared with the DOM result (dashed).

in coordinate space:

$$S_{\ell j}(k;E) = \frac{2}{\pi}\int_0^\infty dr r^2 \int_0^\infty dr' r'^2 j_\ell(kr)\mathrm{Im}G_{\ell j}(r,r';E)j_\ell(kr'). \tag{3.15}$$

The momentum distribution for a given ℓj is then obtained from

$$n_{\ell j}(k) = \int_{-\infty}^{\varepsilon_F} dE\ S_{\ell j}(k;E). \tag{3.16}$$

The total proton momentum distribution (normalized by the calculated Z) is then

$$n(k) = \frac{1}{Z}\sum_{\ell j}(2j+1)n_{\ell j}(k). \tag{3.17}$$

This quantity is displayed in Fig. 3.5 by the dashed line. For comparison the momentum distribution from the quasihole wave functions (normalized to one) is displayed by the solid line. As discussed in Refs. [7, 50, 51], these quasihole contributions are mostly associated with wave functions near the Fermi energy and hardly contain any high-momentum components. Thus, the dashed line in Fig. 3.5 demonstrates the presence of high-momentum components in the DOM potential. Furthermore, about 10% of the protons were found to have momenta beyond 1.4 fm^{-1}. This number is in reasonable agreement with the 10% generated for ^{16}O in the calculations of Refs. [7, 50, 51] and in quite good agreement with the experimental results of Ref. [52]. These results show that the present version of the DOM is capable of representing experimentally well-established effects related to the presence of SRC, at least in the aggregate.

Looking at the spectral functions, however, reveals that the expected energy dependence of high-momentum components—that is, that the high-momentum components become increasingly important with increasing separation energy—is not contained in the DOM. The $d_{3/2}$ spectral in momentum space at different energies is plotted in Fig. 3.6. This figure illustrates that the *shape* of the momentum content of the spectral function hardly changes as a function of energy, especially when mo-

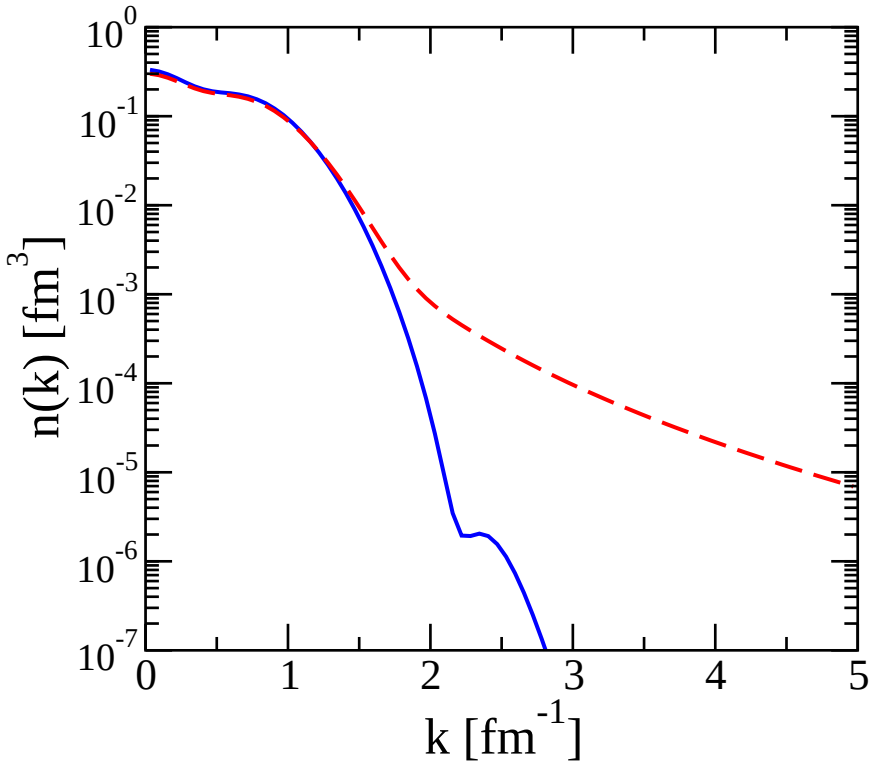

Figure 3.5: Comparison of the total momentum distribution calculated according to Eq. (3.17) (dashed) with the one obtained from the quasihole contributions (solid). Published in Ref. [30].

menta above 1.4 fm^{-1} are considered. This feature is completely opposite to the effect expected of SRC. The high-momentum content in the $s_{1/2}$ orbit, shown in Fig. 3.7, does not show any essential change in energy either.

In order to describe the correct behavior of the high-momentum components in the DOM it may be necessary in the future to make the geometry of the potential dependent on energy. Indeed, by reducing the radius of the confining nuclear potential with decreasing energy, one may expect to raise the high-momentum content and generate the behavior predicted in Refs. [7, 50] and experimentally confirmed in [52]. Since the geometry of the DOM potential has been assumed independent of energy in the current implementations, this would increase the computational ef-

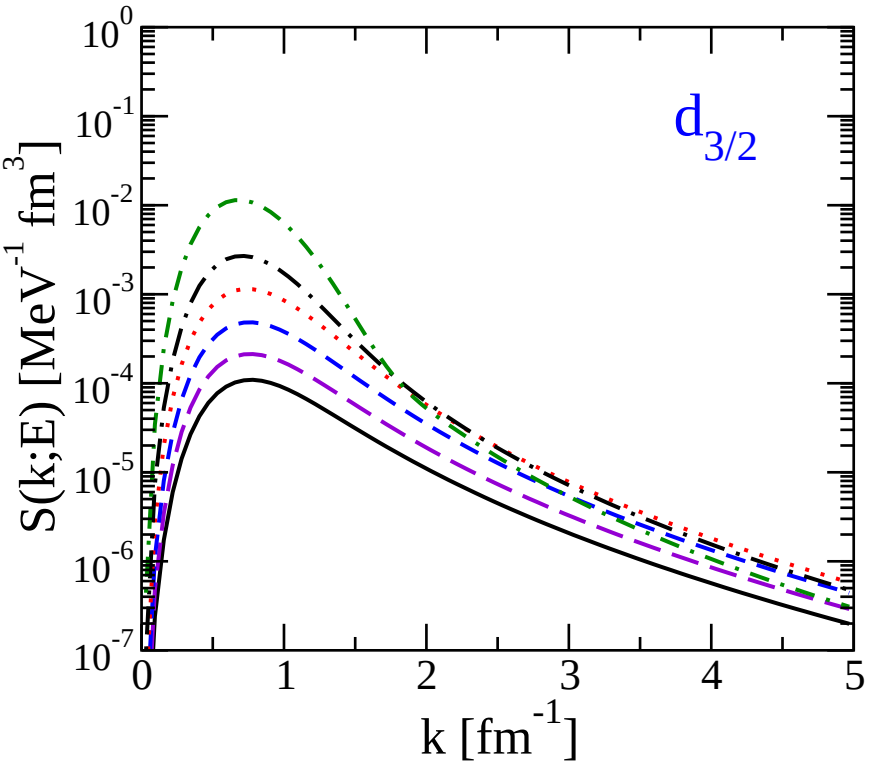

Figure 3.6: Momentum-space spectral function for $d_{3/2}$ quantum numbers at different energies. The highest curve is obtained at -25 MeV and each successive lower curve (at small momenta) represents a 25 MeV step lower in energy with the last curve representing the spectral function at -150 MeV. Published in Ref. [30].

fort substantially since the application of the subtracted dispersion relation would have to be performed also as a function of the coordinates for which the real part of the dispersive part is required. The work of Refs. [7, 50] was performed in momentum space and it may be necessary to consider DOM implementations which rely on momentum-space formulations, at least as far as SRC are concerned.

The missing ingredients in DOM for describing high-momentum components are relevant for the description of the nuclear charge density. As discussed in Ref. [53], the role of SRC is to remove some nuclear charge, present in the mean-field description in terms of the occupied $s_{1/2}$ states, from the origin to larger radii but not to the

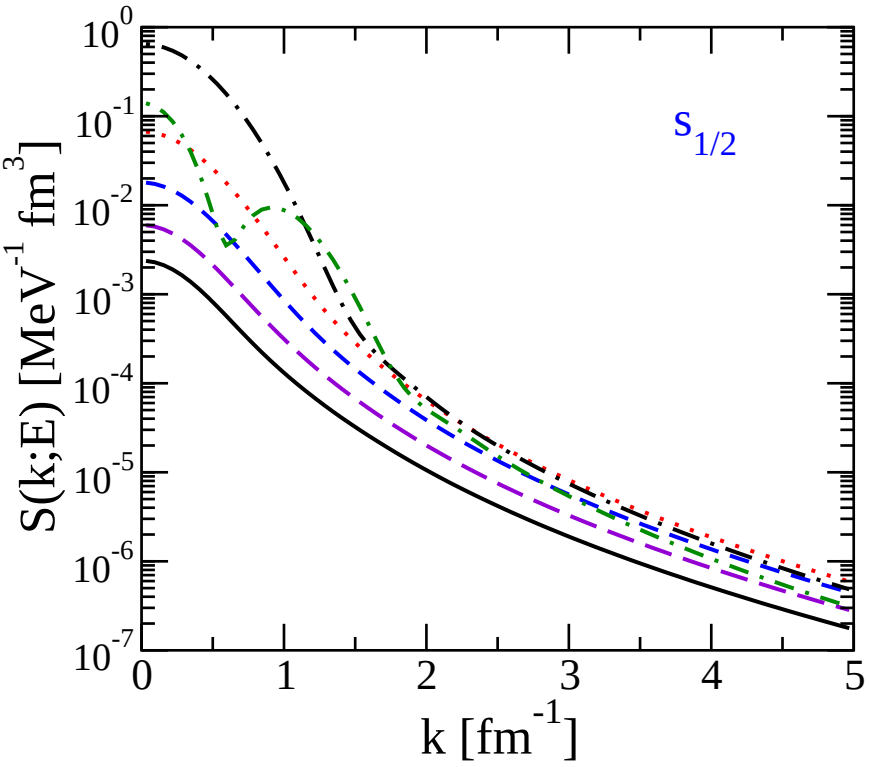

Figure 3.7: Momentum-space spectral function for $s_{1/2}$ quantum numbers at energies corresponding to the ones used in Fig. 3.6. Published in Ref. [30].

surface, which is dominated by quasihole contributions. While some of this charge returns to the origin as partially occupied higher $s_{1/2}$ states, most of this strength is associated with higher ℓ-values, similar to the results obtained in Refs. [7, 51]. It is therefore reasonable to expect that a proper treatment of SRC with the attendant presence of high-momentum (higher ℓ) components (constrained by the experimental data [52]) will make it possible to obtain an accurate fit to the nuclear charge density in a DOM framework.

3.2.5 Binding Energy per Particle

It is well known that the sp propagator allows for the calculation of the energy per particle from the contribution of the underlying two-body interaction. For the present case, it is useful to employ this result in momentum space. The energy per proton of the ground state can, for example, be obtained by calculating [36]

$$\frac{E(^{40}\mathrm{Ca})}{Z} = \frac{1}{2Z}\sum_{\ell j}(2j+1)\int_0^\infty dk k^2 \frac{k^2}{2m} n_{\ell j}(k) + \frac{1}{2Z}\sum_{\ell j}(2j+1)\int_0^\infty dk k^2 \int_{-\infty}^{\varepsilon_F} dE\ E S_{\ell j}(k;E). \tag{3.18}$$

With the present DOM potential only -2.91 MeV per proton was obtained, including the effect of the Coulomb interaction. A similar calculation for the neutrons yields -6.51 MeV per neutron for a total of -4.71 MeV per particle. This result represents about 60% of the experimental result. This is a remarkable result since the spectral information and the location of the bound levels in combination with a considerable wealth of elastic scattering data is described by the DOM self-energy. However, also in this case addressing the incorrect description of high-momentum components in the DOM may resolve this issue. In Ref. [7] it was shown that the quasihole contribution to the energy per particle is about 35% in ^{16}O whereas 65% is generated by the continuum contribution at large negative energies where high-momenta dominate. This result is noteworthy also since only 10% of the nucleons are considered to have high momenta as confirmed by experiment. A similar situation appears to apply in the case of the DOM analysis of ^{40}Ca. Since the total number of high-momentum components appears reasonable, it suggests that their appearance at more negative energy will be able to resolve part of the discrepancy for the total energy of the ground state. It must also be noted that an important contribution from three-body forces may have to be considered. It appears therefore reasonable to expect that all data that are not yet well reproduced at present, can be better described in a future DOM implementation which incorporates the contribution of about 10% of high-momentum

nucleons with the correct energy dependence.

3.3 Other Isotopes

3.3.1 Extrapolations

An important goal of the DOM is to extrapolate to exotic nuclei based on global fits to data. As mentioned already, the above analysis was done using the DOM potential from Ref. [23], which was obtained from fitting only calcium data. This potential was extrapolated out to ^{60}Ca, but it was found that the surface imaginary potential for neutrons, $\mathcal{W}_s^n$, eventually changed sign, indicating creation of neutrons instead of absorption. This unphysical creation of particles resulted from using a standard Lane-type potential [54] for the asymmetry dependence of $\mathcal{W}_s^n$ and $\mathcal{W}_s^p$. In a Lane-type potential the depth is given by

$$V^{p,n} = V_0 \pm \frac{N-Z}{A} V_1$$

where the $+$ is for protons and $-$ is for neutrons (assuming $N > Z$). So, when $\mathcal{W}_s^n$ was extrapolated to more neutron rich nuclei, the potential depth changed sign. Thus, the Lane-type potential often used for the surface imaginary potential was called into question.

In order to constrain the asymmetry dependence of the neutron imaginary potential, an experiment was done to measure neutron elastic-scattering differential cross sections on ^{48}Ca [24]. These data were then included in a DOM fit to data from nuclei with $N = 28$, $Z = 20, 28$ [24]. No asymmetry dependence for $\mathcal{W}_s^n$ and $\mathcal{W}_s^p$ was assumed. Instead, the parameter controlling the height of the surface imaginary potential was adjusted separately for neutrons and protons in each nucleus, allowing the asymmetry dependence to be constrained by data. In addition, separate fits were performed for nuclei with $Z = 50$ and $Z = 82$. In this section, the fit with the lighter nuclei is denoted FIT1, with the tin isotopes FIT2, and with the lead FIT3. Some

aspects of these fits are discussed in the following subsections.

Calcium Isotopes

For the Ca isotopes, both $\mathcal{W}_s^n$ and $\mathcal{W}_s^p$ exhibited a more complicated asymmetry dependence than the simple linear relationship predicted by a Lane-type potential. In particular, the strength of $\mathcal{W}_s^n$ increased from ^{40}Ca to ^{42}Ca, but the strength for ^{48}Ca was about the same as that of ^{40}Ca. The method of extrapolation to more neutron rich nuclei is then less straightforward.

Nonetheless, based on isospin symmetry, one may naively expect the asymmetry dependence of the surface imaginary potential of protons in Ca isotopes with $(N < Z)$ to follow a similar pattern as for the surface imaginary potential of neutrons in Ca isotopes with $(N > Z)$, and vice versa. Therefore, the DOM potential from FIT1 was extrapolated to ^{36}Ca, for which proton and neutron knockout experiments have been performed recently [55].

For the neutrons, the height of $\mathcal{W}_s^n$ was adjusted to the same height as $\mathcal{W}_s^p$ in ^{44}Ca. Since $\mathcal{W}_s^n$ for the $N > Z$ isotopes did not exhibit a strong asymmetry dependence, the height of $\mathcal{W}_s^p$ in ^{36}Ca was adjusted to the same height as for protons in ^{40}Ca. The calculated spectroscopic factors are shown in Table 3.4. In Fig. 3.8 the spectroscopic factors for the valence hole levels of the minority nucleon species as a function of $(N - Z)/A)$. Both the local and nonlocal implementations of the DOM give a mild decrease in the neutron spectroscopic factor, in contrast to the more drastic decrease suggested by the neutron knockout experiment discussed in [55].

Knockout experiments on various rare isotopes have consistently yielded small spectroscopic factors for the minority species [56], and there has been much debate over the reason for this result. One possible explanation is that for increasing neutron-proton asymmetry, coupling to the continuum can become important. Indeed, it was shown in Ref. [57] that taking into account coupling to the continuum causes a significant reduction in the spectroscopic factors of the valence protons in neutron-rich oxygen isotopes.

Table 3.4: Spectroscopic factors for the proton and neutron valence hole levels in ^{36}Ca. The second column gives the results from using the DOM with a nonlocal volume HF piece, and the third column gives the results using the purely local form of the DOM. The last column shows the spectroscopic factors extracted from proton and neutron knockout experiments [55].

Species	Nonlocal DOM	Local DOM	Exp.
π	0.70	0.72	0.75
ν	0.65	0.67	0.22

As the valence nucleons of the majority species become less bound, the threshold energy needed for a hole to couple to a 2h1p excitation moves closer to the energy of the valence hole. For example, as one approaches the neutron drip-line, the energy required to remove a neutron becomes increasingly smaller, and so the energy required for a proton hole to couple to a neutron particle-hole state also becomes smaller. Furthermore, because the neutron particle in the intermediate state is in the continuum, there are many more ways for a proton hole to couple to 2h1p states, resulting in a greater reduction of sp strength. The effect of the continuum on the strength with which a hole can couple to a 2h1p state is illustrated in Fig. 3.9 for the specific case of a proton hole.

This effect was explored in the DOM by varying the threshold energy, ε_{thresh}, of the imaginary part of the self-energy. The distance of this threshold energy from ε_F was given by,

$$\Delta^{(i)}_{thresh} = C\left(\frac{\Delta_i}{2} + min(\Delta_n, \Delta_p)\right), \tag{3.19}$$

where $i = n, p$ denotes either a neutron or a proton and Δ_i are neutron and proton particle-hole gaps, i.e.,

$$\Delta_i = \varepsilon_F^{(i)+} - \varepsilon_F^{(i)-}. \tag{3.20}$$

C is a parameter that takes into account the effects of correlations on Δ_{thresh}. In the IPM, $C = 1$, and the maximum energy for which a hole can couple to a 2h1p excitation is $\varepsilon_{thresh} = \varepsilon_F^- - min(\Delta_n, \Delta_p)$. This form neglects the interaction among

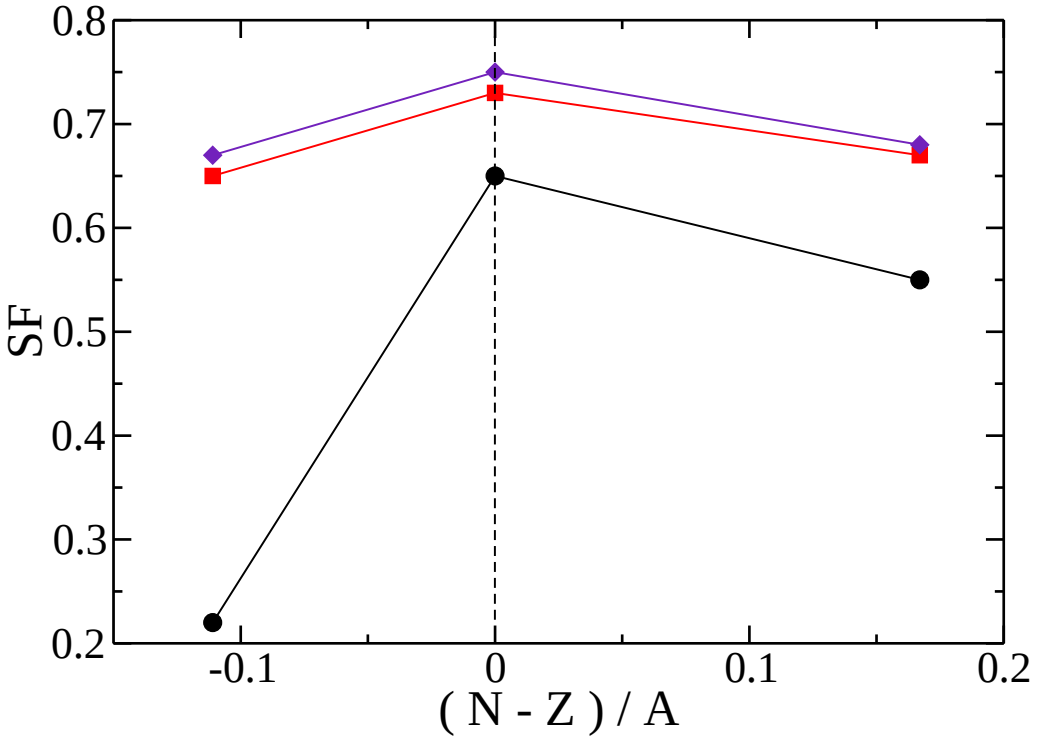

Figure 3.8: Spectroscopic factors for the valence holes of the minority species in the Ca isotopes obtained from experiment (circles), nonlocal DOM (squares) and local DOM (diamonds). The points to the left of the dashed vertical line are for the neutron holes in ^{36}Ca, while the middle points and those to the right are for the proton holes. The circle to the left is from the neutron knockout experiment in Ref. [55], and the other circles are from $(e, e'p)$ experiments [6].

the intermediate particle and hole states. This interaction tends to reduce Δ_{thresh}, and in Ref. [24] the parameter C was set to 0.8. However, the value of Δ_{thresh} in ^{36}Ca may be very different from the value given by this prescription.

In general, the closer the 2h1p excitation is to the hole state, the stronger the coupling strength will be. Therefore, it is useful to define $\Delta = |\varepsilon_{thresh} - \varepsilon_F^-|$. In Fig. 3.10, the spectroscopic factor of the neutron $1s_{1/2}$ hole of ^{36}Ca is shown as a function of Δ. The value of $\Delta = 3.0$ MeV corresponds to the DOM result from

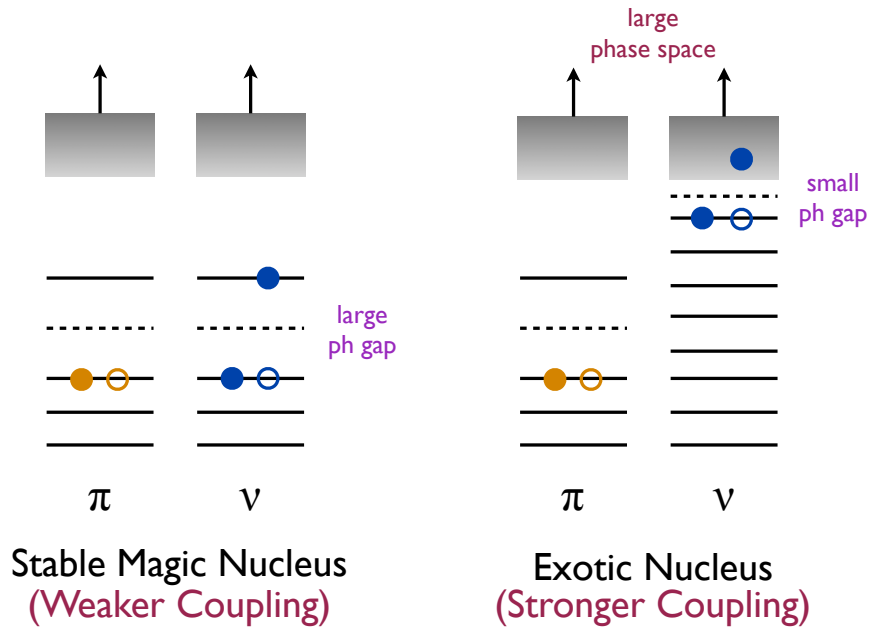

Figure 3.9: Schematic level diagrams illustrating the effect of the continuum on the coupling of a proton hole to 2h1p a state. Solid lines indicate shell-model energy levels and dashed lines show the Fermi energies. For both level diagrams, the proton levels are on the left (orange) and the neutron levels are on the right (blue). Holes are indicated by unfilled circles and the levels below the valence hole levels are assumed to be fully occupied. The continuum is represented by a gray area.

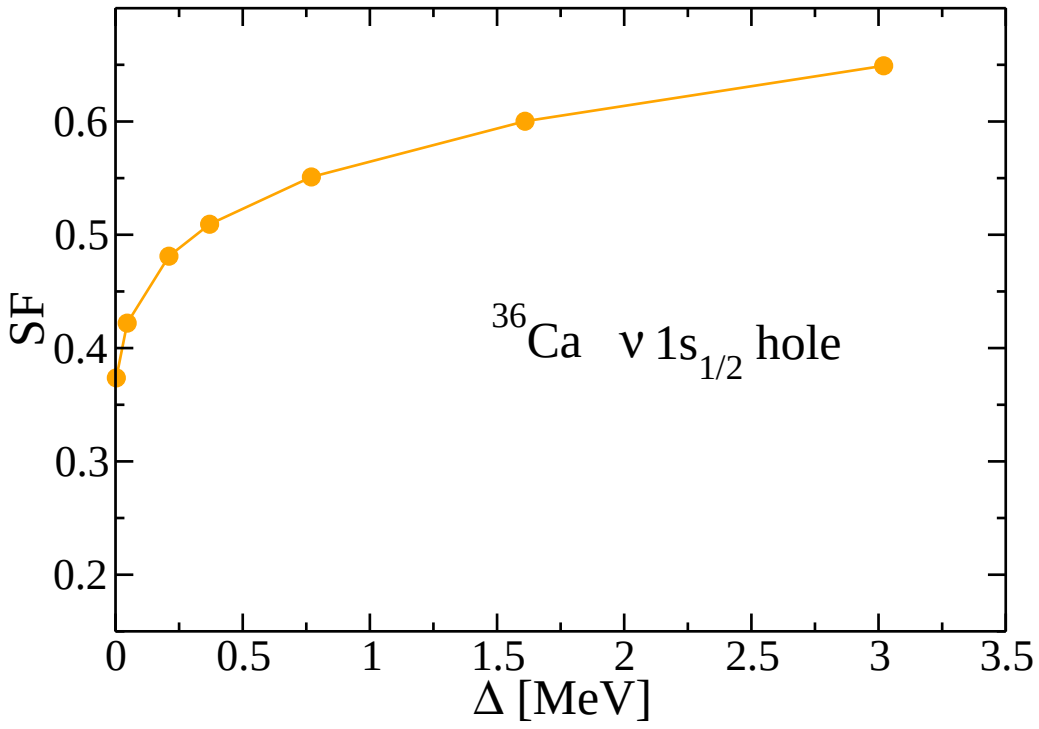

Figure 3.10: Spectroscopic factor of the neutron $1s_{1/2}$ hole state of ^{36}Ca as function of Δ, the energy interval between the threshold energy for the imaginary potential at negative energies and the $1s_{1/2}$ hole state.

Ref. [24], which is obtained by using Eq. (3.19) with $C = 0.8$.

The smaller values of Δ show that the DOM has the capability to take coupling to the continuum into account. As Δ decreases, the number of 2h1p and 2p1h states in the neighborhood of ε_F increases. Thus, sp strength is leaked from the quasihole state to more complicated states and the spectroscopic factor is reduced. This physics is illustrated in Fig. 3.11, which shows the spectral strength distribution of the neutron $1s_{1/2}$ hole for various values of Δ. The dashed line corresponds to $\varepsilon_{1s_{1/2}}$.

The problem with the above explanation for the small spectroscopic factor, at least in the framework of the DOM, is that when Δ is decreased, the proton spectroscopic factor of the $0d_{3/2}$ hole state is also heavily reduced; but this reduction

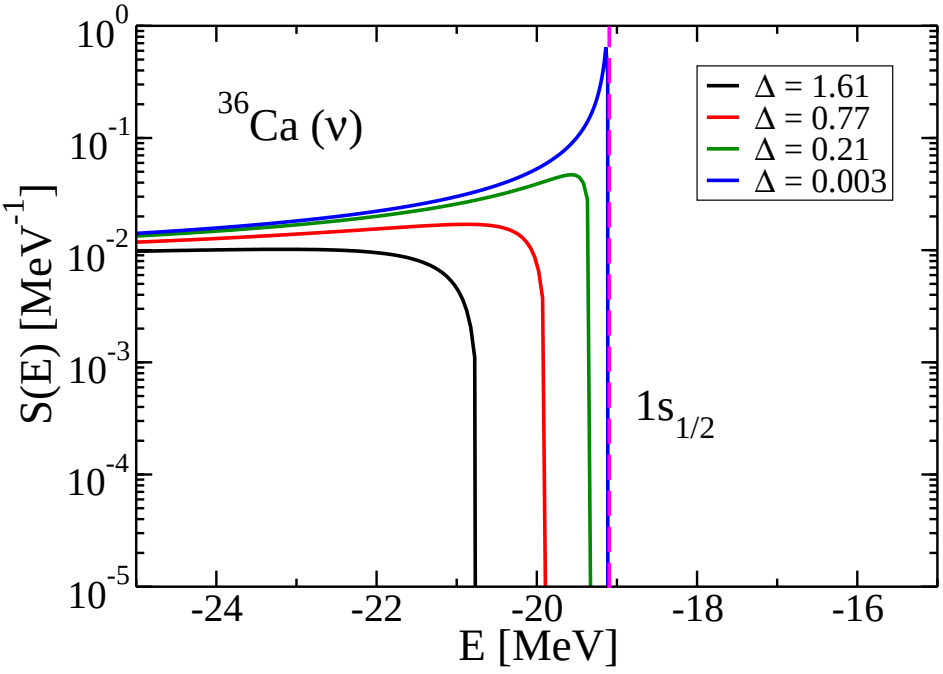

Figure 3.11: Spectral strength of the neutron $1s_{1/2}$ hole state of ^{36}Ca for different values of Δ.

is not observed experimentally (see Table 3.4). In fact, the experimentally inferred spectroscopic factors for the majority species in nuclei close to the drip-line are more in line with what one sees in stable closed-shell nuclei. One possible explanation for the apparent insensitivity to the continuum could be that the valence protons are halo-like, resulting in a decreased interaction with the other nucleons. Thus, the coupling to the continuum could be stronger for the valence neutrons than for the valence protons. This effect was tested within the DOM framework by increasing the radius parameter and adjusting the depth in order to get the $0d_{3/2}$ proton hole in ^{36}Ca correct. It was found that by making proton $0d_{3/2}$ wave function more extended increased the spectroscopic factor.

According to recent coupled-cluster calculations [58], the effect of the continuum on the sp states of ^{17}F, whose first excited state is a halo nucleus [58, 59], and

^{17}O was shown to be comparable. Therefore, a similar set of calculations involving a nucleus with a greater neutron-proton asymmetry would be interesting. Nevertheless, both DOM fits and experiments indicate that for increasingly asymmetric nuclei, the nucleons of the minority species experience more correlations, which is implied by the decreasing spectroscopic factors (see Fig. 3.8).

Before turning to the heavier elements in the next section, it is worth mentioning that the spectroscopic factors from Ref. [23] are about 0.1 smaller than those from Ref. [24] and thus more in line with $(e, e'p)$ experiments (the two circles furthest to the right in Fig. 3.8). This difference is mainly due to different implementations of the surface imaginary potential. In Ref [23] the surface imaginary potential is stronger at energies in the neighborhood of ε_F, and calculated spectroscopic factors are quite sensitive to the strength of the imaginary potential in this energy region, as can be seen in Fig. 3.10.

In microscopic calculations the self-energy has discrete poles near ε_F, and these poles enhance the coupling of the quasihole and quasiparticle states to more complicated states. The higher spectroscopic factors in Ref. [24] suggest, then, that the imaginary potential near ε_F is too weak and that the DOM potential in Ref. [23] probably provides a better description of the surface physics in the energy region around ε_F. In future implementations of the DOM, this issue should be investigated in more detail.

Tin Isotopes

Data from proton scattering on ^{112,114,116,118,120,122,124}Sn and from neutron scattering on ^{116,118,120,124}Sn were included in FIT2. In contrast to FIT1, both $\mathcal{W}_s^n$ and $\mathcal{W}_s^p$ did exhibit a linear dependence on $(N-Z)/A$ [24], allowing for more straightforward extrapolations. As in a Lane-type potential, the asymmetry dependence for neutrons was found to have a negative slope, while that for the protons was found to have positive slope. However, unlike a Lane-type potential, the asymmetry dependence for neutrons was much weaker than that for protons.

The nonlocal DOM results were obtained by fitting the charge radii of ^{112}Sn and ^{124}Sn. It is known that an $A^{1/6}$ radial dependence for the proton potential describes the experimental charge radii of the tin isotopes [60] much better than an $A^{1/3}$ dependence. So, in fitting the nonlocal HF term, an $A^{1/6}$ dependence was assumed for the protons, but an $A^{1/3}$ dependence was maintained for the neutrons. The radial parameters for neutrons (r_0) and protons (r_0') were chosen so that at ^{112}Sn the radius of the neutron HF potential coincided with the radius of the proton HF potential, i.e., $r_0 A^{1/3} = r_0' A^{1/6}$. The parameters of the nonlocal HF potential were adjusted to reproduce the charge radius of ^{112}Sn, and the resulting charge radius of ^{124}Sn was 4.76 fm, compared with the experimental value of 4.677 ± 0.001 fm [48]. The neutron and spin-orbit corrections to the charge density were both taken into account [41].

One rare isotope of interest is ^{132}Sn, which in the nuclear shell-model picture would be expected to be a doubly-magic nucleus, with a magic number of 50 for the protons and 82 for the neutrons. In exotic nuclei, however, experiments point to the disappearance of standard shell model magic numbers [61] and the appearance of new magic numbers, such as $N = 14$ in ^{22}O [13]. Testing magic numbers in exotic nuclei, then, is an important way of testing our understanding of nuclear structure, which is essential for understanding the processes responsible for nucleosynthesis (such as the r-process).

Experimentally, ^{132}Sn has shown properties that are characteristic of a doubly-closed shell nucleus. For example, K.L. Jones *et al.* studied the neutron sp states in ^{133}Sn with the transfer reaction $^{132}\mathrm{Sn}(d,p)^{133}\mathrm{Sn}$ in inverse kinematics [62]. The data were analyzed using finite-range DWBA, and the extracted spectroscopic factors were on the order of unity. Small spectroscopic factors imply highly fragmented sp states, which occur as a result of correlations with the surrounding nucleons. A nucleon moving outside a closed shell, however, is expected to experience fewer correlations and thus have a spectroscopic factor closer to what is obtained in the IPM. The results in [62], then, indicate the magic nature of ^{132}Sn.

In Ref. [20], the $^{132}\mathrm{Sn}(d,p)^{133}\mathrm{Sn}$ reaction was analyzed using the finite-range adi-

Table 3.5: Energy levels for sp neutron levels in ^{133}Sn. Energies are in MeV

Level	Exp.	local DOM	nonlocal DOM
$1f_{7/2}$	-2.47	-2.47	-2.47
$2p_{3/2}$	-1.62	-1.54	-1.41
$2p_{1/2}$	-1.11	-0.98	-0.80
$1f_{5/2}$	-0.46	-0.42	-0.22

Table 3.6: Spectroscopic factors for sp neutron levels in ^{133}Sn.

Level	FR-ADWA-CH	local DOM	nonlocal DOM
$1f_{7/2}$	1.0	0.80	0.77
$2p_{3/2}$	0.92	0.86	0.83
$2p_{1/2}$	1.2	0.86	0.84
$1f_{5/2}$	1.2	0.81	0.74

abatic wave approximation (FR-ADWA), which uses nucleon optical potentials as input instead of the more ambiguous deuteron optical potential used in DWBA analyses. Using the CH89 optical potentials, slightly different spectroscopic factors were obtained, but were still on the order of unity within experimental uncertainties. The experimental energy levels of neutrons added to the ^{132}Sn core are shown in Table 3.5 and compared with those calculated with the DOM. In Table 3.6, the corresponding spectroscopic factors are presented. The column labeled FR-ADWA-CH indicates the spectroscopic factors extracted using FR-ADWA with CH89 optical potentials. This information is shown graphically in Fig. 3.12.

The energy levels generated by the DOM track the experimental levels quite well, once the potential depth is adjusted to reproduce the ground state level of ^{133}Sn. The excited levels calculated using the nonlocal DOM are slightly smaller than the levels calculated using the local DOM, but this difference is likely a result of using a smaller diffuseness in the nonlocal DOM than in the local version. However, the fit of the nonlocal HF term was not optimized, so a different choice of parameters could result

in a better agreement with experiment.

The spectroscopic factors obtained with the DOM are about 20-30% lower than those obtained with FR-ADWA and using CH89 optical potentials. The overlap function for the added neutron is also needed in an FR-ADWA analysis, and in Ref. [20] an overlap function generated with a Woods-Saxon potential was used. In Ref. [31] an FR-ADWA analysis using the DOM potentials as input was performed for the ^{132}Sn$(d,p)^{133}$Sn reaction. Using an overlap function generated with a Woods-Saxon potential resulted in a slightly reduced spectroscopic factor for the $1f_{7/2}$ orbital compared to the CH89 result. However, it was found that the spectroscopic factor was

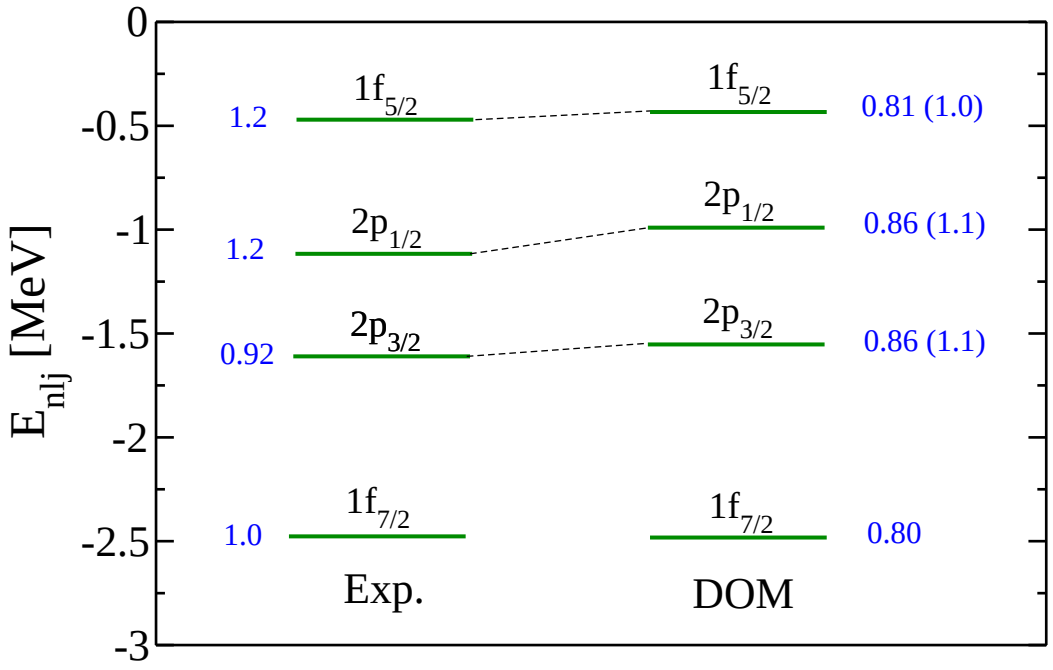

Figure 3.12: Comparison of energy levels of neutrons in ^{133}Sn obtained experimentally and with the DOM. The spectroscopic factors obtained with FR-ADWA-CH and the local DOM are also compared. The spectroscopic factors in parentheses (on the right) show what the DOM spectroscopic factors would be if the $1f_{7/2}$ spectroscopic factor were scaled to 1.

reduced further by about 30% when a DOM overlap function was used instead. The main difference between the two overlap functions is that the DOM overlap function contains a correction for nonlocality. The results from using FR-ADWA with DOM potentials for various (d, p) reactions on stable nuclei is discussed in greater detail in the next chapter.

Since spectroscopic factors are an indicator of the degree of shell closure, a comparison of the spectroscopic factors of the neutron particle states of ^{132}Sn with those of a doubly magic nucleus that is stable is instructive. In Ref. [62] a comparison between ^{208}Pb and ^{132}Sn was made, and the spectroscopic Pb spectroscopic factors were found to be generally smaller than those in Sn, implying that ^{132}Sn has a stronger shell closure than ^{208}Pb.

In Fig. 3.13, a comparison between ^{132}Sn and ^{208}Pb is also made, but with spectroscopic factors calculated with nonlocal DOM potentials. The spectroscopic factors in Pb are also generally smaller than those in Sn, but not to the same extent as in Ref. [62]. The smaller spectroscopic factors in Pb are probably due to the higher angular momentum states. States with higher angular momentum are suppressed in the interior due to the centrifugal barrier and enhanced in the surface region, which is where the surface imaginary potential is strongest [24]. States with higher ℓ then couple more strongly to long-range correlations, resulting in smaller spectroscopic factors.

Occupation Numbers and Correlations

As discussed in the previous section, the DOM fit with Sn data favored a surface absorption for protons that increased linearly with increasing $(N - Z)/A$. As a result, the spectroscopic factors show a corresponding decrease with $(N - Z)/A$. The first column in Table 3.7 shows the spectroscopic factors of the $0g_{9/2}$ proton hole calculated using the nonlocal version of the DOM for various isotopes. In going from ^{102}Sn to ^{130}Sn, the proton spectroscopic factors go from 0.80 to 0.48. In ^{132}Sn the spectroscopic factor increases to 0.56 due to a large particle-hole gap. The overall

trend, however, is consistent with the notion that the valence nucleons of the minority species in asymmetric nuclei experience more correlations with increasing asymmetry, which is also supported by knockout and $(e, e'p)$ reactions [63].

Occupation numbers for valence nucleons, on the other hand, should show a smaller decrease than the spectroscopic factors. The imaginary potential above ε_F is responsible for removing strength below ε_F, decreasing the occupation; but the imaginary potential below ε_F removes strength from near ε_F and puts it back at lower energies. So, while sp strength around ε_F is reduced by the imaginary potential above and below ε_F, the occupation is only reduced by the part above ε_F.

All the DOM implementations thus far have assumed the surface absorption to be symmetric about ε_F. Since most of the asymmetry dependence of the absorption comes from the surface term $\mathcal{W}_s$, one would expect that roughly half of the reduction of the spectroscopic factors comes from the surface absorption for $E < \varepsilon_F$ and half from the surface absorption for $E > \varepsilon_F$. The reduction in the occupation number, then, should be about half of the reduction in the corresponding spectroscopic factor, and inspecting columns 1 and 3 in Table 3.7 one can see that this is roughly the case for the $0g_{9/2}$ proton hole.

The second column shows n^c_{nl}, the contribution of the occupation due to the continuum states, which occur at lower energies. The total occupation is just the sum of this contribution and the spectroscopic factor. The increase in n^c_{nl} for increasing neutron number shows that the stronger the surface absorption the more sp strength is moved to lower energies. This effect is also illustrated in Fig. 3.14, which shows the spectral strength distribution for the isotopes listed in Table 3.7. As neutron number increases, the spectral strength increases in the first 40 MeV or so below ε_F, which is roughly the energy region where the surface imaginary potential dominates.

The last two columns in Table 3.7 show the total occupations (n_l) and spectroscopic factors (S_l) calculated using the local version of the DOM, which employed approximate forms for these quantities. The spectroscopic factors S_l were calculated using Eq. (2.50) and are in agreement with those calculated using Eq. (2.31). The n_l

Table 3.7: Spectroscopic factors (relative to the IPM predictions) and occupation numbers n for the $0g_{9/2}$ proton orbit in Sn isotopes using the nonlocal (NL) and local (L) versions of the DOM.

Isotope	S_{NL}	n^c_{NL}	n_{NL}	n_L	S_L
102	0.80	0.11	0.91	0.86	0.79
106	0.68	0.17	0.85	0.81	0.68
112	0.63	0.20	0.83	0.74	0.63
124	0.50	0.28	0.78	0.62	0.51
130	0.48	0.30	0.78	0.60	0.49
132	0.56	0.25	0.81	0.65	0.56

occupation numbers were calculated using

$$N_{n\ell j} = \int_0^\infty \mathrm{d}r \bar{\varphi}^2_{n\ell j}(r) \left[1 + \frac{m}{\tilde{m}(r, E_{n\ell j})} \frac{1}{\pi} \int_{E_F}^\infty \mathrm{d}E' \frac{\mathcal{W}(r, E')}{(E' - E_{n\ell j})^2}\right], \tag{3.21}$$

which was an approximation proposed by Mahaux and Sartor [22]. However, these occupation numbers show a decrease with increasing neutron number that is similar to the decrease in the spectroscopic factors. Thus, Eq. (3.21) is not a good approximation when the imaginary potential is too strong and thus may not be appropriate for extrapolations to proton or neutron drip-lines.

3.3.2 Other Ground-state Properties

The binding energy per particle for some of the isotopes studied with the DOM are listed in Table 3.8 and compared with experiment. The DOM results for the heavier isotopes are more poorly described than the lighter ones. Note that the ^{40}Ca results are slightly different from the ones quoted in Sec. 3.2. This difference is a result of using the DOM potential in [24] instead of the one in [23].

In Fig. 3.15 the calculated charge distributions of ^{124}Sn and ^{208}Pb (normalized to the correct proton number) are compared with their respective experimental distributions. As in the case of ^{40}Ca, the DOM results place too much charge at the

Table 3.8: Binding energies per particle for various isotopes. The binding energies are in MeV. The proton and neutron contributions to the binding energy are presented in the last two columns.

Isotope	Exp.	DOM	DOM / Exp.	DOM(π)	DOM(ν)
^{36}Ca	7.82	4.10	0.52	0.42	7.88
^{40}Ca	8.55	4.50	0.53	2.01	6.95
^{48}Ca	8.67	5.24	0.60	7.04	3.88
^{112}Sn	8.51	4.03	0.47	3.67	4.37
^{124}Sn	8.47	3.25	0.38	4.70	2.21
^{132}Sn	8.36	3.58	0.43	5.70	2.07
^{208}Pb	7.87	2.89	0.37	2.92	2.87

origin.

3.4 Beyond Nonlocal HF Description

It has been shown in this chapter that replacing the traditional local but energy-dependent HF term with a nonlocal but energy-independent one improves the description of bound-state information, such as particle number, deeply-bound states, and occupation numbers. Moreover, employing this nonlocal energy-independent HF term provides access to quantities–such as spectral functions, charge densities, and total energy–that are important for studying nuclear structure. Indeed, the study of these quantities for ^{40}Ca revealed ways in which the DOM can be further improved.

One issue that still needs to be addressed is particle number. The local version of the DOM greatly overestimates particle number and the inclusion of the nonlocal HF term produces much more reasonable results. However, the current nonlocal implementation still overestimates particle number due to the assumed state independence of the imaginary potential, which means that the occupation of nominally empty states converges too slowly with increasing ℓ. For example, in ^{112}Sn the calculated proton number is $Z_{calc} = 51.0$ when only ℓ waves up to $\ell_{max} = 4$ are included. However, when $\ell_{max} = 6$ then $Z_{calc} = 57.2$. This problem becomes worse as the strength

of the imaginary potential increases, as it does for protons in ^{124}Sn. When $\ell_{max} = 6$ is used for this nucleus then $Z_{calc} = 60.4$.

Another challenge for the DOM is to be able to correctly take into account SRC. The DOM can generate high-momentum components, as shown for the case of ^{40}Ca; but these components are not found at very low energies, resulting in binding energies that are too low.

One other area that needs improvement is the description of the charge density. The current nonlocal version of the DOM produces a charge distribution for ^{40}Ca that has too much density in the central region, and this problem is present for the heavier isotopes as well.

As mentioned already, a correct treatment of SRC may improve the description of the charge distribution, and this might mean making the radius of the potential energy dependent. However, a preliminary DOM fit using a nonlocal imaginary potential suggests that the DOM is flexible enough to fit the interior part of the charge density without resorting to an energy dependent radius. Only bound-state data were fit, though, so the imaginary potential was not well constrained. Work is being done to include scattering data in a fit with nonlocal potentials.

One way to begin addressing these issues is to compare the DOM self-energy with microscopic calculations of the self-energy. Recent studies comparing microscopic and DOM self-energies [32, 33] indicate, for example, that the strength of the imaginary part of the microscopic self-energy decreases quickly with increasing ℓ. They also suggest that this decrease is due in large part to the nonlocality of the imaginary part. These studies will be discussed in Chs. 5 and 6.

Before turning to these studies, however, application of the DOM to transfer reactions is discussed in the next chapter. In this study, only the local version of the DOM is used.

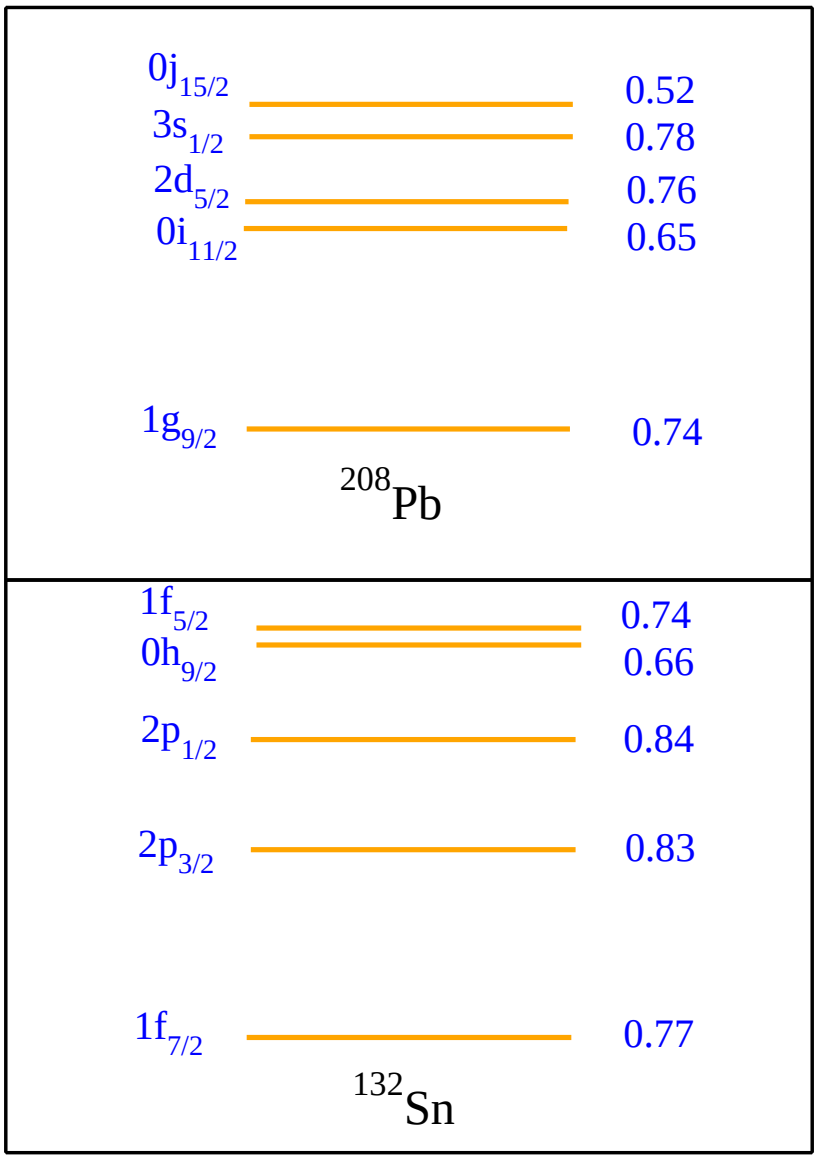

Figure 3.13: *Top Panel*: sp neutron states above the ^{208}Pb core. *Bottom Panel*: sp neutrons states above the ^{132}Sn core. In each panel, the levels are labeled on the left and the corresponding spectroscopic factors are given on the right. The levels and numbers are from the nonlocal DOM.

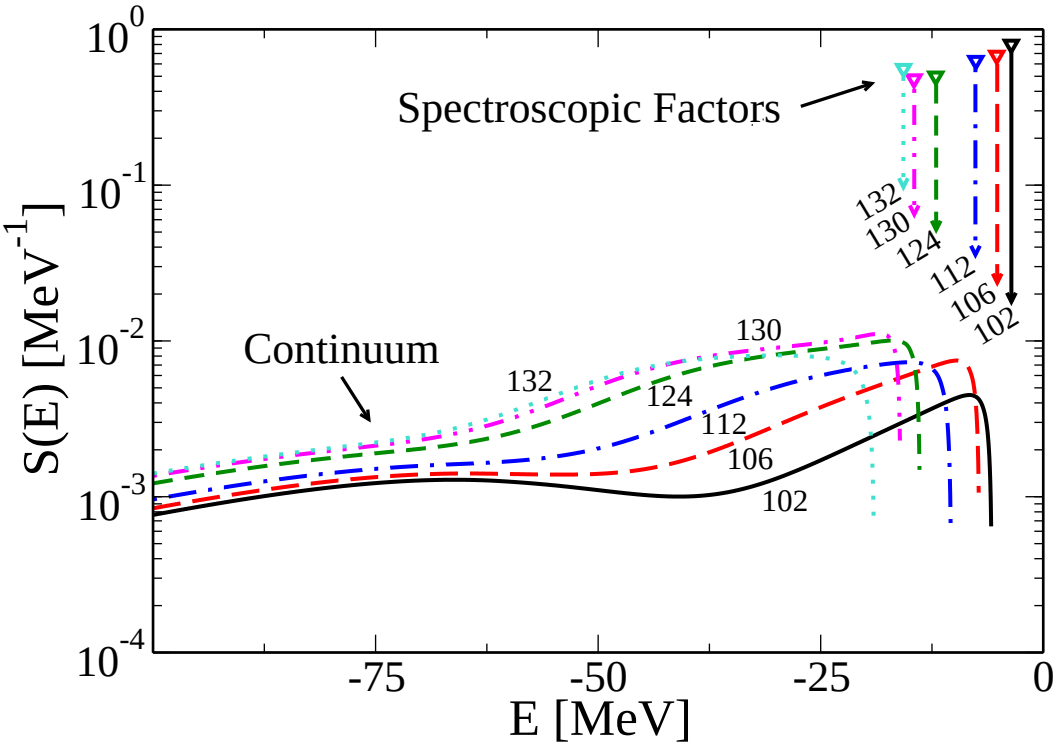

Figure 3.14: Strength functions of the $0g_{9/2}$ proton orbit in different Sn isotopes obtained with the nonlocal calculations. The curves represent the continuum contribution of the strength function and are labeled by the appropriate mass number. Also indicated is the location of the the $0g_{9/2}$ quasihole level in the different isotopes. The height of the corresponding vertical lines identifies the spectroscopic factor for each isotope. Published in Ref. [24].

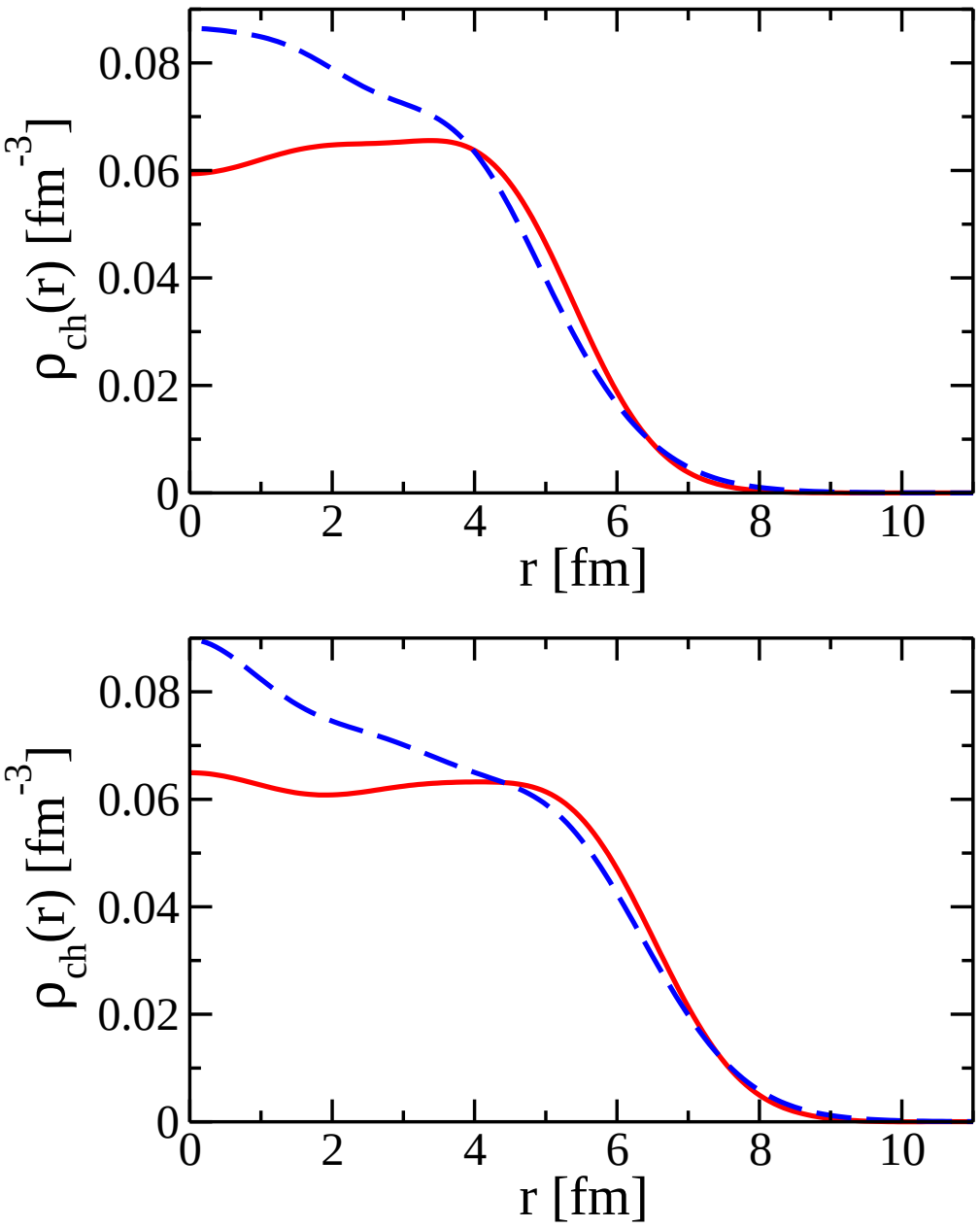

Figure 3.15: *Top Panel*: Experimental ^{124}Sn charge density (solid red) compared with the nonlocal DOM result (dashed blue). *Bottom Panel*: Experimental ^{208}Pb charge density (solid red) compared with the nonlocal DOM result (dashed blue).

Chapter 4

DOM and Transfer Reactions

4.1 Introduction

As seen in Ch. 3, the DOM can be used to extrapolate the empirical self-energy to exotic nuclei and predict properties related both to nuclear reactions and nuclear structure. This latter feature sets the DOM (especially its nonlocal version) apart from other optical models since they do not contain a clear relation between scattering and bound-state information. Of course, it is then important to compare the results from DOM extrapolations with experiment. Performing nucleon scattering experiments on exotic nuclei becomes less feasible as the nuclei become less stable, and nuclear reactions employing inverse kinematics are currently the most practical way of experimentally studying nuclei furthest from the valley of stability. Proton scattering and proton knockout experiments can be performed, for example, by directing a rare isotope beam onto a hydrogen target [64].

Transfer reactions are another set of important experiments which can be done in inverse kinematics. Since one can access both ground as well as excited states, these reactions provide a way to study shell structure, and by choosing appropriately the kinematic conditions, one can explore both the asymptotic (peripheral) and surface regions of the nuclear potential. In particular, the (d, p) and (p, d) reactions have been important in the study of neutron sp properties of rare isotopes. Examples of recent

studies include ^{132}Sn$(d,p)^{133}$Sn [62], ^{15}C$(d,p)^{16}$C [65], and ^{34,36,46}Ar(p,d) [66, 67].

A link between information obtained from one-nucleon transfer experiments and that contained in the DOM potentials is provided via the adiabatic wave approximation (ADWA), which depends on nucleon optical potentials as opposed to the more ambiguous deuteron optical potential used in DWBA analyses. The approximation was introduced by Johnson and Soper [18, 68] to take into account deuteron breakup to all orders, and was initially developed within a zero-range approximation (ZR-ADWA), in which the relative distance between the neutron and proton in the deuteron is assumed to be zero. Johnson and Tandy [69] later extended the ADWA to include fine-range effects (FR-ADWA), which have been shown to be important in (d,p) reactions [19].

Using the DOM optical-potentials as input in the ADWA, it may be possible to use (d,p) and (p,d) reactions to not only test DOM extrapolations, but also to use the data from these reactions to further constrain the DOM potentials. The purpose of this chapter is to evaluate the use of DOM potentials in FR-ADWA for (d,p) reactions. In particular, the following cases are analyzed: ^{40}Ca$(d,p)^{41}$Ca, ^{48}Ca$(d,p)^{49}$Ca, ^{132}Sn$(d,p)^{133}$Sn, and ^{208}Pb$(d,p)^{209}$Pb.

The results of the work presented below were produced in collaboration with F.M. Nuñes and N.B. Nguyen at Michigan State University. They provided the reaction codes and R.J. Charity, from Washington University, provided the DOM fits. I went to Michigan State University on two visits in order to assist with the interface between the reaction codes and the DOM potentials.

4.2 ADWA

The adiabatic theory of Refs. [68, 69] for $A(d,p)B$ starts from a three-body model of $n+p+A$. The deuteron scattering wavefunction in the incident channel is obtained

by solving the differential equation:

$$[E + i\epsilon - T_{\boldsymbol{r}} - T_{\boldsymbol{R}} - U_{nA} - U_{pA} - V_{np}]\Psi^{(+)}(\boldsymbol{r}, \boldsymbol{R}) = i\epsilon\phi_d(\boldsymbol{r}) \exp(i\boldsymbol{K}_d \cdot \boldsymbol{R}), \quad (4.1)$$

with $\boldsymbol{r} = \boldsymbol{r}_p - \boldsymbol{r}_n$ ($\boldsymbol{R} = (\boldsymbol{r}_n + \boldsymbol{r}_p)/2$) being the relative coordinate (center-of-mass coordinate) of the $n - p$ system. The neutron and proton coordinates, which are taken at the center of mass of the target A, are given by $\boldsymbol{r}_n$ and $\boldsymbol{r}_p$, respectively. $U_{nA}(\boldsymbol{r}_n)$, $U_{pA}(\boldsymbol{r}_p)$, and $V_{np}(\boldsymbol{r})$ are the neutron-target, proton-target, and neutron-proton interactions.

In this three-body approach, the solution of Eq. (4.1) is inserted into the exact transfer matrix element:

$$T = \langle \phi_{nA}\chi^{(-)}_{pB} | \, V_{np} + \Delta_{rem} \, |\Psi^{(+)}\rangle \ , \quad (4.2)$$

where ϕ_{nA} is the bound state of the neutron-target system, and $\chi^{(-)}_{pB}$ is a proton scattering distorted wave in the outgoing channel. The remnant operator is $\Delta_{rem} = U_{pA} - U_{pB}$. Contributions from this term are often small except for the lighter systems [19].

Solving Eq. (4.1) for the three-body wavefunction $\Psi^{(+)}(\boldsymbol{r}, \boldsymbol{R})$ is computationally expensive, but as Johnson and Tandy noted in [69], the exact three-body wavefunction is only needed within the range of the neutron-proton interaction V_{np}, as long as the remnant contributions are negligible. Within the range of this interaction, the three-body wavefunction can be expanded in terms of Weinberg states. In the current implementation of the FR-ADWA, only the first term in this expansion is used, and in [70] this truncation is found to give results within 10% of the exact solution of the three-body problem at forward angles, provided the deuteron energy is not too small or too large [70]. Nonetheless, the FR-ADWA appears to be valid for nuclei and energy regions that are of interest in this work.

4.3 Link with DOM

In this work, the Reid potential [71] was used for V_{np} and DOM potentials were used for U_{pA} and U_{nA}. According to standard practice, the DOM potentials for the incident channel were evaluated at half the deuteron kinetic energy E_d. This approximation is based on the assumption that low-energy, weakly correlated break-up states dominate in the transfer reaction [18].

A bound-state potential V_{nA} is also needed to generate the overlap function ϕ_{nA}. A Woods-Saxon potential with standard sp parameters (radius $r_0 = 1.25$ fm and diffuseness $a_0 = 0.65$ fm) and with a depth adjusted to reproduce the neutron binding energy is commonly used to generate ϕ_{nA}, but with the DOM this procedure is unnecessary since overlap functions are easily obtained from the DOM potential using Eq. (2.29). However, the potential depth of the volume HF term in the DOM was also adjusted to reproduce the neutron binding energy, since the angular distributions are very sensitive to this quantity.

Only purely local potentials were used for U_{pA}, U_{nA}, and U_{pB}, but the overlap function was calculated with both a purely local potential and a nonlocal potential, which was determined as outlined in [30] and discussed in detail in the previous chapter. The overlap function generated in the first way, but corrected for nonlocality per Eq. (2.47), is denoted as $\overline{\varphi}$, and the overlap function generated from the nonlocal potential is denoted as φ_{NL}. The overlap function generated with a local Woods-Saxon potential is denoted as φ_{WS}.

4.4 Results

4.4.1 Details of the calculations

The DOM potentials from Ref. [24] were used in the FR-ADWA framework to calculate the transfer cross sections of the outgoing proton for the reactions already mentioned above. The reader is reminded that the optical potentials for the Ca, Sn,

Table 4.1: Properties of overlap functions with a comparison among φ_{WS}, $\bar{\varphi}$, and φ_{NL}. The table includes the counting number n, the angular momenta (ℓj) of the valence orbital, the separation energy S_n and the root mean square radius of the valence orbital R^{rms}.

Nucleus	Overlap	$n\ell j$	S_n [MeV]	$R^{rms}[fm]$
^{41}Ca	φ_{WS}	$0f_{7/2}$	8.362	3.985
	$\bar{\varphi}$			3.965
	φ_{NL}			3.949
^{49}Ca	φ_{WS}	$1p_{3/2}$	5.146	4.606
	$\bar{\varphi}$			4.820
	φ_{NL}			4.759
^{133}Sn	φ_{WS}	$1f_{7/2}$	2.469	6.080
	$\bar{\varphi}$			6.513
	φ_{NL}			6.135
^{209}Pb	φ_{WS}	$1g_{9/2}$	3.936	6.498
	$\bar{\varphi}$			6.746
	φ_{NL}			6.704

and Pb nuclei were obtained with different parameter sets (see Sec. 3.3). The code TWOFNR [72] was used to calculate the finite-range deuteron adiabatic potential, and FRESCO [73] was used to calculate the transfer cross sections.

Throughout this section, the results obtained from using DOM potentials but using φ_{WS} for the overlap function are denoted by DOM+WS. The results obtained from using DOM potentials and using $\bar{\varphi}$ are denoted DOM+LBar, while those obtained from using φ_{NL} are denoted DOM+NL. Calculations were also done using the global optical-potential CH89 [16], and these are denoted by CH89+WS. Since CH89 does not include a dispersive correction, it cannot provide sensible bound-state information, which is why a Woods-Saxon potential was used for the overlap function.

The properties of the neutron states considered in this chapter are summarized in Table 4.1. The rms radii of $\bar{\varphi}$ and φ_{NL} are very similar except for ^{133}Sn, where φ_{NL} has a much lower R^{rms} than $\bar{\varphi}$. This discrepancy will be addressed later. Except for ^{41}Ca, both $\bar{\varphi}$ and φ_{NL} have larger rms radii than φ_{WS}. The DOM fit for Ca isotopes in Ref. [24] generated a radius parameter of 1.18 fm while the corresponding

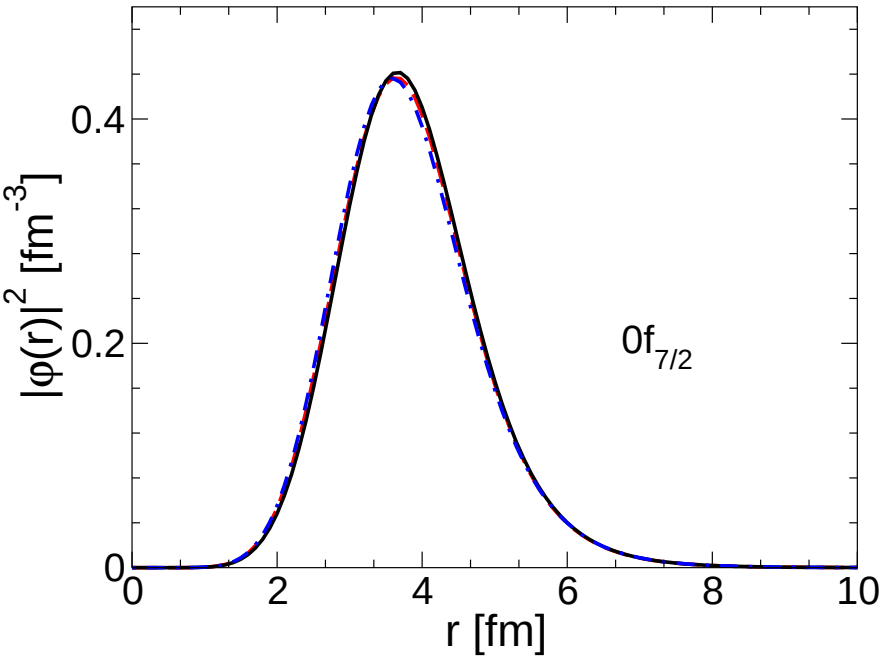

Figure 4.1: Comparison of the square of the single-neutron overlap functions for ^{41}Ca obtained with a Woods-Saxon potential φ_{WS} (solid), with the local DOM corrected for nonlocality $\bar{\varphi}$ (dashed), and with the DOM containing nonlocal HF term φ_{NL} (dot-dashed).

standard Woods-Saxon potential was fixed at 1.25 fm. The nonlocality correction almost completely cancels this difference, making both of the DOM overlap functions, $\bar{\varphi}$ and φ_{NL}, essentially identical to φ_{WS} (see Fig. 4.1). When a node is present, as for ^{49}Ca, the effects due to nonlocality are more pronounced, and Fig. 4.2 shows that the wavefunction corrected for nonlocality, $\bar{\varphi}$, is now more extended than its Woods-Saxon counterpart, even though the DOM radius parameter is still 1.18 fm. The same effect is seen in φ_{NL}, but the rms radius is slightly smaller.

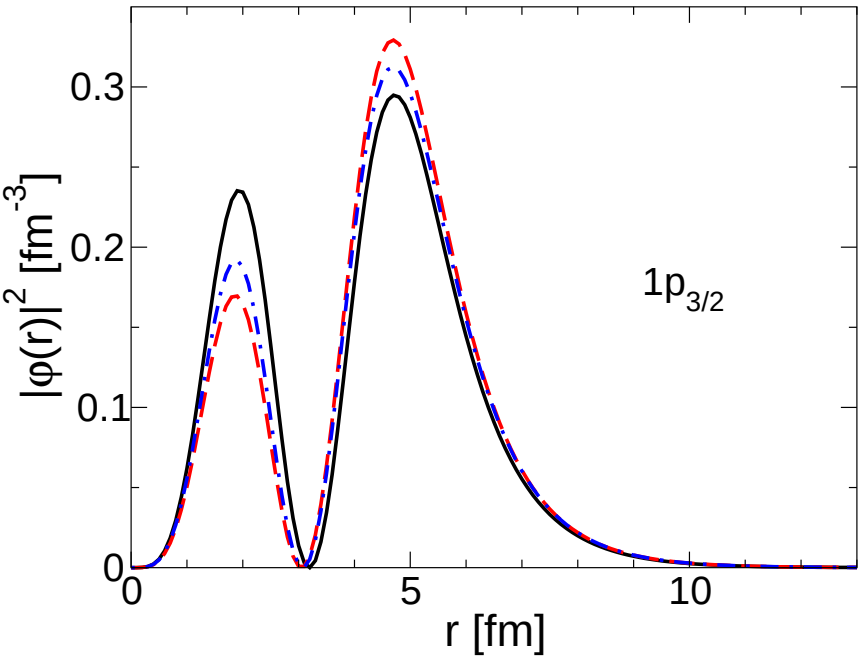

Figure 4.2: Same as in Fig. 4.1, but for ^{49}Ca.

The radius parameter resulting from the DOM fit to Sn nuclei is 1.24 fm, and therefore $\bar{\varphi}$ has an rms radius that is substantially larger than that of φ_{WS}. The overlap function generated from a truly nonlocal potential, φ_{NL}, has a significantly smaller rms radius than $\bar{\varphi}$. This difference could be a result of fitting the nonlocal potential to ^{124}Sn bound-state information first and then extrapolating to ^{132}Sn. As seen in Ch. 3, the radius parameter of the truly nonlocal HF potential tends to be somewhat less than the radius parameter corresponding to the local-equivalent potential. This effect is due in part to the enhancement of the dispersive correction, per Eq. (2.42), that is needed when the local- equivalent, but energy-dependent, HF term is replaced by a truly nonlocal one. Indeed, if the dispersive correction is not enhanced, then the radius parameter in the ^{40}Ca fit needs to be increased from 1.09 to 1.12 fm in order to reproduce the rms charge radius.

It is interesting to note that the rms radius of φ_{NL} for ^{49}Ca is also less than the rms radius of $\bar{\varphi}$ (see Table 4.1), but the difference is not as great. In both cases, the parameters of the nonlocal term were adjusted to reproduce the rms charge radius of the smaller isotope (^{40}Ca and ^{124}Sn), but the dispersive correction for the protons in the tin isotopes is much stronger than in the calcium isotopes. This could explain why the difference in the rms radii between φ_{NL} and $\bar{\varphi}$ (see Table 4.1) is not as great for ^{49}Ca as it is for ^{133}Sn, even though the increase in neutron number in going from ^{124}Sn to ^{132}Sn is the same as going from ^{40}Ca to ^{48}Ca. This uncertainty suggests that in order to properly extrapolate using a truly nonlocal potential it is important to implement a version of the DOM that also takes into account the nonlocality of the imaginary potential.

4.4.2 Transfer Cross Sections

The cross sections are shown in Fig. 4.3-4.9, and for each of these figures the results from using the set of interaction potentials CH89+WS, DOM+WS, and DOM+LBar are displayed. The latter two sets produce angular distributions with almost identi-

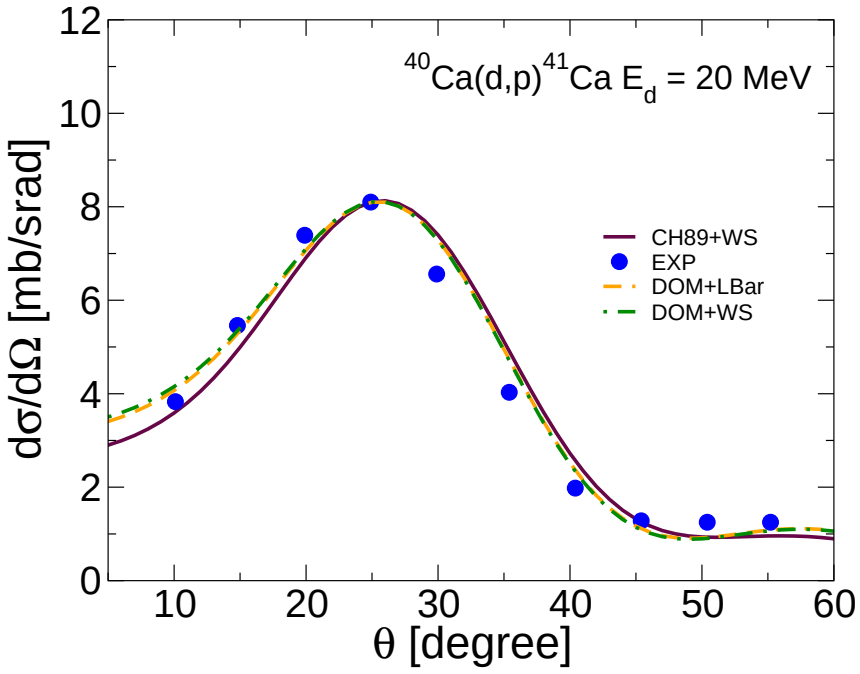

Figure 4.3: Angular distributions are shown for the reaction ^{40}Ca$(d,p)^{40}$Ca at $E_d = 20$ MeV. Theory predictions have been normalized to the data at the peak.

cal shapes. The angular distributions were also calculated with the interaction set DOM+NL, but their shapes were not significantly different from those calculated using DOM+WS and DOM+LBar and so are not shown. For reactions below the Coulomb barrier, the angular distributions were normalized at the backward angle peak of the data, while for reactions with beam energies above the Coulomb barrier, they were normalized at the forward angle peak. In the case of the ^{48}Ca(d,p)^{49}Ca reaction, for example, the relevant angles were $\theta \approx 155°$, $\theta \approx 10°$ and $\theta \approx 5°$ for $E_d = 2$, 19.3 and 56 MeV, respectively.

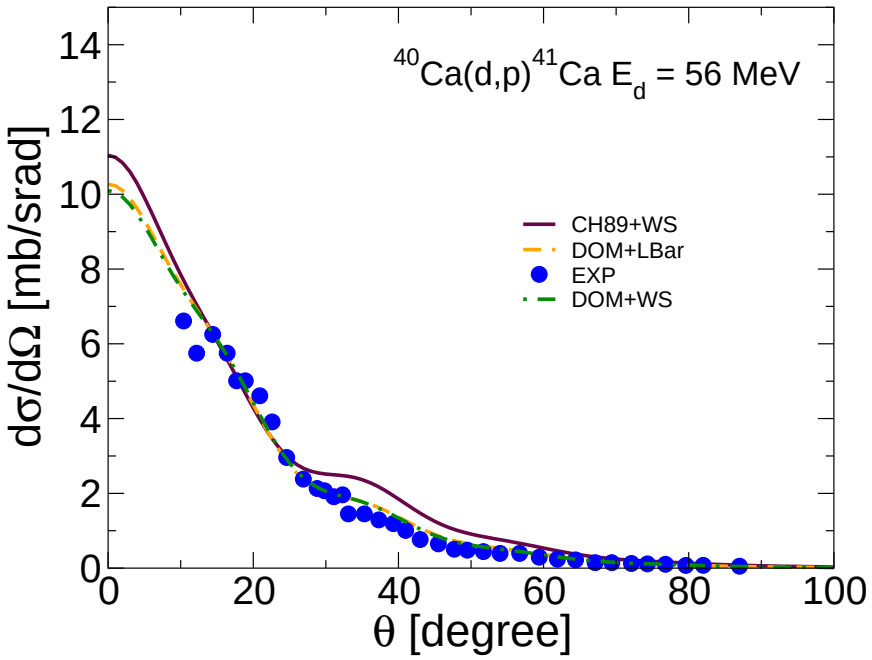

Figure 4.4: Angular distributions are shown for the reaction $^{40}\mathrm{Ca}(d,p)^{40}\mathrm{Ca}$ at $E_d = 56$ MeV. Theory predictions have been normalized to the data at the peak.

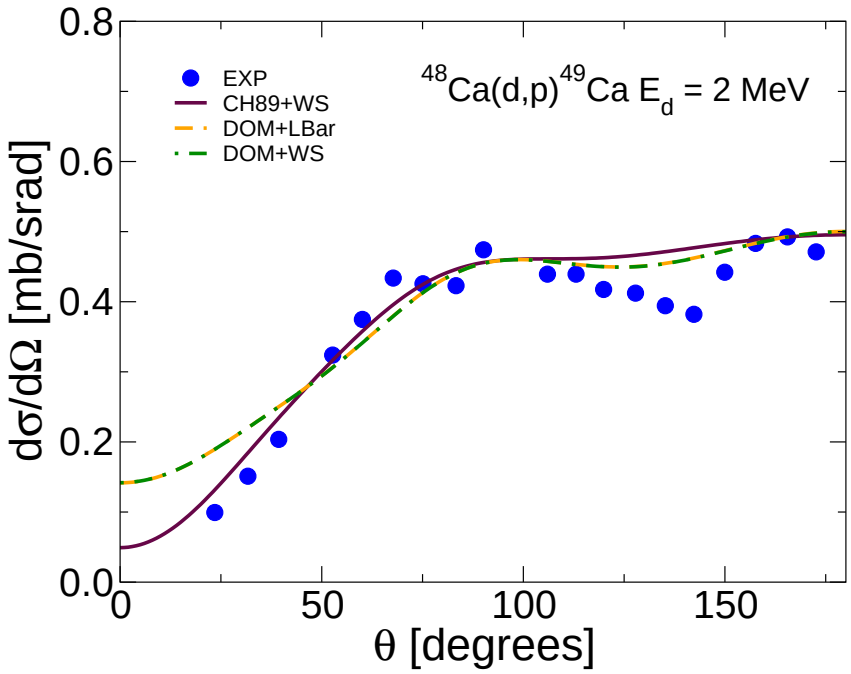

Figure 4.5: Angular distributions are shown for the reaction $^{48}\mathrm{Ca}(d,p)^{49}\mathrm{Ca}$ at $E_d = 2$ MeV. Theory predictions have been normalized to the data at backward angles.

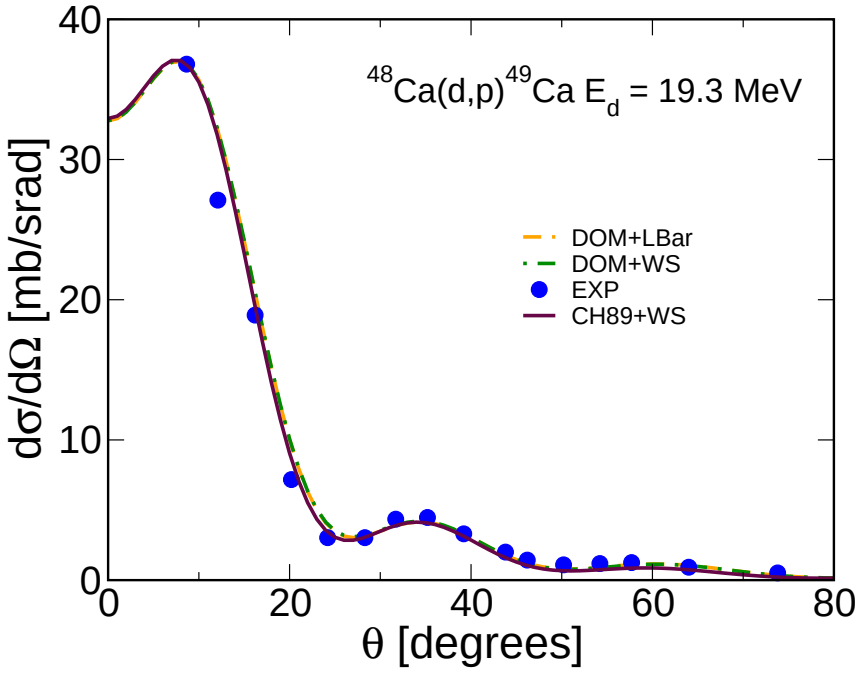

Figure 4.6: Angular distributions are displayed for the reaction $^{48}\mathrm{Ca}(d,p)^{49}\mathrm{Ca}$ at $E_d = 19.3$ MeV. Theory predictions have been normalized to the data at the peak.

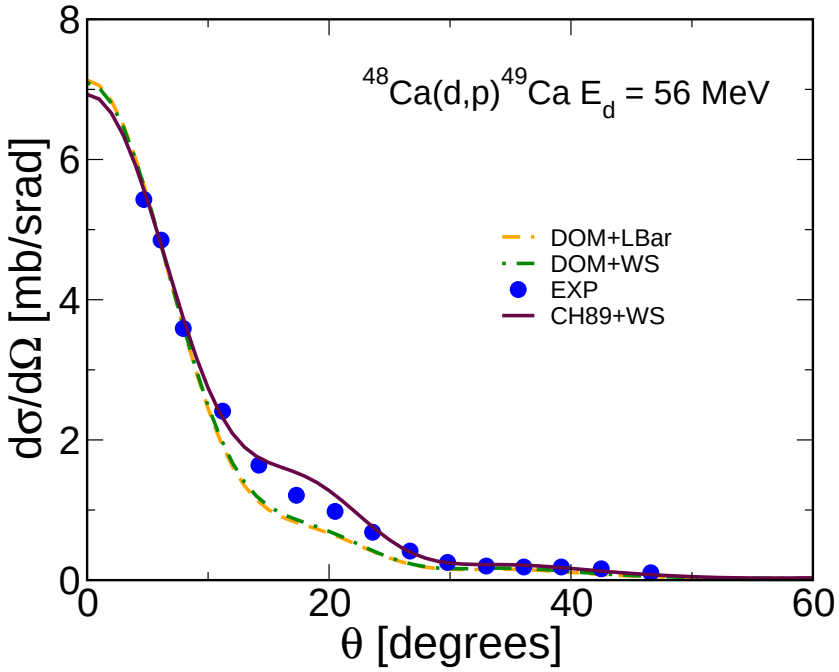

Figure 4.7: Angular distributions for the reaction $^{48}\mathrm{Ca}(d,p)^{49}\mathrm{Ca}$ at $E_d = 56$ MeV are displayed. Theory predictions have been normalized to the data at forward angles.

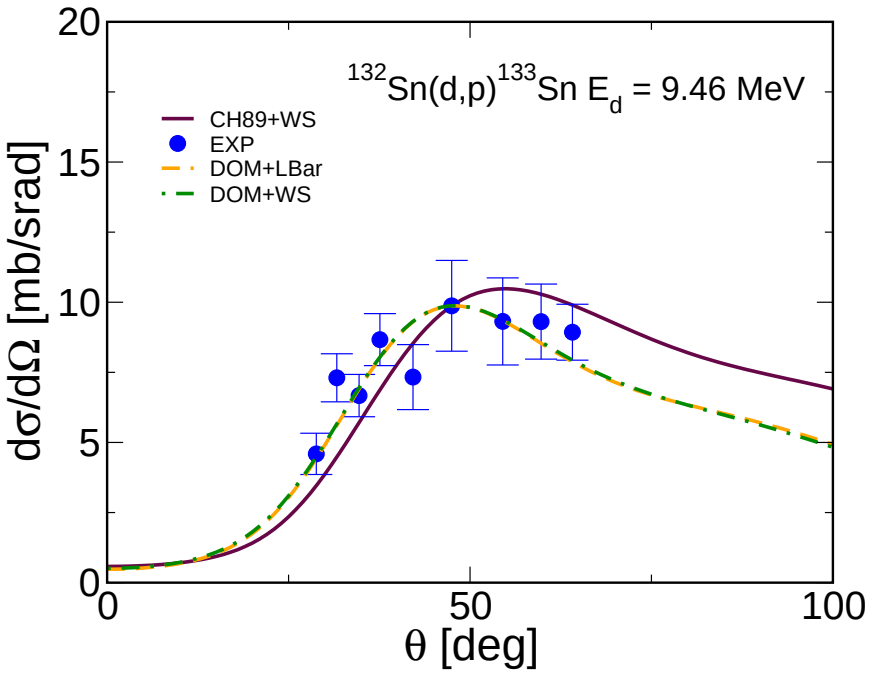

Figure 4.8: Angular distributions for the $^{132}\mathrm{Sn}(d,p)^{133}\mathrm{Sn}$ reaction at a deuteron energy of $E_d = 9.46$ MeV are shown normalized at the peak of the experimental cross section.

For the Ca isotopes, the DOM is able to describe the cross sections well, but there is no significant difference between the angular distributions predicted by the DOM and those predicted by CH89+WS. For ^{132}Sn, there is a larger difference between DOM and CH89 descriptions of the angular distributions, although both descriptions are consistent with the data. Since CH89+WS and DOM+WS use the same overlap function, it is clear that the difference in the angular distributions between CH89 and DOM is due to the optical potentials and not the choice of overlap function. The real part of the DOM potential, for example, has a larger radius, which shifts the diffraction pattern toward smaller angles. The CH89 and DOM optical potentials for ^{132}Sn are compared in Fig. 4.10.

In Fig. 4.10 (b), the DOM imaginary potential for neutrons is seen to be weaker than the corresponding CH89 potential, while the DOM imaginary potential for pro-

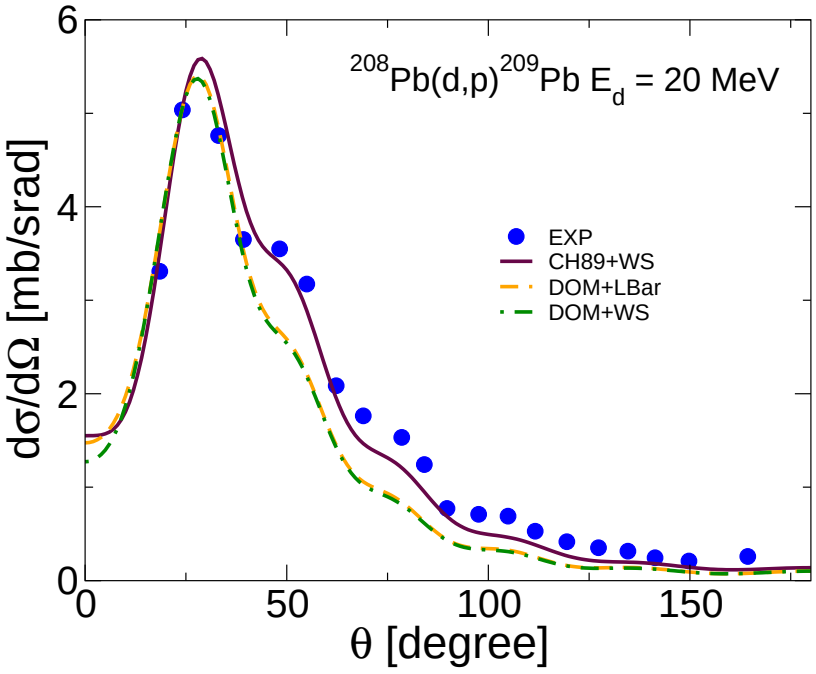

Figure 4.9: Angular distributions for the ^{208}Pb$(d,p)^{209}$Pb reaction are shown at a deuteron energy of $E_d = 20$ MeV and normalized at the peak of the experimental data.

tons is much stronger. In [24], the DOM potentials resulting from global fits to data exhibited a surface absorption with a very weak dependence on $(N-Z)/A$ for neutrons for both Sn and Ca isotopes, whereas the protons exhibited a strong dependence on $(N-Z)/A$. Thus, the surface absorption for neutrons in the DOM was assumed to have a much weaker asymmetry dependence than in Ref. [16].

The real parts of the CH89 potentials have the same radius parameter for both protons and neutrons by decree, whereas in the DOM, due to the different surface absorption, the dispersive correction makes the real proton potentials extend farther than those for neutrons. The CH89 potentials are not dispersive, so a more detailed comparison would be less productive.

For ^{208}Pb, the DOM actually makes the description of the data worse than that of CH89. No issues arose in the DOM fitting for this nucleus, and therefore the DOM fits

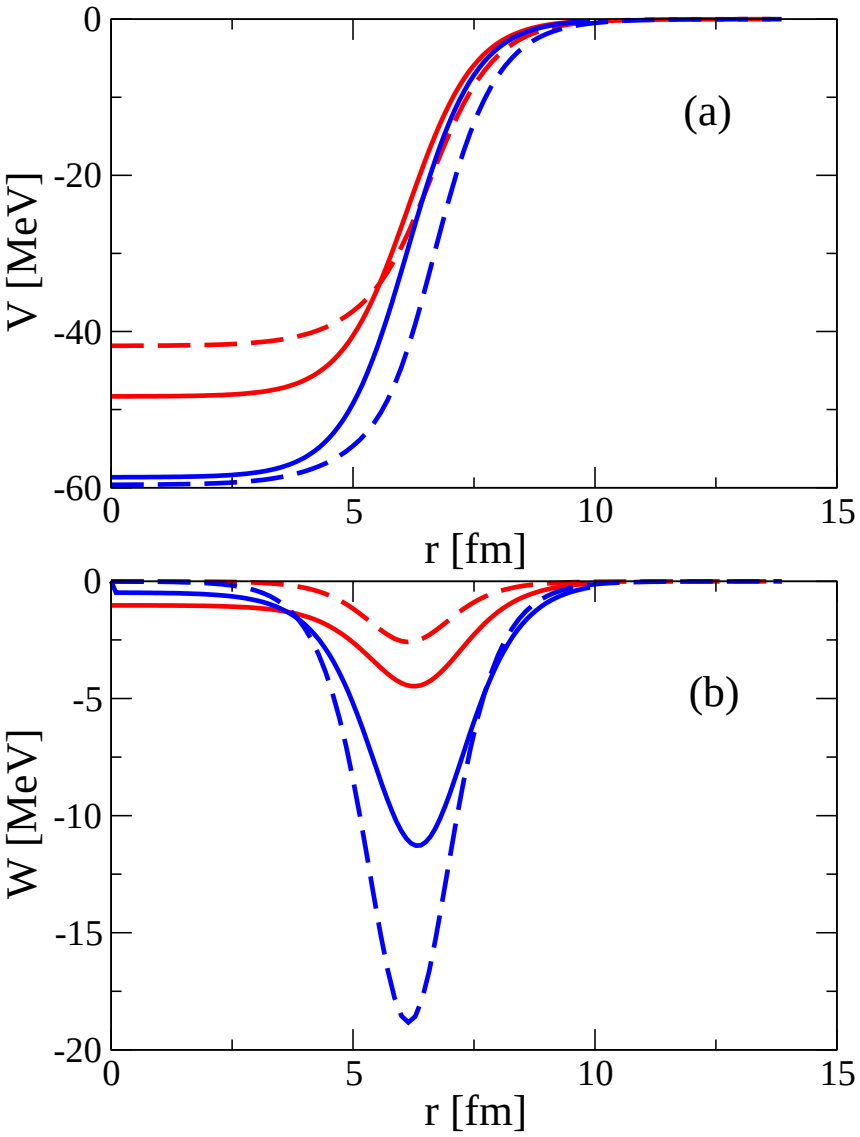

Figure 4.10: Comparison of the CH89 (solid) and the purely local DOM (dashed) optical potentials for n-^{132}Sn (red) and p-^{132}Sn (blue) at an energy of 4.7 MeV (half the deuteron energy). The real component is shown in panel (a) and the imaginary component in panel (b). Adapted from Ref. [31].

Table 4.2: Spectroscopic factors obtained from the FR-ADWA analysis. The deuteron kinetic energy E_d (lab. frame) is in MeV. Reference to the experimental data set used in the extraction is also given .

Nucleus	E_d	data	CH89+WS	DOM+WS	DOM+LBar	DOM+NL	DOM(calc)
^{41}Ca	20	[74]	0.96	0.85	0.86	0.85	0.75
	56	[75]	0.88	0.73	0.74	0.74	
^{49}Ca	2	[76]	0.94	0.72	0.66	0.66	0.80
	13	[77]	0.82	0.67	0.61	0.61	
	19.3	[77]	0.77	0.68	0.62	0.62	
	56	[78]	1.1	0.70	0.62	0.65	
^{133}Sn	9.46	[62]	1.1	1.0	0.72	1.1	0.80
^{209}Pb	8	[79]	1.7	1.5	1.2	1.2	0.76
	20	[80]	0.89	0.61	0.51	0.52	

can be considered reliable for the elastic and total cross-section data, so in Ref. [31] the possibility of target excitation was explored and was found to be important for ^{208}Pb, especially at the higher energy. This may also explain why the spectroscopic factors extracted for this nucleus, and shown in Table 4.2, are not consistent for the two energies studied and why the spectroscopic factor for the sub-coulomb experiment is actually greater than 1. Thus, the present results for ^{208}Pb call for an extension of the FR-ADWA to include target excitation and deuteron breakup in a consistent framework.

4.4.3 Spectroscopic Factors

While the angular distributions predicted using DOM do not differ considerably from those using CH89, the normalization of the cross sections do. The experimental spectroscopic factor was determined by taking the ratio of $d\sigma/d\Omega$(exp) over $d\sigma/d\Omega$(theory) for θ at the first peak of the distribution for all but sub-barrier energies. The results obtained in the various approaches are compared in Table 4.2. The spectroscopic factor coming directly from the DOM, using Eq. (2.50), is shown in the last column and denoted with DOM(calc).

In general, the traditional CH89+WS approach yields spectroscopic factors which are larger than those obtained with the DOM and depend on the beam energy. This unwanted energy dependence was already seen in the systematic study in [81]. A comparison between CH89+WS and DOM+WS shows that the smaller spectroscopic factors given by the DOM are due to the potential and not the overlap function. For ^{48}Ca, CH89+WS yields spectroscopic factors in the range 0.77-1.1, but this large energy dependence is significantly reduced when DOM optical potentials are used.

When nonlocality is taken into account using $\bar{\varphi}$ for the overlap function (the DOM+LBar results), the spectroscopic factor is further reduced, except for the case of ^{40}Ca, for which there is basically no change in the spectroscopic factors. This lack of reduction is due to the fact that the wavefunctions $\bar{\varphi}$ and φ_{WS} are almost identical. In all other cases, the different radius parameter obtained in DOM fits, together with the nonlocality correction, shift density from the interior and enhance the probability in the surface region. A larger overlap function at the surface produces larger cross-sections which then imply small spectroscopic factors. Spectroscopic factors extracted using DOM ingredients are much more in line with those from $(e, e'p)$ measurements [5] with the exception of ^{208}Pb.

The spectroscopic factors extracted using the purely local DOM but with the overlap function φ_{NL} (DOM+NL) are essentially the same as those obtained using DOM+LBar, except for the (d, p) reaction on ^{48}Ca with $E_d = 56$ MeV and for the case of ^{132}Sn. The former is not surprising since at higher energy the interior of the overlap function is probed, which is where φ_{NL} and $\bar{\varphi}$ differ the most (see Fig. 4.2). In the latter case, it is already seen in Table 4.1 that the rms radius of φ_{NL} is much smaller than $\bar{\varphi}$ resulting in a wavefunction that is less extended and hence a larger spectroscopic factor. A possible explanation for this discrepancy has already been given.

The two spectroscopic factors extracted from the ^{40}Ca reactions are not consistent with each other, as in the case of ^{48}Ca. However, one should keep in mind that describing low-energy scattering for ^{40}Ca is notoriously difficult to describe. In fact,

proton elastic scattering data for ^{40}Ca at energies below 18 MeV were excluded from the DOM fit. Since in the ADWA the optical potentials are evaluated at $E_d/2$, the DOM results for ^{40}Ca(d,p) at $E_d = 20$ MeV are not well constrained by elastic nucleon scattering data. Thus, the spectroscopic factor obtained for this energy is suspect.

The spectroscopic factors for ^{208}Pb, even with nonlocality taken into account, are also not consistent, but as already discussed, this may be due to not properly taking into account target excitation in the FR-ADWA. It was shown in Ref. [82] that target excitation in ^{40}Ca$(d,p)^{41}$Ca is important at low energies, and this effect may explain why the spectroscopic factors extracted from the ^{40}Ca reactions are less consistent with each other than the ones extracted from the ^{48}Ca reactions. The ^{48}Ca nucleus has a very weak transition to its first excited state, and therefore no significant effect of target excitation is expected. The effects of target excitation were tested for the reaction on ^{132}Sn and found to be negligible [31].

The spectroscopic factors predicted directly by DOM without reference to transfer reaction data (last column) are larger than those extracted from experiment, but as discussed in Ch. 3, this difference is mostly associated with the choice of where the imaginary part vanishes in the vicinity of the Fermi energy. In Ref. [23] the spectroscopic factors are smaller by about 0.1 as compared with those obtained in Ref. [24] and shown in Table 4.2.

4.5 Conclusions

In general, the DOM performs as well as the CH89 parameterization in the description of the angular distributions from (d,p) reactions. The spectroscopic factors extracted using the DOM, however, are more in line with those obtained from $(e,e'p)$ measurements. In addition, at least in the case of ^{48}Ca, the DOM provides consistency in the spectroscopic factors extracted at different beam energies, whereas in the standard approach the spectroscopic factors are strongly energy dependent.

In contrast to the CH89 parametrization, the DOM generates overlap functions

in addition to the nucleon-target interactions. The DOM incorporates reaction and structure data on the same footing. Therefore the DOM provides a more holistic and systematic way to extrapolate potentials to rare isotopes and provides an excellent platform to analyze transfer reactions involving such nuclei.

Chapter 5

FRPA and DOM

As already mentioned in the introduction, the optical potential is formally identical to the irreducible nucleon self-energy. However, most formalisms for the optical potential do not properly take into account hole propagation. In Feshbach's theory, for example, the hole states are projected out of the Hilbert space; but it was shown in Refs. [26, 83, 84] that if the Hilbert space is extended to include states both above and below the Fermi surface, then the optical potential from Feshbach's theory corresponds exactly to the irreducible nucleon self-energy $\Sigma^*(E)$. This equivalence means that calculations based on the Green's function theory can be employed to suggest improvements of optical models. Since the DOM optical potentials can be thought of as a representation of the irreducible nucleon self-energy, a comparison between the microscopic self-energy from Green's function theory and the empirical self-energy from a DOM fit is particularly interesting.

The most sophisticated microscopic implementation of the Green's function is the Fadeev random phase approximation (FRPA) [45, 46, 85], which takes into account long-range or low-energy correlations in which nucleons couple to low-lying collective states and giant resonances. The random phase approximation (RPA) is used to generate particle-hole (ph), particle-particle (pp), and hole-hole (hh) excitations or phonons. The ph phonons are then coupled to the pp or hh phonons in a way that properly takes into account Pauli correlations, and the resulting 2p1h and 2h1p self-

energy diagrams are summed to all orders.

The purpose of this chapter is to seek a microscopic underpinning of the qualitative features of empirical optical potentials. Since Ca isotopes have been studied in recent DOM fits [23–25, 30], the comparison between DOM and FRPA results has been done for ^{40}Ca and ^{48}Ca with emphasis on the role of LRC. The FRPA self-energy is also calculated for ^{60}Ca.

The work presented in this chapter is a result of a collaboration with C. Barbieri, who provided the FRPA self-energies. Much of the material discussed below can be found in Ref [32].

5.1 Ingredients of the FRPA

The self-energy is shown in terms of Feynman diagrams in Fig. 5.1. Σ^{∞} is the correlated HF term, which is energy-independent. The other terms take into account the coupling of sp motion to 2p1h/2h1p states and are energy-dependent. The polarization propagators $R^{(2p1h)}(E)$ and $R^{(2h1p)}(E)$ account for the fact that the different hole lines and particle lines can all interact with each other, affecting each other's motion. This treatment of pp, hh, and ph excitations on an equal footing is one of the principal improvements in the FRPA over other approximation schemes.

The basic ingredients for the calculation of the self-energy are the particle-hole (ph) polarization propagator, $\Pi_{\alpha\beta,\gamma\delta}(E)$, that describes excited states of the A-nucleon

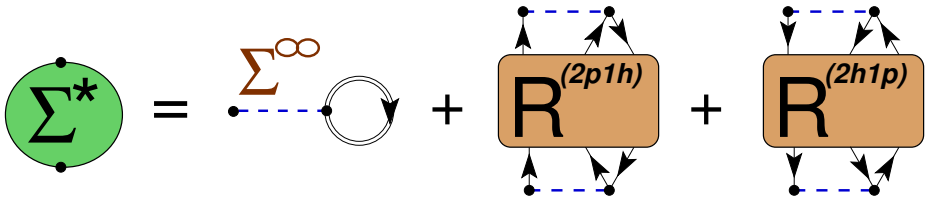

Figure 5.1: The self-energy $\Sigma^{\star}(E)$ separates exactly into a static (mean-field) term, Σ^{∞}, and the polarization propagators $R^{(2p1h/2h1p)}(E)$ for the 2p1h/2h1p motion. These $R(E)$ are expanded in terms of particle-vibration couplings as depicted below in Fig. 5.3. Published in Ref. [32].

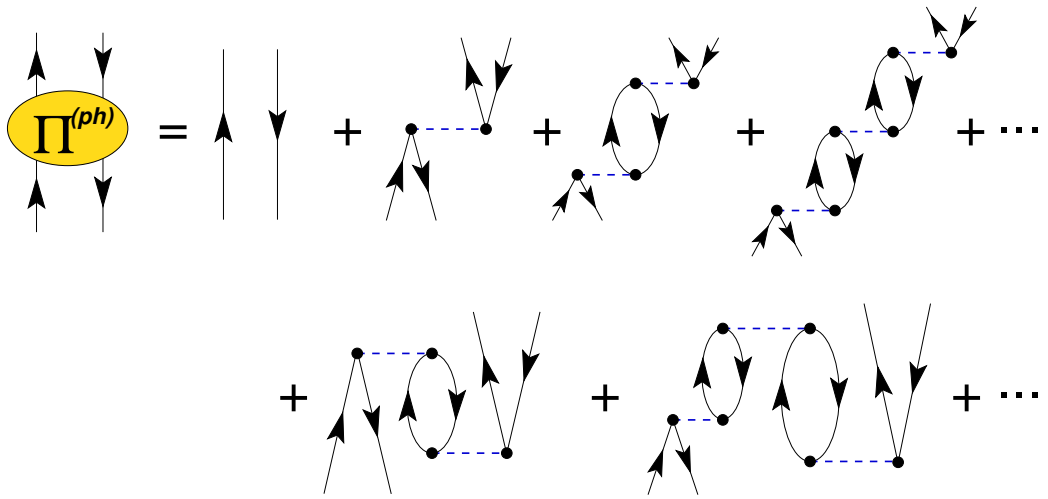

Figure 5.2: Expansion of the ph propagator $\Pi(E)$ in a series of ring diagrams. The second line gives examples of time-inversion patterns that are generated by the RPA. A similar expansion, in terms of ladders diagrams, applies to $g^{II}(E)$. The diagrams are time ordered, with time propagating upward. Published in Ref. [32].

system, and the two-particle propagator, $g^{II}_{\alpha\beta,\gamma\delta}(E)$, that describes the propagation of two added/removed particles. These propagators are calculated as summations of ring and ladder diagrams in the random-phase approximation (RPA). This allows for a proper description of collective excitations in the giant-resonance region when the model space is sufficiently large. The RPA induces time orderings as those shown in Fig. 5.2 for the ph case and accounts for the presence of two-particle–two-hole and more complicated admixtures in the ground state, which are generated by correlations.

Once $\Pi(E)$ and $g^{II}(E)$ are calculated, they are re-coupled to single-particle or single-hole states to obtain the $R^{(2p1h)}(E)$ and $R^{(2h1p)}(E)$ propagators that appear in Fig. 5.1. This is done by solving the set of Faddeev equations detailed in Refs. [45, 85]. Some examples of the resulting diagrams are shown in Fig. 5.3.

A further advantage of the FRPA formalism is that it calculates explicitly the effects of *all* many-body excitations including the region of giant resonances. The result is a global description of the self-energy over a wide range of energies, wider than is currently possible with shell-model calculations [86]. The FRPA is then a good method for investigating medium-mass nuclei in a wide energy domain around

the Fermi surface.

The coupling scheme outlined above does not adequately incorporate short-range correlations, but they can be partially accounted for by directly calculating the two-body scattering for nucleons that propagate outside the model space. The result is the so-called $\mathcal{G}$-matrix that must be employed as an energy-dependent effective interaction inside the chosen space. The contribution from ladder diagrams from outside the model space is then added to the calculated self-energy from Fig. 5.1 and results in an energy-dependent correction to Σ^{∞} [86]. This additional energy dependence enhances the reduction of the spectroscopic strength of occupied orbits by about 10%. A similar depletion is also obtained in nuclear-matter calculations with realistic interactions [8] and indirectly confirmed by high-energy electron scattering data [52, 87] that identify a corresponding presence of high momenta in the nucleus.

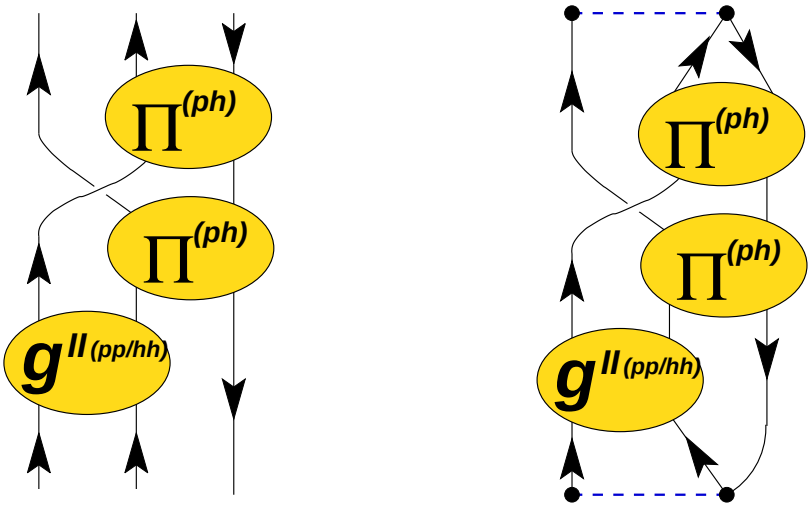

Figure 5.3: *Left:* Example of one of the diagrams for $R^{(2p1h)}(E)$ that are summed to all orders by means of the Faddeev method. Each of the ellipses represent an infinite sum of rings [$\Pi(E)$] or ladders [$g^{II}(E)$]. The diagrams included in $\Pi(E)$ are shown in Fig. 5.2 and $g^{II}(E)$ contains the ladder diagrams [85]. *Right:* The corresponding contribution to the self-energy obtained from $R^{(2p1h)}(E)$ (compare to Fig. 5.1). Published in Ref. [32].

5.2 Connecting the DOM and FRPA Self-energies

For a $J = 0$ target nucleus, all partial waves (ℓ, j, τ) are decoupled, where ℓ,j label the orbital and total angular momentum and τ labels the isospin. The irreducible self-energy in coordinate space (for either a proton or a neutron) can be written in terms of the harmonic-oscillator basis used in the FRPA calculation, as follows:

$$\Sigma^{\star}(\boldsymbol{x}, \boldsymbol{x'}; E) = \sum_{\ell j m_j \tau} \mathcal{I}_{\ell j m_j}(\Omega, \sigma) \left[\sum_{n_a, n_b} R_{n_a \ell}(r) \Sigma^{\star}_{ab}(E) R_{n_b \ell}(r') \right] (\mathcal{I}_{\ell j m_j}(\Omega', \sigma'))^*, \quad (5.1)$$

where $\boldsymbol{x} \equiv \boldsymbol{r}, \sigma, \tau$. The spin variable is represented by σ, n is the principal quantum number of the harmonic oscillator, and $a \equiv (n_a, \ell, j, \tau)$ (note that for a $J = 0$ nucleus the self-energy is independent of m_j). The standard harmonic-oscillator function is denoted by $R_{n\ell}(r)$, while $\mathcal{I}_{\ell j m_j}(\Omega, \sigma)$ represent the j-coupled angular-spin function.

The harmonic oscillator projection of the self-energy is calculated directly in the FRPA calculations and can be written as

$$\Sigma^{\star}_{ab}(E) = \Sigma^{\infty}_{ab}(E) + \tilde{\Sigma}_{ab}(E) = \Sigma^{\infty}_{ab}(E) + \sum_r \frac{m^r_a (m^r_b)^*}{E - \varepsilon_r \pm i\eta}. \quad (5.2)$$

The term with the tilde is the dynamic part of the self-energy due to long-range correlations calculated in FRPA, and $\Sigma^{\infty}_{ab}(E)$ is the correlated Hartree-Fock term which acquires an energy dependence through the energy dependence of the G-matrix effective interaction (see above). $\Sigma^{\infty}_{ab}(E)$ is the sum of the strict correlated Hartree-Fock diagram (which is energy independent) and the dynamical contributions due to short-range interactions outside the chosen model space. The self-energy was further decomposed in a central (0) part and a spin-orbit (ls) part according to

$$\Sigma^{\ell j>} = \Sigma^{\ell}_0 + \frac{\ell}{2} \Sigma^{\ell}_{\ell s}, \quad (5.3a)$$

$$\Sigma^{\ell j<} = \Sigma^{\ell}_0 - \frac{\ell + 1}{2} \Sigma^{\ell}_{\ell s}, \quad (5.3b)$$

with $j_{>,<} \equiv \ell \pm \frac{1}{2}$. The corresponding static terms are denoted by $\Sigma_0^{\infty,\ell}$ and $\Sigma_{\ell s}^{\infty,\ell}$, and the corresponding dynamic terms are denoted by $\tilde{\Sigma}_0^{\ell}$ and $\tilde{\Sigma}_{\ell s}^{\ell}$.

The FRPA calculation employs a discrete sp basis in a large model space which results in a large number of poles in the self-energy (5.2). Since the goal is to compare with optical potentials at positive energy, it is appropriate to smooth out these contributions by employing a finite width for these poles. The optical potential was always intended to represent an average smooth behavior of the nucleon self-energy [22]. In addition, it makes physical sense to at least partly represent the escape width of the continuum states by this procedure. Finally, further spreading of the intermediate states to more complicated states ($3p2h$ and higher excitations that were not included in the FRPA calculation) can also be accounted for by this procedure. Thus, before comparing to the DOM potentials, the dynamic part of the microscopic self-energy was smoothed out using a finite, energy-dependent width for the poles

$$\tilde{\Sigma}^{\ell j}_{n_a,n_b}(E) = \sum_r \frac{m^r_{n_a} m^r_{n_b}}{E - \varepsilon_r \pm i\eta} \longrightarrow \sum_r \frac{m^r_{n_a} m^r_{n_b}}{E - \varepsilon_r \pm i\Gamma(E)} \,. \tag{5.4}$$

The real and imaginary parts are then

$$\begin{aligned} \tilde{\Sigma}^{\ell j}_{n_a,n_b}(E) &= \sum_r \frac{(E-\varepsilon_r)}{(E-\varepsilon_r)^2 + [\Gamma(\varepsilon_r)]^2} m^r_{n_a} m^r_{n_b} \\ &+ i\left[\theta(\varepsilon_F - E) \sum_h \frac{\Gamma(\varepsilon_h)}{(E-\varepsilon_h)^2 + \Gamma(\varepsilon_h)^2} m^h_{n_a} m^h_{n_b}\right. \\ &- \left.\theta(E - \varepsilon_F) \sum_p \frac{\Gamma(\varepsilon_p)}{(E-\varepsilon_p)^2 + [\Gamma(\varepsilon_p)]^2} m^p_{n_a} m^p_{n_b}\right], \end{aligned} \tag{5.5}$$

where, r implies a sum over both particle and hole states, h denotes a sum over the hole states only, and p a sum over the particle states only. For the width, the following form was used [88]:

$$\Gamma(E) = \frac{1}{\pi} \frac{a\,(E-\varepsilon_F)^2}{(E-\varepsilon_F)^2 + b^2},$$

with a=12 MeV and b=22.36 MeV. This generates a narrow width near ε_F that

increases as the energy moves away from the Fermi surface, in accordance with observations.

In the DOM representation of the optical potential the self-energy is recast in the form of a subtracted dispersion relation as

$$\Sigma^{\star}_{ab}(E) = \Sigma^{S}_{ab} + \tilde{\Sigma}^{S}_{ab}(E), \tag{5.6}$$

where

$$\Sigma^{S}_{ab} = \Sigma^{\star}_{ab}(\varepsilon_F)\,, \tag{5.7}$$

$$\tilde{\Sigma}^{S}_{ab}(E) = \Sigma^{\star}_{ab}(E) - \Sigma^{\star}_{ab}(\varepsilon_F)\,. \tag{5.8}$$

Since there is no imaginary part at ε_F, Σ^{S}_{ab} is real, and Im $\tilde{\Sigma}^{S}_{ab}(E)$ is the same as the imaginary part defined in Eq. (5.2). Σ^{S}_{ab} is the entity that is parametrized as the HF potential in the DOM, and Re $\tilde{\Sigma}^{S}_{ab}(E)$ is the dispersive correction used in the DOM. In the following sections, either the normal or the subtracted form of the real parts will be shown as appropriate.

Volume Integrals

The focus of this work is primarily on averaged properties of the self-energy, as described by volume integrals. In fitting optical potentials, it is usually found that volume integrals are well constrained by the experimental data [22, 89]. For this reason, they have been considered as a reliable measure of the total strength of a potential. For a nonlocal and ℓ-dependent potential of the form (5.1) it is convenient to consider separate integrals for each angular momentum component, $\Sigma^{\ell}_{0}(r,r')$ and $\Sigma^{\ell}_{\ell s}(r,r')$, which correspond to the square brackets in Eq. (5.1) and decomposed according to (5.3). Denoting the central real part of the optical potential by V and the central imaginary part by W, the corresponding volume integrals of these potentials

are

$$J_W^\ell(E) = 4\pi \int dr r^2 \int dr' r'^2 \text{Im } \Sigma_0^\ell(r, r'; E) \tag{5.9a}$$

$$J_V^\ell(E) = 4\pi \int dr r^2 \int dr' r'^2 \text{Re } \Sigma_0^\ell(r, r'; E) \tag{5.9b}$$

and the corresponding averaged quantities

$$J_W^{avg} = \frac{1}{N_{\{\ell\}}} \sum_{\ell \in \{\ell\}} J_W^\ell \tag{5.10a}$$

$$J_V^{avg} = \frac{1}{N_{\{\ell\}}} \sum_{\ell \in \{\ell\}} J_V^\ell \,. \tag{5.10b}$$

In Eqs. (5.10), $N_{\{\ell\}}$ is the number of partial waves included in the average and the sum runs over all values of ℓ except if otherwise indicated.

The correspondence between the above definitions and the volume integrals used for the (local) DOM potential in Refs. [23, 25] can be seen by casting a spherical local potential $U(r)$ into a nonlocal form $U(\boldsymbol{r}, \boldsymbol{r}') = U(r)\delta(\boldsymbol{r} - \boldsymbol{r}')$. Expanding this in spherical harmonics gives

$$U(\boldsymbol{r}, \boldsymbol{r}') = \sum_{lm} U^\ell(r, r') Y^*_{\ell m}(\Omega') Y_{\ell m}(\Omega) \,, \tag{5.11}$$

with the ℓ component

$$U^\ell(r, r') = \frac{U(r)}{r^2} \delta(r - r') \,, \tag{5.12}$$

which is angular momentum independent. The definitions (5.9) for the volume integrals lead to

$$\begin{aligned} J_U^\ell &= 4\pi \int dr r^2 \int dr' r'^2 U^\ell(r, r') \\ &= 4\pi \int U(r) r^2 dr = \int U(r) d\boldsymbol{r} \,, \qquad \text{for any } \ell \end{aligned} \tag{5.13}$$

and reduces to the usual definition of volume integral for local potentials. Thus,

Eqs. (5.9) and (5.10) can be compared directly to the integral determined in previous studies of the DOM.

Some other useful volume integrals are those for the central part of the subtracted dispersive correction (denoted by a D) and $\Sigma^{\infty}(\varepsilon_F)$ (denoted by F). These are

$$J_D^{\ell}(E) = 4\pi \int dr r^2 \int dr' r'^2 \mathrm{Re}\ \tilde{\Sigma}_0^{S,\ell}(r, r'; E) \tag{5.14}$$

$$J_F^{\ell} = 4\pi \int dr r^2 \int dr' r'^2 \Sigma_0^{\infty,\ell}(r, r'; \varepsilon_F). \tag{5.15}$$

Eq. (5.14) will be used to compare the FRPA and DOM dispersive corrections.

5.3 Calculation Details

Calculations were done for two different realistic interactions, the Argonne AV18 potential [90] and N3LO [91]. The former is local and contains a strongly-repulsive core, while the latter is nonlocal and softer. Calculations based on the N3LO interaction gave only slightly less absorption for $E > \varepsilon_F$, especially in ^{40}Ca. Nevertheless, the results for the two interactions are qualitatively similar, so all the results (except for those in Fig. 5.4) shown in this chapater are limited to the AV18 case.

Extremely large model spaces are not required for the present analysis because the short-range part of the interaction is already accounted for through the partitioning procedure described in Sec. 5.1 [86]. In the current energy regime of interest, short-range physics affects mainly the real part of the self-energy. The contributions to the imaginary part are not included as they show up at very high positive energies which are not considered here [8]. The self-energies of ^{40}Ca, ^{48}Ca and ^{60}Ca were calculated using the FRPA in a harmonic-oscillator model space with frequency $\hbar\Omega = 10$ MeV. Calculations for ^{60}Ca were possible in no-core model spaces including up to 8 major shells (N_{max} =7), so this truncation was employed for all the results presented in Sec. 5.4. This space is deemed large enough to provide a proper description of the physics around the Fermi surface and at least qualitatively good at energies in the

region of giant-resonance excitations, which is of interest in this study.

Due to the unavoidable truncation of the model space, calculations are only reliable within in an energy interval centered around ε_F. These limits were checked by calculating J_W of ^{48}Ca for model spaces of different sizes, including up to 10 major oscillator shells (which is possible for this isotope [9]), and the results are illustrated in Fig. 5.4. The volume integrals for two successive model-spaces are similar over a certain energy range, which increases as N_{max} is increased, as expected. Based on this comparison, the self-energies calculated for N_{max}=7 (8 shells) are expected to be meaningful for energies in the range -80 MeV$< E - \varepsilon_F <$80 MeV.

5.4 Results

5.4.1 Angular-Momentum Dependence

Optical potentials that are purely local have no angular-momentum dependence, aside from the spin-orbit term. Microscopically calculated self-energies, however, are intrinsically angular-momentum dependent. Figure 5.5 illustrates this angular-momentum dependence for the real parts of the self-energy at $E = \varepsilon_F$.

A nonlocal potential of the form given by Eq. (3.1) is automatically dependent on ℓ due to the dependence on the angle between $\boldsymbol{r}$ and $\boldsymbol{r}'$. As already discussed in Ch. 3, employing such a potential in the DOM for the HF-type term (in place of the energy-dependent, local-equivalent term) improves the description of bound-state information, such as the hole spectral functions and observables like the charge density. The volume integral of this nonlocal term, denoted by $J_{HF}^{DOM,\ell}$, is also shown in Fig. 5.5 and exhibits a systematic decrease in strength with increasing ℓ.

Since the DOM potentials are parametrized using a subtracted dispersion relation, $J_{HF}^{DOM,\ell}$ can be directly compared to $J_V^\ell(\varepsilon_F)$. For $\ell = 0 - 3$, $J_{HF}^{DOM,\ell}$ roughly follows $J_V^\ell(\varepsilon_F)$, which suggests that the ℓ-dependence of the self-energy at ε_F is due in large

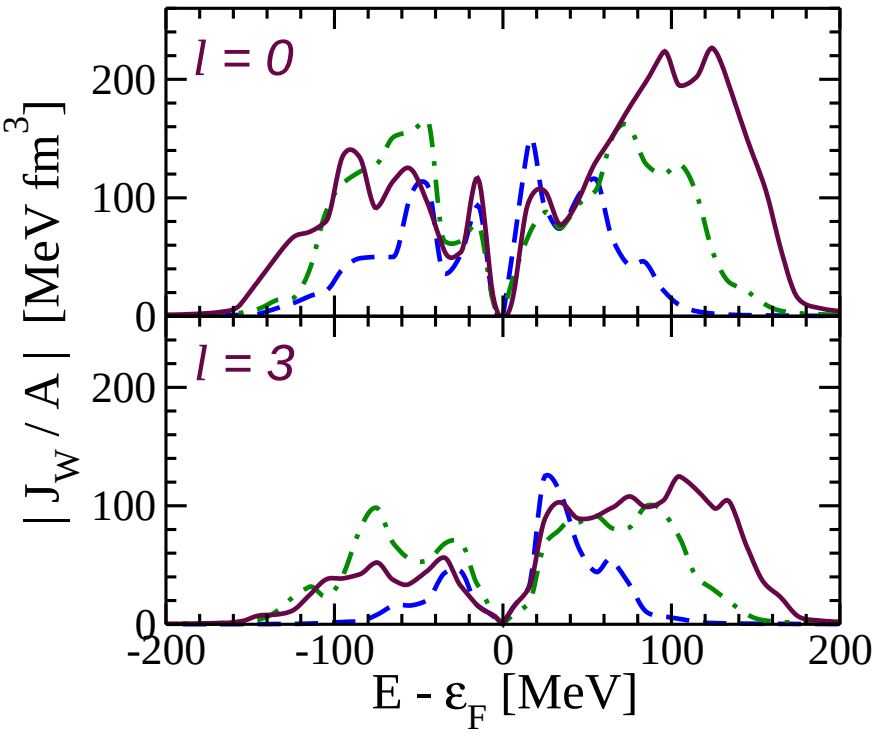

Figure 5.4: Imaginary volume integral $J_W^\ell(E)$ of the ^{48}Ca self-energy calculated with model spaces of different sizes. The top (bottom) panels refer to the scattering of a neutron with angular momentum ℓ=1 (ℓ=3). Dashed, dot-dashed and full lines refer to model spaces of 6, 8, and 10 oscillator shells, respectively. These results are for the N3LO interaction.

part to nonlocality. There is a parity dependence in $J_V^\ell(\varepsilon_F)$ that is not present in the DOM result, but this topic will be discussed in the next section. The volume integral J_F^ℓ, from Eq. (5.15), is also shown in Fig. 5.5 (diamonds). It lies somewhat above $J_V^\ell(\varepsilon_F)$, which suggests that Σ^S from Eq. (5.7) provides more binding than Σ_0^∞.

The overall strength of the imaginary part of the self-energy also decreases with increasing ℓ. This effect may be partly explained by the truncated model space, since

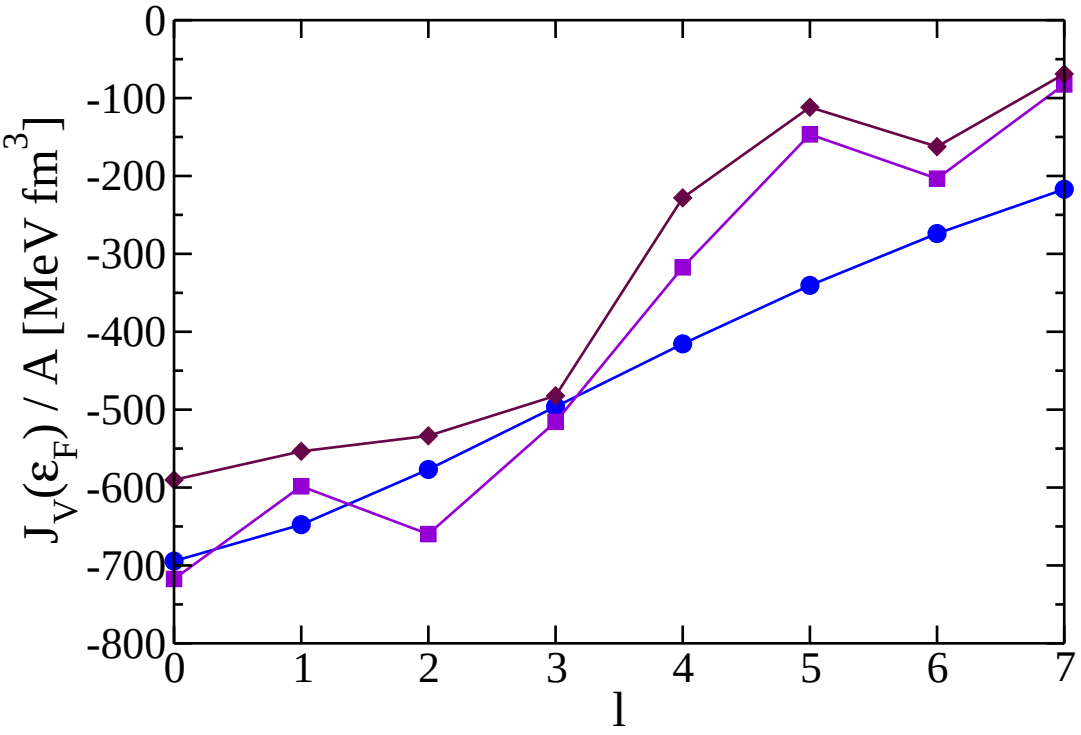

Figure 5.5: Angular momentum dependence for the volume integrals $J_V^\ell(\varepsilon_F)$ (solid squares), J_F^ℓ (diamonds) and $J_{HF}^{DOM,\ell}$ (circles), which should be compared with $J_V^\ell(\varepsilon_F)$. The results shown are for neutrons in ^{40}Ca.

the higher ℓ-channels also have fewer orbits. Figure 5.6 shows the volume integrals J_W averaged over ℓ-channels with the same number of harmonic-oscillator orbits inside the chosen model space for neutrons in ^{40}Ca. On the other hand, Fig. 5.5 suggests that most of the decrease in J_W comes from the ℓ-dependence implied by the nonlocality of the imaginary potential.

The green dash-double-dotted curve in Fig. 5.6 illustrates the corresponding DOM volume integral, J_W^{DOM}, which does not depend on ℓ. Since the DOM imaginary potential was assumed to be local, J_W^{DOM} has been corrected by the effective mass that governs nonlocality [22, 30] in order to be compared with the FRPA results, which are generated from nonlocal potentials. The overall effect of this correction is

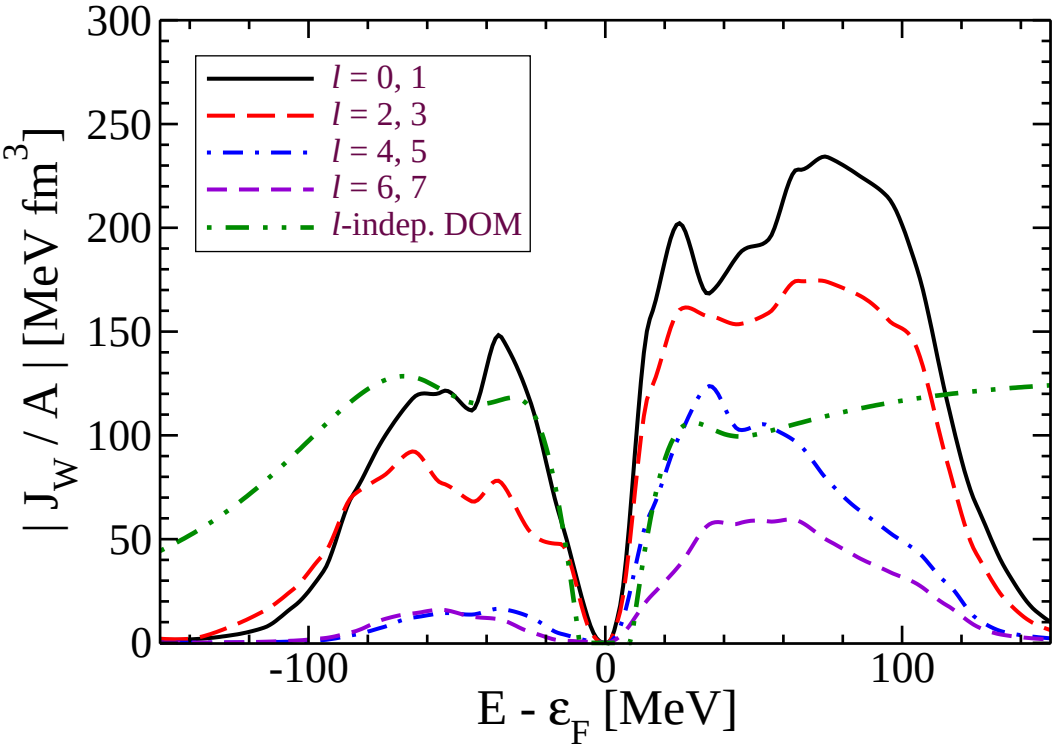

Figure 5.6: Separate partial wave contributions of J_W averaged over ℓ-channels with 4 (solid), 3 (long-dashed), 2 (dot-dashed), and 1 (short-dashed) harmonic-oscillator orbits in the model space. This plot is for neutrons in ^{40}Ca. The dash-double-dotted curve represents the DOM result. Published in Ref. [32].

to enhance the absorption.

It was noted in Ch. 3 that assuming the imaginary potential to have the same strength for each ℓ results in occupations of higher ℓ-values below the Fermi energy that are too large. In contrast, according to Fig. 5.6, the imaginary part of the FRPA self-energy becomes less important for higher ℓ-values, especially below the Fermi energy. Below the Fermi energy, the volume integrals associated with the prevalence of low-ℓ orbits like s, p, and d dominate.

Clearly, the DOM overestimates the absorption of higher partial waves, and this problem could be solved in part by using a nonlocal imaginary potential in future

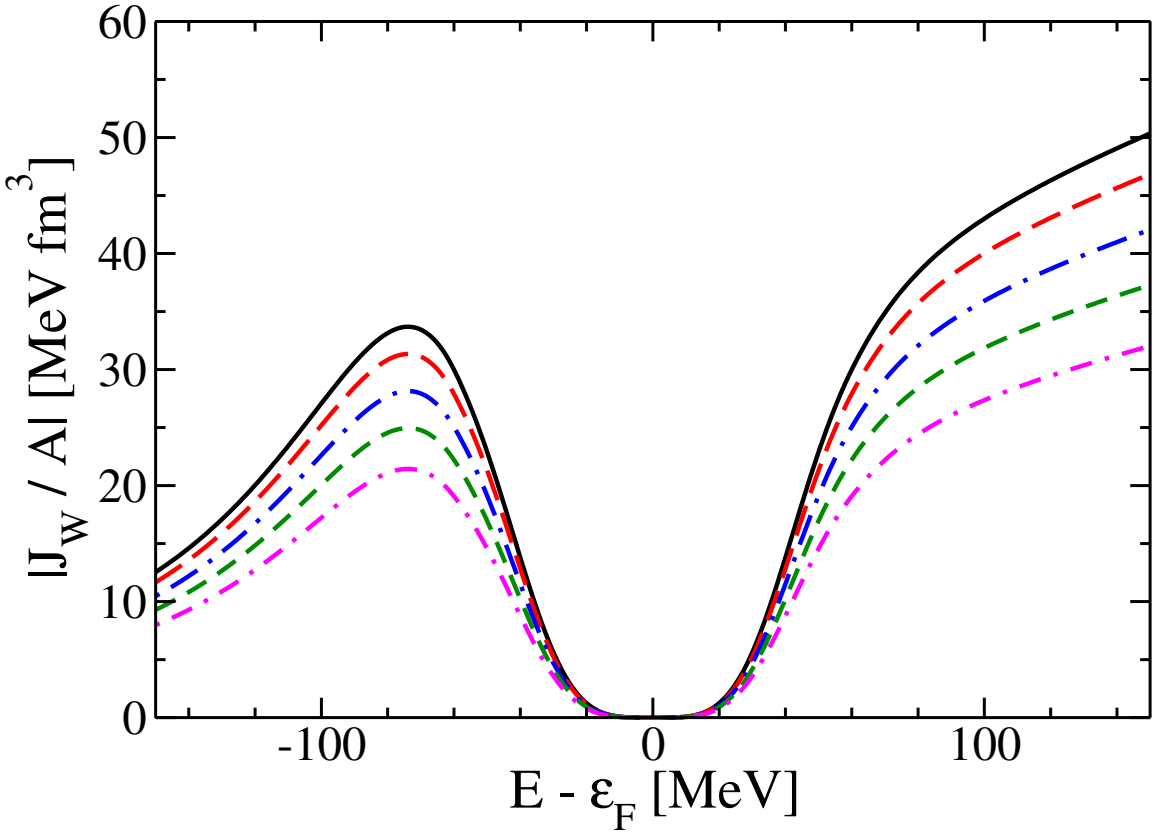

Figure 5.7: Imaginary volume integrals of the volume part of a DOM self-energy with a local Woods-Saxon form factor replaced by a nonlocal form proposed by Perey and Buck. The results shown are for $\ell = 0$ (solid), $\ell = 1$ (long-dash), $\ell = 2$ (long-dot-dash), $\ell = 3$ (short-dash) and $\ell = 4$ (short-dot-dash). Published in Ref. [32].

DOM implementations. For example, the local Woods-Saxon radial form factor used for the volume contribution to the imaginary potential could be replaced with the same kind of nonlocal potential employed in Ch. 3, while keeping the functional form of the energy dependent part the same.

The volume integral of such a potential is illustrated in Fig. 5.7 for different ℓ-values, where the energy dependence was taken from Ref. [23], and the parameters defining the nonlocal form factor were taken from Ref. [30] (they are also listed in Ch. 3). As in the case of the FRPA, the volume integrals decrease with increasing ℓ, although the decrease is not as great. A potential with a higher degree of nonlocality would result in a faster suppression of the terms with higher ℓ-values.

Since the imaginary part of the DOM has been assumed independent of ℓ (aside from the spin-orbit term), plotting J_W^{DOM} with the ℓ-averaged FRPA volume integral provides a more direct comparison. Such a comparison is made in Fig. 5.8 for protons in ^{40}Ca and ^{48}Ca. One can see that the FRPA predicts the absorption below ε_F to be significantly less than the absorption above, whereas in the DOM, the surface absorption is *assumed* to be symmetric about ε_F in an energy region of about 50 MeV above and below ε_F [22–25]. Thus, this assumption needs to be tested. In Fig. 5.8 the surface absorption of J_W^{DOM} is not quite symmetric about ε_F because the effective mass correction above ε_F is different from the correction below ε_F.

Above ε_F, the ℓ-averaged FRPA result is reasonably close to the DOM fit for both nuclei in the domain $E - \varepsilon_F < 80$ MeV, which is where the FRPA is expected to be relevant. The J_W calculated with the FRPA decreases quickly at energies $E - \varepsilon_F >$100 MeV due to the truncation of the model space. The DOM, on the other hand, predicts correctly that absorption remains sizable even at higher energies. Since the absorption above the Fermi energy is strongly constrained by elastic scattering data, Fig. 5.8 suggests that the FRPA does a good job of describing the physics relevant for a wide range of energies.

The importance of nonlocality for the imaginary part of the self-energy suggested by the FRPA calculations may actually provide a handle on describing the nuclear charge density for ^{40}Ca more accurately than was possible in Ref. [30]. Although the averaged volume integrals in Fig. 5.8 are similar to the DOM results for positive energies ($<$ 80 MeV), Fig. 5.6 demonstrates that the $\ell = 0$ contribution is actually significantly higher than the DOM volume integral. Since the imaginary part at positive energies is responsible for removing sp strength from the Fermi sea, a stronger absorption in the $\ell = 0$ channel would remove more strength from the origin.

Some of the overall features of the dispersive part of the self-energy are illustrated in Fig. 5.9, which shows the volume integral of the real part, J_V^ℓ. These results are shown for neutrons in ^{40}Ca and are separated in partial waves up to ℓ=5. The variation of J_V^ℓ with respect to J_F^ℓ decreases with increasing ℓ (Fig. 5.9). This decrease

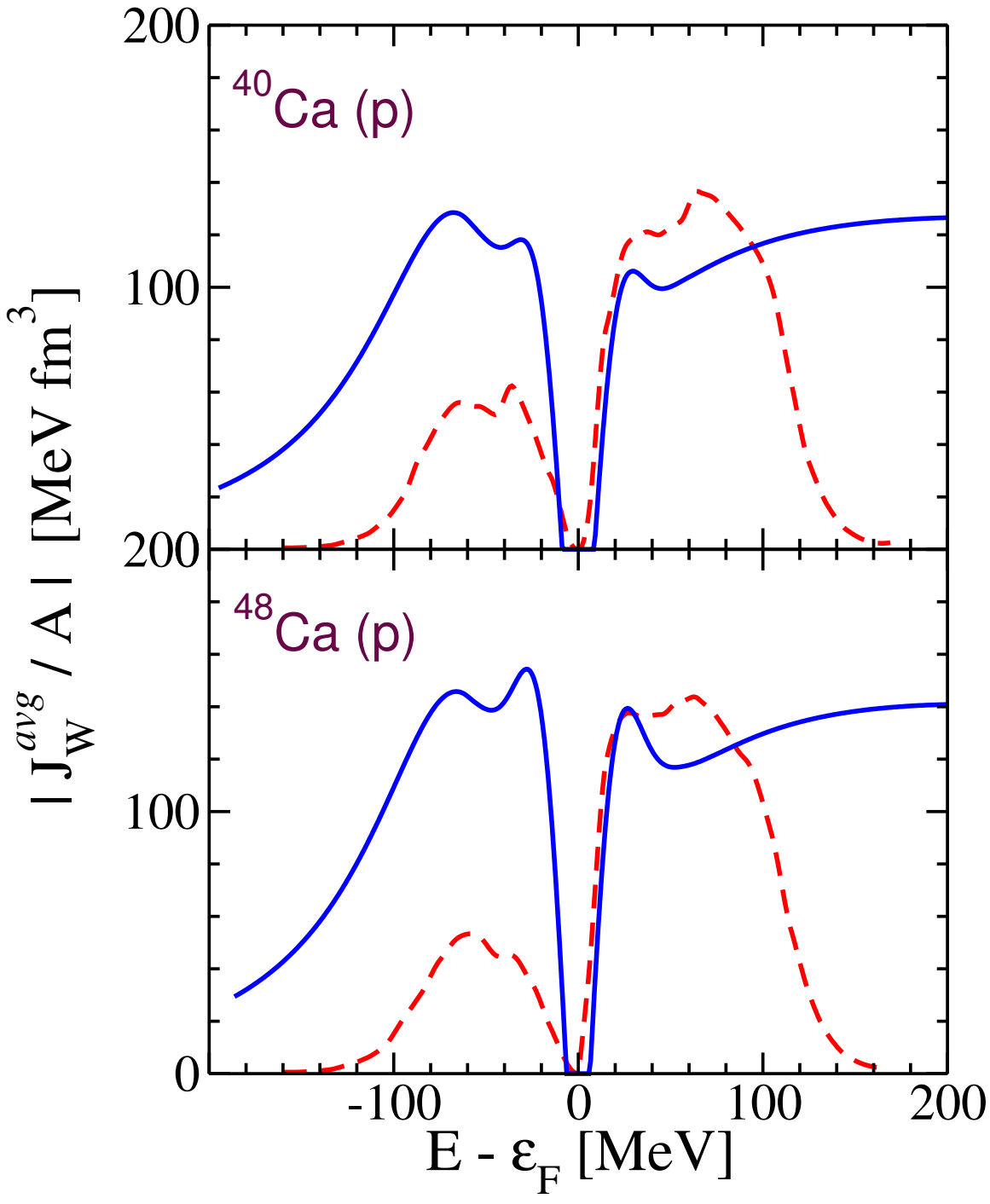

Figure 5.8: The FRPA results for the average over all ℓ-channels (dashed) are compared with the DOM result (solid), corrected for nonlocality. Published in Ref. [32].

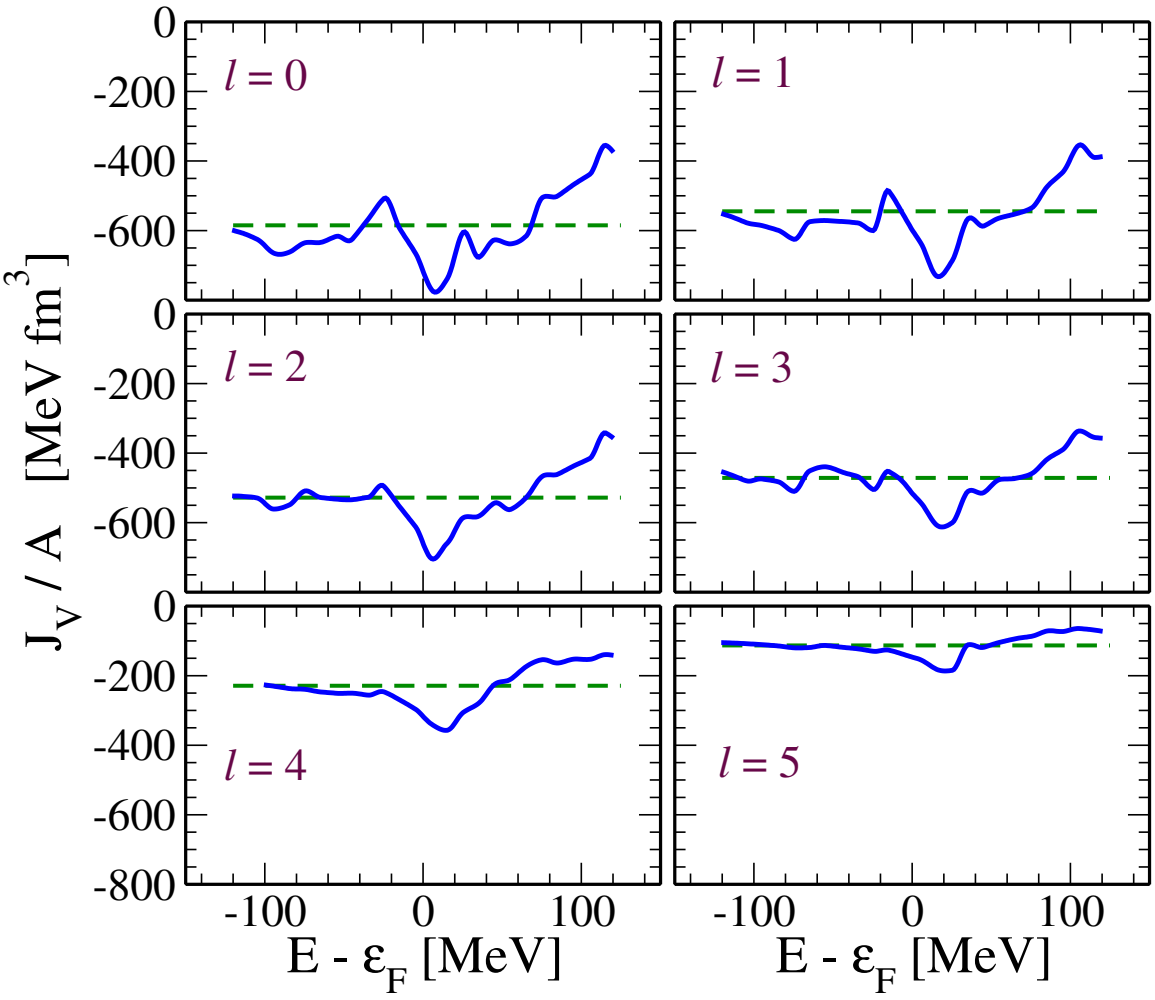

Figure 5.9: Volume Integrals of Re Σ_0^ℓ for neutrons in ^{40}Ca. The horizontal, dashed lines are the volume integrals of $\Sigma_0^{\infty,\ell}(\varepsilon_F)$. Published in Ref. [32].

reflects a similar reduction of the imaginary parts, J_W^ℓ, to which J_V^ℓ are linked through the dispersion relation.

Note that near ε_F the volume integral changes rapidly with energy. This feature is also captured in the DOM parametrization of the dispersive potential, as seen in Fig. 5.10, which compares the volume integral of the DOM dispersive correction, J_D^{DOM}, with the corresponding ℓ-averaged FRPA result, J_D^{avg}. The volume integrals shown are for protons in ^{40}Ca and ^{48}Ca in the energy range where the truncation of the model space is expected to be unimportant.

J_D^{avg} is roughly symmetric about ε_F in the energy domain $|E-\varepsilon_F| < 25$ MeV, like

Table 5.1: Particle-Hole Gaps in MeV. Published in Ref. [32].

Nucleus	Neut./Prot.	AV18	N3L0	DOM	Exp.
^{40}Ca	ν	10.7	12.0	7.79	7.23
	π	7.9	12.1	7.20	7.24
^{48}Ca	ν	4.8	4.9	2.83	4.79
	π	11.6	13.5	6.78	6.18
^{60}Ca	ν	4.9	6.5	4.95	-
	π	10.4	12.3	6.13	-

the DOM, but is somewhat smaller in magnitude. For more negative energies J_D^{avg} and J_D^{DOM} show a similar dependence on energy, whereas for more positive energies J_D^{avg} and J_D^{DOM} diverge. The energy-dependent correction to Σ^∞ can only be calculated for negative energies, and the correction for positive energies would tend to reduce J_D^{avg}, bringing the FRPA result in closer agreement with the DOM result.

Further comparison of FRPA with the DOM self-energy is made in Table 5.1 for the ph-gap. The AV18 seems to provide smaller ph-gaps by 1-2 MeV compared to N3LO. However, in both cases these gaps substantially overestimate the experimental results (see Table 5.1). DOM fits from Ref. [23] are also included in the table and are typically closer to experiment.

5.4.2 Parity Dependence

In Fig. 5.11, the absorption of the negative parity channels is compared with that of the positive parity channels in ^{40}Ca, ^{48}Ca, and ^{60}Ca. The averages $\left(\sum_{\text{even }\ell} J_W^\ell\right)/N_{\text{even }\ell}$ and $\left(\sum_{\text{odd }\ell} J_W^\ell\right)/N_{\text{odd }\ell}$ are compared in order to see the trends more clearly. An interesting feature in ^{40}Ca is that just below ε_F there is more negative parity absorption than for even parity, while just above ε_F the opposite is true.

The effect can be understood in terms of the number of 2p1h and 2h1p states, which are the configurations included beyond the mean-field approximation that are closest to ε_F. In these states, the ph and the hp phonons have negative parity, since the holes are in the *sd*-shell while the particles are in the *pf*-shell. Thus, near ε_F, the

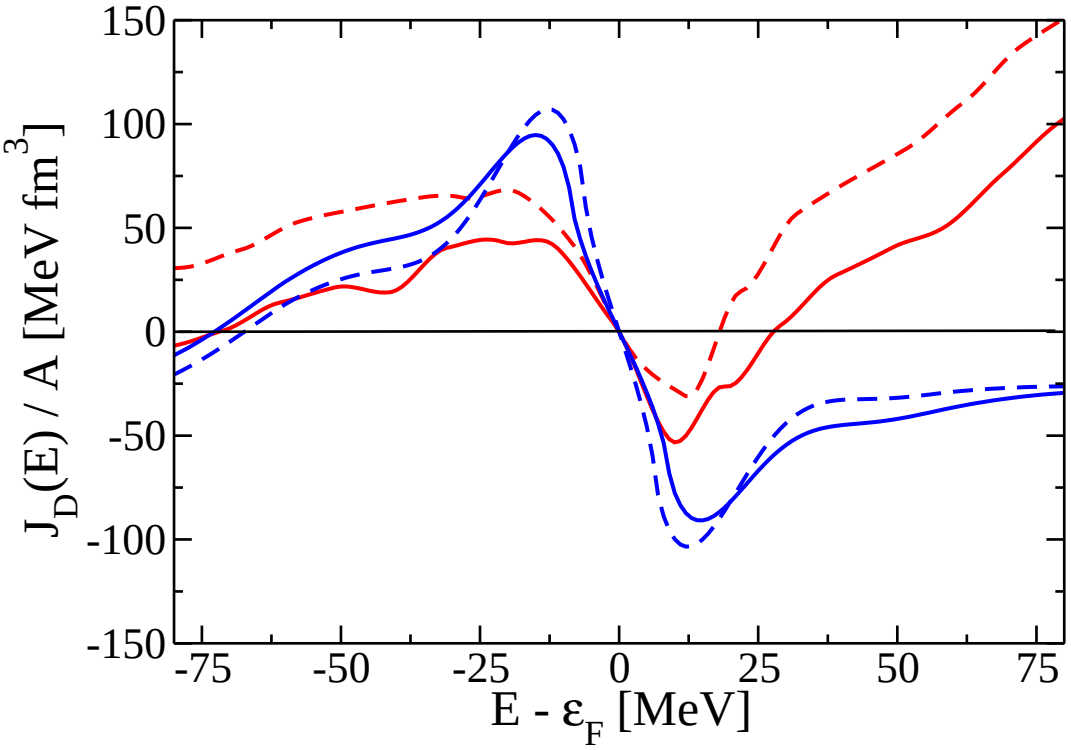

Figure 5.10: Comparison of the FRPA (red) and DOM (blue) subtracted dispersive corrections. The comparison is made for protons in ^{40}Ca (solid) and in ^{48}Ca (dashed).

2h1p states will have negative parity and the 2p1h states will have positive parity.

Proton ph-configurations at low energy continue to have negative parity, as the neutron number increases in the pf-shell. However, phonons with positive parity can be created at energies close to ε_F due to the partial filling of the neutron pf-shell. So, both parities for 2p1h and 2h1p states are possible. As a result, in ^{48}Ca one sees little difference between the absorption from negative and positive parity states.

In ^{60}Ca, which is the next closed shell, the neutron pf-shell is filled and the corresponding low-lying neutron ph configurations again have negative parity, as in ^{40}Ca; but in this case the neutron holes have negative parity corresponding to $\ell = 1$ and 3. Thus, there are more 2h1p states with positive parity near ε_F for the neutrons.

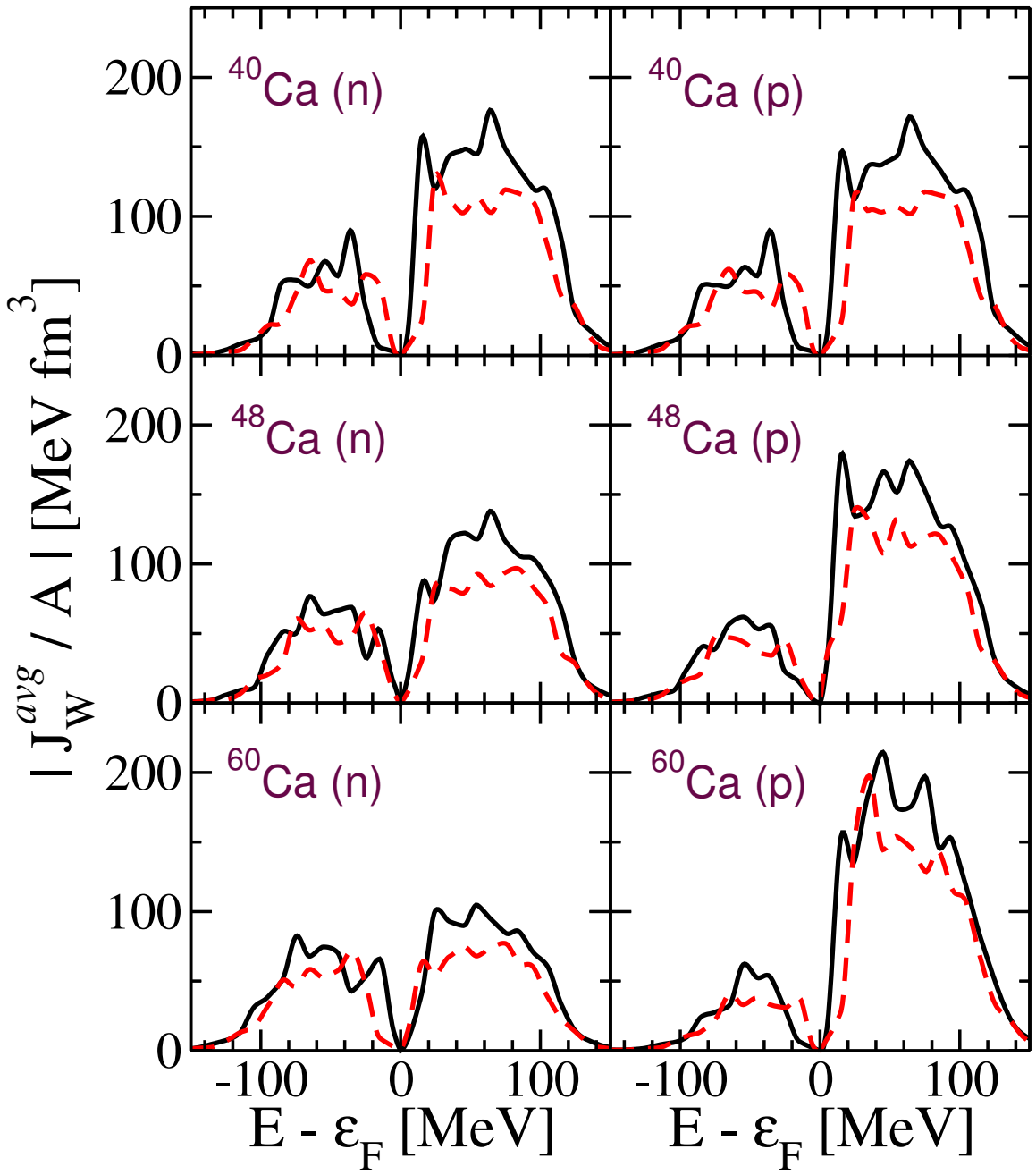

Figure 5.11: J_W averaged over even ℓ-channels (solid) is compared with Jw averaged over odd ℓ-channels (dashed). Published in Ref. [32].

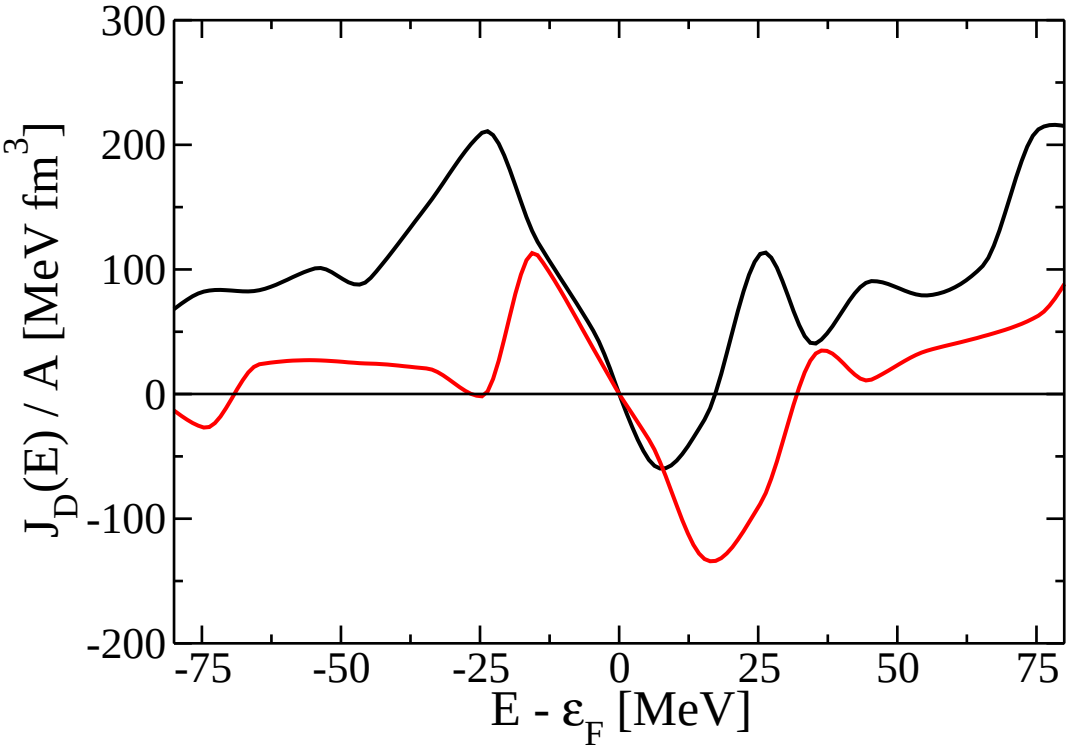

Figure 5.12: $J_D^\ell(E)$ for $\ell = 0$ (black) and $\ell = 1$ (red) for neutrons in ^{40}Ca.

The situation for the protons is similar to the case of ^{40}Ca. The inversion of the dominant parity above and below ε_F is quite general when major shells are filled or depleted and also visible in the partial waves separately.

The parity dependence in the imaginary part of the self-energy results in a corresponding parity dependence in the dispersive correction. This parity dependence is illustrated in Fig. 5.12 for neutrons in ^{40}Ca. Only the $\ell = 0, 1$ contributions are presented. The parity dependence in both the real and imaginary particularly striking in ^{40}Ca. Including some parity dependence in future DOM fits may be able to improve the description of the differential cross sections for low-energy proton scattering on ^{40}Ca. These cross sections are notoriously difficult to fit and were excluded in the DOM fits presented in Refs. [23, 24].

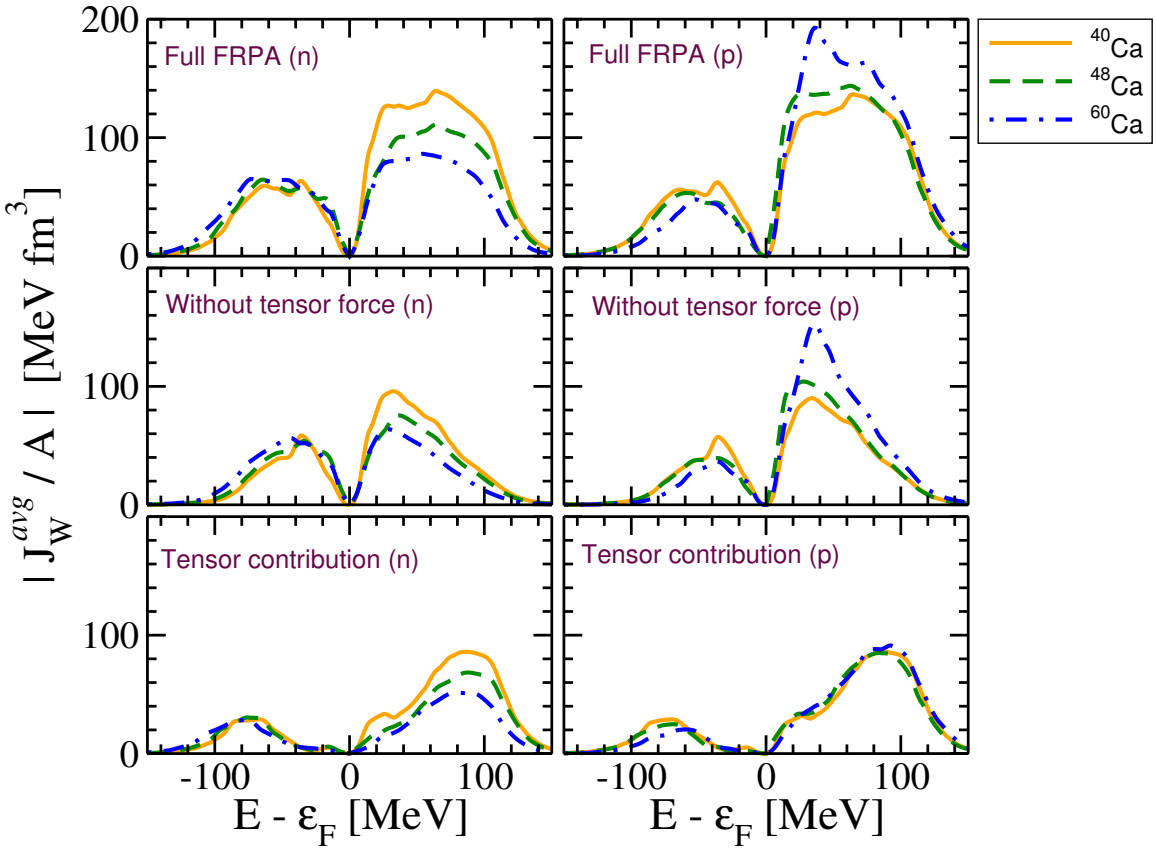

Figure 5.13: Asymmetry dependence of the absorption for neutrons and protons and dependence on tensor correlations. The top panels shows J_W^{avg} for ^{40}Ca (solid) is compared with the results for ^{48}Ca (dashed), and ^{60}Ca (dot-dashed). The middle panels are obtained by suppressing the tensor component in the AV18 interaction. The difference between the top two panels is plotted in the bottom panels to provide a more detailed assessment of the correlations induced by including the tensor force. Published in Ref. [32].

5.4.3 Asymmetry Dependence

The correlations that neutrons and protons experience inside the nucleus depend on the proton-neutron asymmetry ($\alpha = (N - Z)/A$). This asymmetry dependence can be seen, for example, in the existence of halo nuclei and in the appearance of new magic numbers as one ventures off the valley of stability. It can also be inferred from the asymmetry dependence of spectroscopic factors observed in knockout and transfer reactions [57, 63, 66, 67, 92–94], since spectroscopic factors are an indication of how much sp strength is removed through the coupling to more complicated states.

The imaginary part of the nucleon self-energy determines the absorption of sp strength. Understanding its asymmetry dependence is therefore essential for reliable DOM extrapolations toward the drip lines and is also important for the analysis of transfer reactions, as already discussed in Ch. 4. The asymmetry dependence of the FRPA imaginary self-energy is studied in Fig. 5.13 using averaged volume integrals. The top panel shows J_W^{avg} for the three different Ca isotopes. Above ε_F, the FRPA predicts an opposite behavior of protons and neutrons, with the proton (neutron) potential increasing (decreasing) when more neutrons are added, qualitatively in agreement with expectations from the Lane potential model [54].

In the recent DOM analysis from Ref. [24], the asymmetry dependence of the imaginary potential for chains of Ca and Sn isotopes was explored. Both sets of isotopes showed a trend similar to the FRPA result in Fig. 5.13, but in both cases the neutron surface absorption exhibited a very weak asymmetry dependence, whereas for protons the asymmetry dependence was much stronger and tended to increase with asymmetry. A separation between volume and surface effects cannot be carried out uniquely in a fully microscopic approach like the present FRPA, but in general, one can argue that most of the physics at scattering energies below 50 MeV is dominated by surface effects [15, 17] which are covered well by the FRPA. Volume effects pertain to higher energies and are not incorporated as well in the FRPA with the chosen model space.

At energies below the Fermi surface, the overall absorption of both protons and neutrons does not show much variation with changing asymmetry. Current DOM implementations assume that surface absorption is similar above and below the Fermi energy, which is clearly not suggested by the FRPA results. Since previous DOM analyses incorporate much less data from energies below ε_F, the DOM potential at negative energies is much less constrained than at positive energies. Therefore, the FRPA prediction should be checked in future DOM fits that use nonlocal potentials so that more data pertaining to negative energies can be incorporated.

Both the FRPA and the DOM results above indicate that a nucleon becomes more

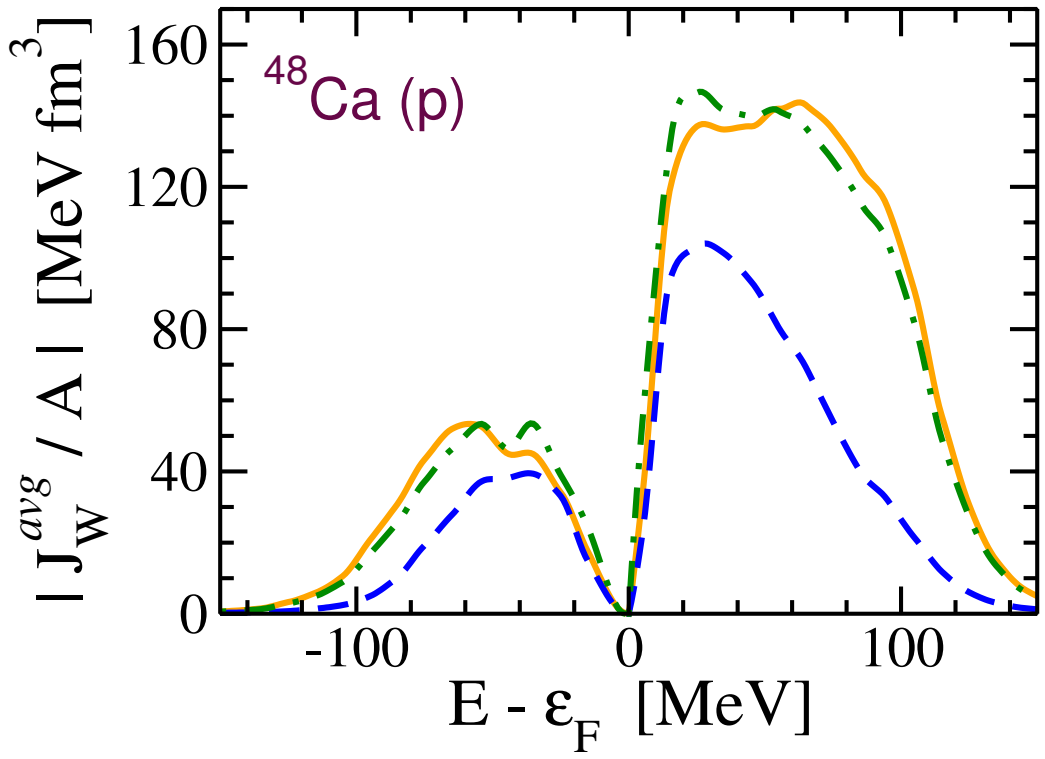

Figure 5.14: Effect of the tensor force and charge exchange on correlations on the proton-^{48}Ca self-energy. The solid curve is the imaginary volume integral J_W^{avg} from the full FRPA calculation, while the dashed curve results from removing the tensor term in the AV18 interaction. The dash-dot curve is obtained by excluding charge exchange from the full calculation. The same results are found for neutrons and the other Ca isotopes. Published in Ref. [32].

correlated when increasing the number of nucleons with opposite isospin projection. This pattern is a rather general feature in nuclear systems that is also found for asymmetric nucleonic matter [95, 96]. FRPA calculations of stable and drip-line nuclei show that this effect results in an asymmetry dependence of spectroscopic factors similar to that observed in knockout reactions, although the overall change from drip line to drip line is comparatively modest [93]. There exist other mechanisms that can affect this quenching besides the coupling to the giant resonance region, including a strong correlation to the ph gap [86] and coupling to the continuum at the drip lines [57].

Since the nucleon self-energy depends on the relative amounts of neutrons and

protons, one expects that the nuclear interaction between protons and neutrons plays a major role in the asymmetry dependence. The tensor force of the nuclear interaction could provide one such mechanism since it is particularly strong in the channel with total isospin $T = 0$, and it has already been shown to influence the evolution of single-particle energies at the Fermi surface [97]. Its influence on the single-particle properties at energies farther removed from ε_F was investigated by recalculating J_W^{avg} with the tensor component of the AV18 interaction suppressed. The result is shown in Fig. 5.14 for protons on ^{48}Ca and in the middle panels of Fig. 5.13 for all isotopes. Removing the tensor force results in a large reduction of absorption at energies $|E - \varepsilon_F| >$30 MeV. Thus, tensor effects have an important impact on scattering at these energies. The difference with the complete solution is plotted in the bottom panels of Fig. 5.13 to highlight the separate effect of the tensor force. It is apparent that the tensor force has a very significant effect on the correlations far from the fermi surface, but it contributes only to the asymmetry dependence of neutron scattering. Thus, correlations other than the tensor dominate in the region near the Fermi surface and are responsible for most of the asymmetry dependence obtained in the full calculation.

Another mechanism that could create an asymmetry dependence is charge-exchange, in which the proton (neutron) projectile is Pauli exchanged with a neutron (proton) in the target. It was argued in Ref. [23] that this process could enhance surface absorption due to the presence of Gamow-Teller resonances, with strength increasing as $\approx 3(N - Z)$. The FRPA self-energy, then, was recalculated with charge-exchange excitations suppressed in the polarization propagator $\Pi(E)$. The results are shown in Fig. 5.14 (dot-dashed line) and suggest that charge-exchange excitations of the target interfere only very weakly with the nucleon-nucleus scattering process.

5.4.4 Analysis of radial dependence

Since the nonlocality of the imaginary part of the self-energy appears to be important for the analysis of elastic scattering data and observables related to quantities below the Fermi energy, incorporating this physics explicitly in a DOM framework seems like a logical step forward for improving the description of the DOM potentials as self-energies. Further insight into the properties of the microscopic FRPA self-energy may provide some guidance for future implementations of nonlocality in the DOM. Therefore, a few simple fits were performed to represent the central part of the imaginary part of the FRPA self-energy in coordinate space at a given energy assuming a form for the potential given by Eq. (3.6), which employs a Gaussian nonlocality projected onto states with good orbital angular momentum. As in Ch. 3, the parameter β controls the degree of nonlocality. The projected potential is represented as

$$W_{NL}^{\ell}(r,r') = W_0\sqrt{f(r)}\sqrt{f(r')}\frac{4}{\pi^{1/2}\beta^3}\exp\left(\frac{-r^2+r'^2}{\beta^2}\right) i^{\ell}(-1)^{\ell} j_{\ell}(iz), \qquad (5.16)$$

where the function $f(r)$ is a conventional Woods-Saxon form factor. The fact that an analytic projection is possible provided the motivation of the choice of Eq. (5.16).

The imaginary part of the FRPA self-energy was fit at an energy of $E - \varepsilon_F = 44$ MeV, where surface physics dominates and the sharper resonances that occur closer to the Fermi energy are avoided. Only the $\ell = 0$ self-energy was fit since it represents the partial wave with the best convergence properties associated with the limited model space considered.

Figure 5.15 displays the diagonal of the central imaginary part of the parametrized self-energy in coordinate space for $\ell = 0$ along with the corresponding FRPA self-energy for ^{40}Ca, ^{48}Ca, and ^{60}Ca. The lines are offset by 5 MeV for the different isotopes. The comparison suggests that Eq. (5.16) is a reasonable representation of the microscopic self-energy and a useful starting point for future choices of functional forms for the DOM.

The parameters from Eq. (5.16) were fitted to the diagonal part of the FRPA

Table 5.2: Parameters from nonlocal fits to the imaginary part of the proton self-energy at $E - \varepsilon_F$=44 MeV for ^{40}Ca, ^{48}Ca, and ^{60}Ca. W_0 is in MeV, r_0, a_0, β are in fm, and J_W is in units of MeV fm^3. Published in Ref. [32].

Isotope	W_0 MeV	r_0 fm	a_0 fm	β fm	$\lvert J_W/A\rvert$	$\lvert J_W/A\rvert$ [FRPA]
^{40}Ca	14.1	1.23	1.23	1.54	187	188
^{48}Ca	16.1	1.32	1.30	1.54	242	241
^{60}Ca	13.6	1.50	1.50	1.49	266	268

self-energy (imaginary) and the volume integral J_W^ℓ. The properties of the imaginary part of the FRPA self-energy in terms of its diffuseness a_0, radius r_0, depth W_0 and nonlocality content are summarized in Table 5.2 for the three different nuclei. The values for the diffuseness are larger than standard ones ($\simeq 0.70$) and increase with neutron number. The radius parameter exhibits a similar nonstandard trend. The value of the nonlocality parameter β is also substantially larger than typically assumed for real nonlocal potentials. The DOM analysis of Ref. [30], which is also discussed in Ch. 3, yielded $\beta = 0.9$ fm for the nonlocal HF potential.

The DOM fit to Ca isotopes in Ref. [23] suggests that surface terms of the neutron imaginary potential should change very little as the neutron drip line is approached [23]. In order to compare this trend with the one in the microscopic potential, the FRPA self-energy over was integrated over one radial coordinate,

$$\Sigma_{int}^\ell(r;E) = \int dr' r'^2 \Sigma_0^\ell(r,r';E), \tag{5.17}$$

for the partial wave $\ell = 0$. This is compared to the DOM fit in Fig. 5.16 at the same energy $E - \varepsilon_F = 44$ MeV. In accordance with the DOM analysis, the strength of the proton imaginary part increases with neutron number in the surface region. The neutron potential changes very little at the surface between ^{40}Ca and ^{48}Ca, also in agreement with the DOM analyses in Refs. [23, 24], but decreases more substantially when going all the way to ^{60}Ca. Thus, an extrapolation of the surface term to very large asymmetries may not be simple.

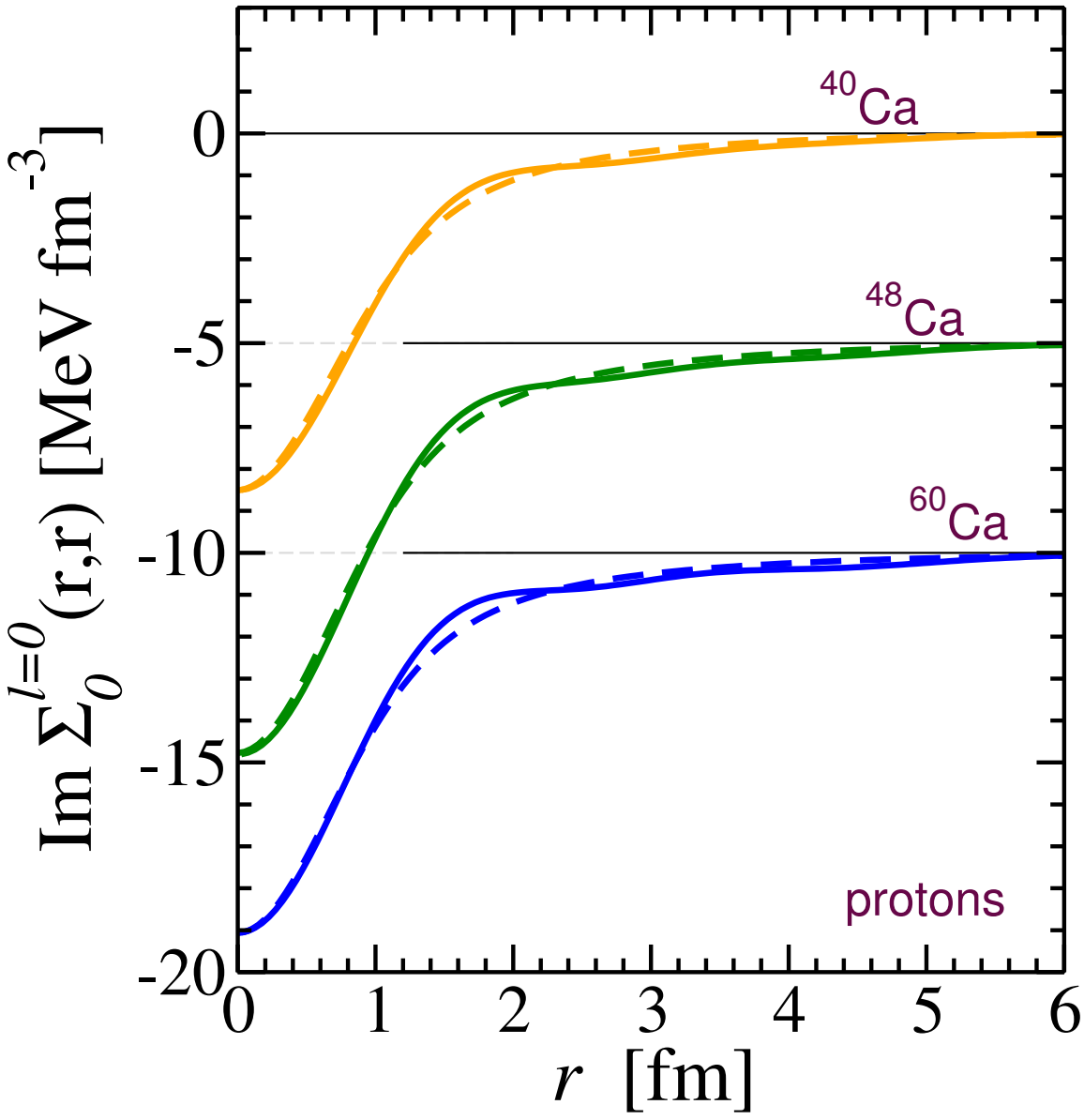

Figure 5.15: Diagonal part of FRPA imaginary self-energy for protons at $E-\varepsilon_F$=44 MeV (solid) and the corresponding parametrized self-energy (dashed). The results shown are for $\ell = 0$ and are offset by 5 MeV for each subsequent nucleus.. Published in Ref. [32].

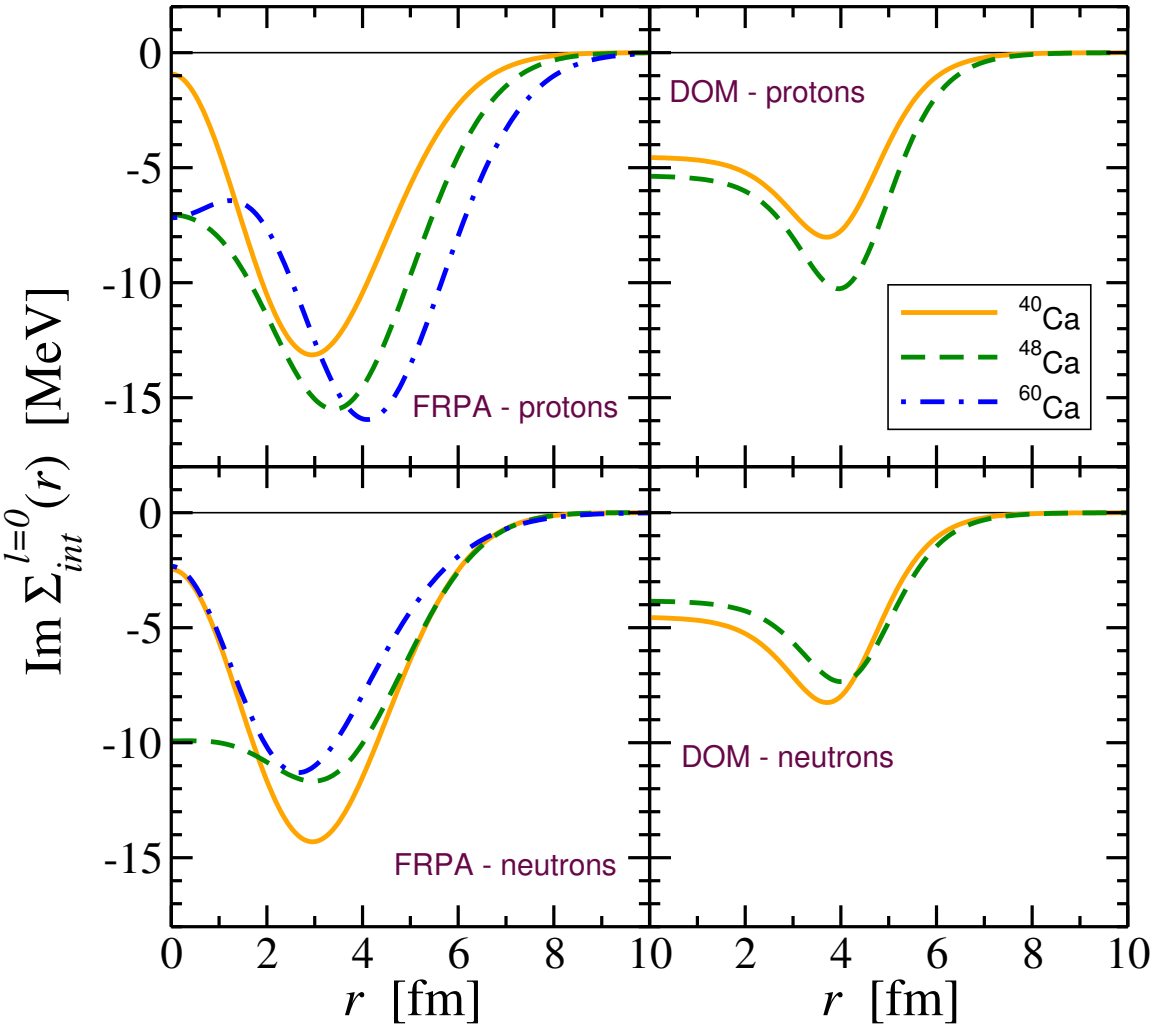

Figure 5.16: *Left panels:* FRPA imaginary self-energy integrated over r' for protons in ^{40}Ca (solid), ^{48}Ca (dashed), ^{60}Ca (dot-dashed). The results shown are for $\ell = 0$ and at an energy of 44 MeV above ε_F. *Right panels:* For comparison, the DOM imaginary potentials at the same energy are shown for ^{40}Ca and ^{48}Ca. Since these are local, they have been corrected for nonlocality by the k-mass. Published in Ref. [32].

5.5 Conclusions

In this investigation, an attempt was made to establish links between the DOM—an empirical approach to the nuclear many-body problem based on the framework of the Green's function method and relevant experimental data—and the microscopic FRPA approach. An analysis of the volume integrals calculated from both approaches proved to be a useful link, and on the whole, both the DOM and the FRPA produced similar results. However, there were some significant and illuminating differences.

The FRPA exhibits some important shell effects as neutrons are added to ^{40}Ca. In particular, there is a parity dependence in ^{40}Ca and ^{60}Ca, but not in ^{48}Ca, where both parities occur at low energy due to the partial filling of the neutron pf-shell. Such an effect has not hitherto been taken into account in the DOM. Inspection of the imaginary volume integrals generated by the FRPA also calls into question the assumption in most DOM analyses that the imaginary part is symmetric about ε_F for the surface absorption, suggesting that absorption of high-ℓ waves corresponding to unoccupied orbits is suppressed below ε_F. At energies about 40 MeV above or below ε_F, a substantial contribution of the absorption is due to the NN tensor force. However, this term in the NN interaction does not greatly influence the asymmetry dependence of the absorption in the FRPA, indicating that the most of the observed asymmetry dependence is due to central components of the interaction. In addition, the decrease of neutron absorption at positive energies appears to be somewhat stronger than what has been deduced so far from DOM fits. The tensor force is not explicitly included in current versions of the DOM, but work is being done in this direction. In addition, the decrease of neutron absorption at positive energies appears to be somewhat stronger than what has been deduced so far from DOM fits.

The ℓ-dependence of the FRPA imaginary self-energy is also noteworthy and points to the relevance of nonlocality in the absorption process. This ℓ-dependence may play an important role in explaining data like the nuclear charge density that are associated with properties of the self-energy below the Fermi energy. Its role in

scattering processes remains to be studied as well and has important consequences for the analysis of transfer and knockout reactions which are sensitive to interior wave functions generated by optical potentials.

Chapter 6

Including SRC in DOM

The FRPA does a good job of incorporating physics associated with LRC, but it is not suited for studying SRC because it does not explicitly consider high-momenta. The procedure that is used to incorporate SRC only calculates the real part associated with ladder diagrams that occur outside the model space, and this part can only be calculated for negative energies. In this chapter the DOM is compared with a microscopic calculation that includes high-momenta. The microscopic calculation of the self-energy for a nucleon in ^{40}Ca was provided by H. Müther and A. Polls and was done using the CDBonn interaction. The self-energy from this calculation does not accurately take into account LRC but provides a fuller treatment of SRC. The calculation was only done for neutrons, but it was done in an isospin conserving way so that the self-energy can also be used to study protons when a Coulomb potential is added. Some of the results in this chapter are in Ref. [33].

6.1 Details of the Microscopic Calculation

The method used to obtain the microscopic nucleon self-energy for ^{40}Ca is the same as the one used in Refs. [7, 50, 51], which was applied to ^{16}O. The HF and second-order diagrams are calculated with an effective interaction that includes only pp intermediate states. This is the so-called $\mathcal{G}$-matrix, which for a finite nucleus (FN)

can be represented in operator form by

$$\mathcal{G}_{FN}(E) = V + VG^{pp}_{FN}(E)\mathcal{G}_{FN}(E), \tag{6.1}$$

where the noninteracting propagator $G^{pp}_{FN}(E)$ represents two particles above the Fermi sea of the finite nucleus taking into account the Pauli principle and V is the bare nucleon-nucleon interaction. The simplest implementation of G^{pp}_{FN} involves plane-wave intermediate states (possibly orthogonalized to the bound states), but even such a simple assumption leads to a prohibitive calculation to solve Eq. (6.1).

A more tractable solution, developed in Refs. [98, 99], first calculates a $\mathcal{G}$-matrix in nuclear matter at a fixed density and fixed energy according to

$$\mathcal{G}_{NM}(E_{NM}) = V + VG^{pp}_{NM}(E_{NM})\mathcal{G}_{NM}(E_{NM}). \tag{6.2}$$

The energy E_{NM} is chosen below twice the Fermi energy of nuclear matter for a kinetic energy sp spectrum and the resulting $\mathcal{G}_{NM}$ is therefore real. In general, an effective interaction $\mathcal{T} = V + V(G^{(0)}_1 + G^{(0)}_2)\mathcal{T}$ can be rewritten as $\mathcal{T} = \mathcal{T}_1 + \mathcal{T}_1 G^{(0)}_2 \mathcal{T}$, where $\mathcal{T}_1 = V + VG^{(0)}_1\mathcal{T}_1$. Writing $G^{pp}_{FN} = G^{pp}_{FN} - G^{pp}_{NM} + G^{pp}_{NM}$, Eq. (6.1) can then be solved in terms of $\mathcal{G}_{NM}$:

$$\mathcal{G}_{FN}(E) = \mathcal{G}_{NM} + \mathcal{G}_{NM}\left\{G^{pp}_{FN}(E) - G^{pp}_{NM}\right\}\mathcal{G}_{FN}(E), \tag{6.3}$$

where the explicit reference to E_{NM} is dropped. The main assumption to make the self-energy calculation manageable is to drop all terms higher than second order in $\mathcal{G}_{NM}$, leading to

$$\mathcal{G}_{FN}(E) = \mathcal{G}_{NM} - \mathcal{G}_{NM}G^{pp}_{NM}\mathcal{G}_{NM} + \mathcal{G}_{NM}G^{pp}_{FN}(E)\mathcal{G}_{NM}, \tag{6.4}$$

where the first two terms are energy-independent. Since a nuclear-matter calculation already incorporates all the important effects associated with SRC, it is reasonable

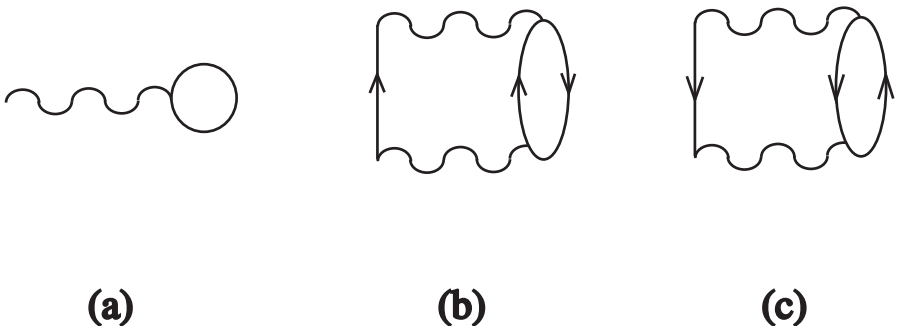

Figure 6.1: Graphical representation of the BHF (a), the two-particle–one-hole contribution (b) and one-particle–two-hole term (c) to the self-energy of the nucleon. The $\mathcal{G}_{NM}$-matrix is indicated by the wiggly line. Published in Ref. [33].

to assume that the lowest-order iteration of the difference propagator in Eq. (6.4) represents an accurate approximation to the full result. This assertion does require further confirmation in future studies.

The self-energy contributions are obtained by closing each term in Eq. (6.4) with a hole. The resulting lowest-order term is shown in Fig. 6.1(a) and is similar to a Brueckner-Hartree-Fock (BHF) self-energy. Strictly speaking the genuine BHF approach involves self-consistent sp wave functions, as in the HF approximation, whereas in the approach described above the occupied states are determined a bound harmonic oscillator. However, the oscillator wavefunctions are a good approximation to the self-consistent BHF wavefunctions [7], so the BHF abbreviation is used.

The third term in Eq. (6.4) is second order in $\mathcal{G}_{NM}$ and corresponds to the self-energy diagram in Fig. 6.1(b), which represents coupling to 2p1h states. In the calculation, harmonic oscillator states were assumed for the occupied (hole) states and plane waves for the intermediate unbound particle states, incorporating the correct energy and density dependence characteristic of a finite nucleus $\mathcal{G}_{FN}$-matrix. In a similar way, one can construct the second-order self-energy contribution depicted in Fig. 6.1(c) which has an imaginary part below the Fermi energy and includes the coupling to 2h1p states. The second term in Eq. (6.4) is also second order in $\mathcal{G}_{NM}$ but calculated with a two-particle propagator from nuclear matter. This term is static

and, because of the choice of starting energy, it is also real.

As already mentioned, the real parts associated with diagrams (b) and (c) of Fig. 6.1 are calculated by first determining the imaginary parts and employing the appropriate dispersion relation. The resulting (irreducible) self-energy then reads

$$\begin{aligned} \Sigma^* &= \Sigma^*_{BHF} + \Delta\Sigma^* \\ &= \Sigma^*_{BHF} + \left(\mathrm{Re}\ \Sigma^*_{2p1h} - \Sigma^*_c + \mathrm{Re}\ \Sigma^*_{1p2h}\right) \\ &+ \ i\left(\mathrm{Im}\ \Sigma^*_{2p1h} + \mathrm{Im}\ \Sigma^*_{1p2h}\right) \end{aligned} \tag{6.5}$$

in obvious notation. This self-energy is employed in the sp basis denoted by states $|\{k(\ell\frac{1}{2})jm_j\}\rangle$, characterized by wave vector, orbital, spin, total angular momentum and its projection (suppressing isospin). The quantum numbers ℓ, j and m_j are conserved and the self-energy does not depend on m_j. The calculation of the $\mathcal{G}_{FN}$-matrix in this basis, however, requires several basis transformations that are computationally expensive [7]. Results for protons can be obtained by making use of isospin conservation for ^{40}Ca and adding in the Coulomb contribution separately.

The CDBonn interaction [100, 101], which is a relatively soft [96], was used for the realistic nucleon-nucleon interaction V in Eq. (6.2). The microscopic calculations were performed in wave-vector space for partial waves up to $\ell_{max} = 4$.

6.1.1 Solution of the Dyson Equation

The sp propagator in momentum space can be obtained from the following version of the Dyson equation [36]

$$G_{\ell j}(k,k';E) = \frac{\delta(k-k')}{k^2} G^{(0)}(k;E) + G^{(0)}(k;E)\Sigma_{\ell j}(k,k';E)G^{(0)}(k;E), \tag{6.6}$$

where $G^{(0)}(k;E) = (E - \hbar^2k^2/2m + i\eta)^{-1}$ corresponds to the free propagator and $\Sigma_{\ell j}$ is the *reducible* self-energy. The latter can be obtained by iterating the irreducible

self-energy to all orders

$$\Sigma_{\ell j}(k,k';E) = \Sigma^*_{\ell j}(k,k';E) + \int dq q^2 \Sigma^*_{\ell j}(k,q;E) G^{(0)}(q;E) \Sigma_{\ell j}(q,k';E). \tag{6.7}$$

Below the Fermi energy the hole spectral function is determined by the imaginary part of the propagator

$$S_{\ell j}(k;E) = \frac{1}{\pi} \text{Im } G_{\ell j}(k,k;E). \tag{6.8}$$

For negative energies, the free propagator has no imaginary part and so according to Eq. (6.6) the spectral function reads

$$S_{\ell j}(k;E) = \frac{1}{\pi} G^{(0)}(k;E) \text{Im } \Sigma_{\ell j}(k,k;E) G^{(0)}(k;E), \tag{6.9}$$

for energies where the imaginary part of the self-energy does not vanish. The total spectral strength at E for a given ℓj combination,

$$S_{\ell j}(E) = \int_0^\infty dk \ k^2 \ S_{\ell j}(k;E), \tag{6.10}$$

yields the spectroscopic strength per unit of energy.

The imaginary part of the CDBonn self-energy vanishes between the maximum energy of 2h1p and the minimum energy of 2p1h states. Inside this domain, discrete solutions to the Dyson equation are obtained from the standard version of the Dyson equation

$$G_{\ell j}(k,k';E) = \frac{\delta(k-k')}{k^2} G^{(0)}(k;E) + G^{(0)}(k;E) \int_0^\infty dq \ q^2 \ \Sigma^*_{\ell j}(k,q;E) G_{\ell j}(q,k';E). \tag{6.11}$$

Following standard steps [36], Eq. (6.11) can be rewritten into an eigenvalue problem for the overlap function

$$\frac{k^2}{2m} \phi^n_{\ell j}(k) + \int dq q^2 \Sigma^*_{\ell j}(k,q;\varepsilon^-_n) \quad \phi^n_{\ell j}(q) \quad = \varepsilon^-_n \phi^n_{\ell j}(k), \tag{6.12}$$

where

$$\varepsilon_n^- = E_0^A - E_n^{A-1}. \tag{6.13}$$

The overlap functions are actually given by $\sqrt{S_{\ell j}^n}\phi_{\ell j}^n(k)$, where $S_{\ell j}^n$ is the spectroscopic factor, and $\phi_{\ell j}^n(k)$ is normalized to unity. The spectroscopic factor is given by

$$S_{\ell j}^n = \left(1 - \left.\frac{\partial \Sigma_{\ell j}^*(\alpha_{qh}, \alpha_{qh}; E)}{\partial E}\right|_{\varepsilon_n^-}\right)^{-1}, \tag{6.14}$$

which was already discussed in Ch. 2. Following a similar procedure, the overlap functions for the bound states above the Fermi energy can be obtained.

The momentum distribution for a given ℓj is obtained from

$$n_{\ell j}(k) = n_{\ell j}^c(k) + n_{\ell j}^q(k), \tag{6.15}$$

where the continuum contribution is obtained by integrating the spectral function up to corresponding threshold

$$n_{\ell j}^c(k) = \int_{-\infty}^{\varepsilon_T^-} dE\ S_{\ell j}(k; E) \tag{6.16}$$

and the contribution of the discrete quasihole states reads

$$n_{\ell j}^q(k) = \sum_n S_{\ell j}^n \left|\phi_{\ell j}^n(k)\right|^2. \tag{6.17}$$

For protons the total momentum distribution (normalized by the number of protons Z) is obtained from

$$n(k) = \frac{1}{Z}\sum_{\ell j}(2j+1)n_{\ell j}(k), \tag{6.18}$$

with a similar result for the neutron distribution.

The continuum contribution to the one-body density matrix reads

$$n^c_{\ell j}(k',k) = \frac{1}{\pi}\int_{-\infty}^{\bar{\varepsilon_T}} dE\ S_{\ell j}(k,k';E) \tag{6.19}$$

where

$$S_{\ell j}(k,k';E) = \frac{1}{\pi}G^{(0)}(k;E)\text{Im}\ \Sigma_{\ell j}(k,k';E)G^{(0)}(k';E) \tag{6.20}$$

corresponds to the nondiagonal spectral density. The one-body density matrix also receives a contribution from the quasiholes according to

$$n^q_{\ell j}(k',k) = \sum_n S^n_{\ell j}\phi^{n*}_{\ell j}(k)\phi^n_{\ell j}(k'). \tag{6.21}$$

The total one-body density matrix is then given by

$$n_{\ell j}(k',k) = n^q_{\ell j}(k',k) + n^c_{\ell j}(k',k). \tag{6.22}$$

By diagonalizing the one-body density matrix given in Eq. (6.22) one obtains the natural orbits for each ℓj combination together with the corresponding occupation numbers. It is therefore possible to write

$$n_{\ell j}(k,k') = \sum_i n^{no}_{i\ell j}\phi^{no^*}_{i\ell j}(k)\phi^{no}_{i\ell j}(k'), \tag{6.23}$$

with $n^{no}_{i\ell j}, \phi^{no}_{i\ell j}(k)$ the corresponding occupation numbers and wave functions for natural orbit i.

6.2 Results

6.2.1 Spectral Functions

In Fig. 6.2 the $d_{3/2}$ spectral function as a function of momentum, $S(k;E)$ is shown for different negative energies. The $d_{3/2}$ orbit is the last one that is mostly occupied

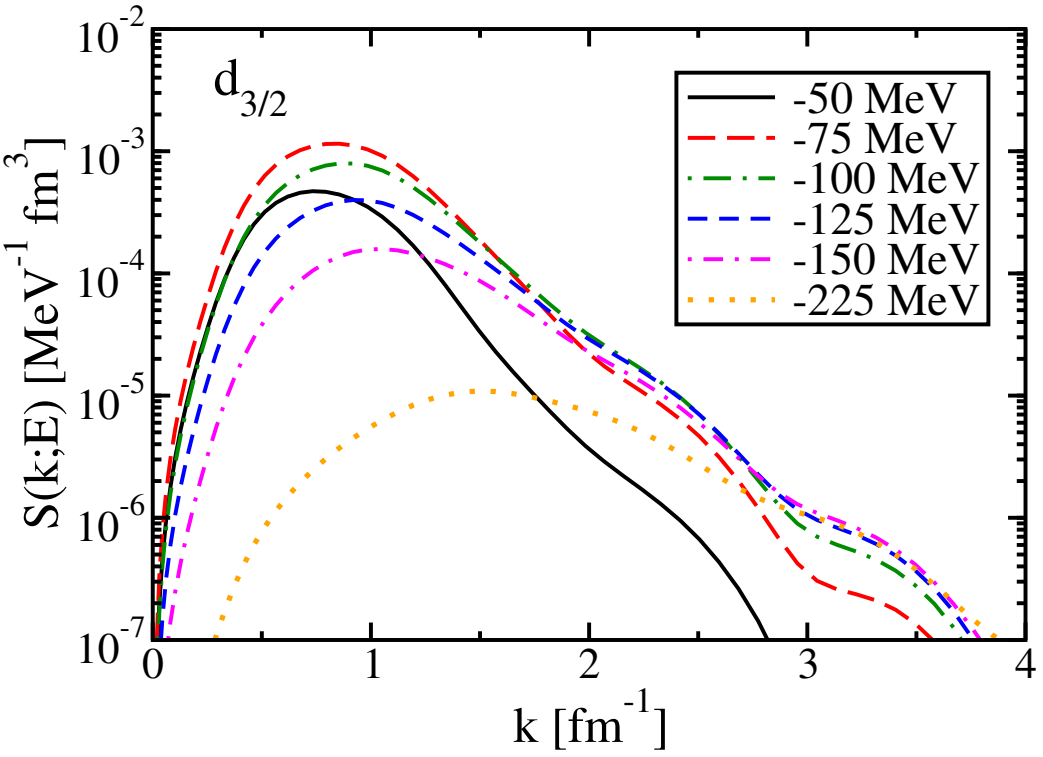

Figure 6.2: Momentum-space spectral function for neutron $d_{3/2}$ quantum numbers at different energies in ^{40}Ca. Published in Ref. [33].

in ^{40}Ca and the momentum content of this state for the energy closest to the Fermi energy (-50 MeV) is similar to what was found before for the $p_{1/2}$ orbit in ^{16}O [50]. In both cases, there is no substantial high-momentum strength at energies near the Fermi energy. As illustrated in Fig. 6.2, the strength at higher momenta increases with increasing excitation energy (decreasing energy), as expected and consistent with earlier calculations [7]. The spectral functions for the valence hole in ^{16}O from Refs. [7, 50] exhibit somewhat larger strength at high-momenta, but this difference could be a result of using a different NN interaction. In this earlier work the Bonn-B potential [102] was employed, and is apparently a harder interaction than the CDBonn interaction [100, 101]. The absence (presence) of high momenta near (far below) the Fermi energy is a simple consequence of simultaneous energy and momentum conservation and is well-documented for nuclear matter [103].

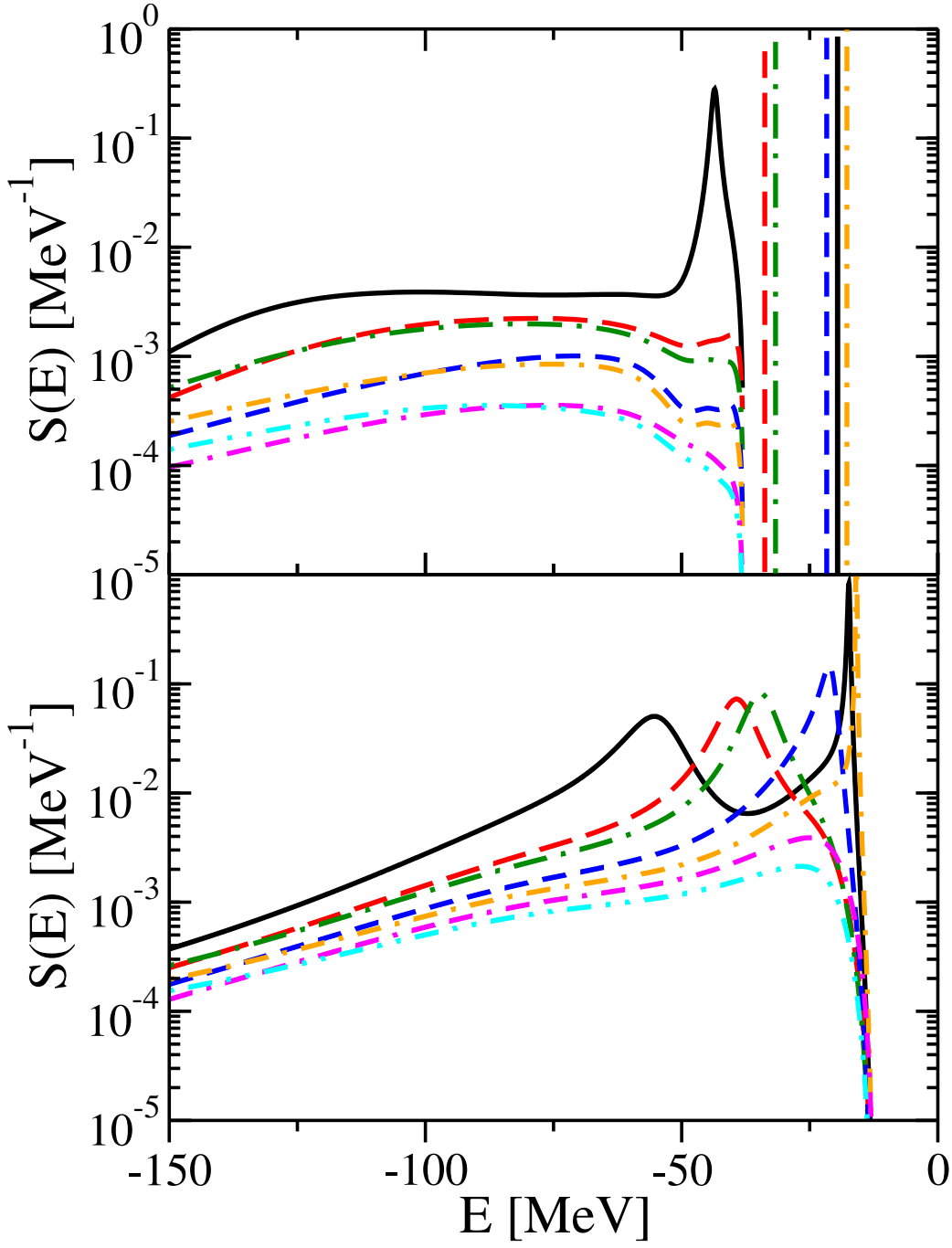

Figure 6.3: Comparison of spectral functions from present work shown in panel (a) with those from a DOM analysis using a nonlocal potential in panel (b). The results are for neutrons in ^{40}Ca. Results are shown for the following ℓj combinations: $s_{1/2}$ (solid), $p_{3/2}$ (long-dash), $p_{1/2}$ (long-dash-dot), $d_{5/2}$ (dash), $d_{3/2}$ (dash-dot), $f_{7/2}$ (dash-dash-dot), and $f_{5/2}$ (dash-dot-dot). Published in Ref. [33].

The behavior of the spectral functions in Fig. 6.2 is somewhat different from the DOM results shown in Fig 3.6, which are also discussed in Ref. [30]. For example, the DOM spectral functions $S(k;E)$ the $d_{3/2}$ level in ^{40}Ca show more high-momentum strength at the lower excitation energies ($E > -75$ MeV) than the corresponding microscopic spectral functions. The most important difference, though, is that the energy-dependence at high-momenta is weaker in the DOM results than in the microscopic results.

In the top panel (a) of Fig. 6.3 the discrete and continuum contributions to the spectral strength [see Eq. (6.10)] are shown as a function of the energy for various ℓj channels for neutrons in ^{40}Ca. Results are shown for the following ℓj combinations: $s_{1/2}$ (solid), $p_{3/2}$ (long-dash), $p_{1/2}$ (long-dash-dot), $d_{5/2}$ (dash), $d_{3/2}$ (dash-dot), $f_{7/2}$ (dash-dash-dot), and $f_{5/2}$ (dash-dot-dot). In the bottom panel (b) the corresponding DOM strength functions are shown for comparison. These were obtained in the way discussed in Ch. 3 using the DOM self-energy from Ref. [23], which has an imaginary part that ends at $\varepsilon_T^- = \varepsilon_F$ and includes a surface term to account for LRC. The resulting strength distribution is therefore continuous with sharp peaks near the Fermi energy, where the imaginary part is small. These peaks are represented by discrete ones (normalized by spectroscopic factors in the figure) for the CDBonn self-energy. Because the coupling to LRC is deemphasized, the imaginary part of the CDBonn self-energy ends at a much lower energy $\varepsilon_T^- = -38$ MeV. The peaks from the DOM result correspond closely to the location of the experimental sp states, and the CDBonn peaks near the Fermi energy are not too different from the DOM result. For the deeply bound $s_{1/2}$ peak, the CDBonn result underestimates the binding by a substantial amount as compared to the DOM result, which is consistent with a corresponding proton peak observed in the $(e, e'p)$ reaction [44].

From Fig. 6.3, it is evident that the microscopic self-energy generates more sp strength at energies below the deeply-bound $s_{1/2}$ peak than the DOM self-energy used in Ref. [30]. The greater sp strength for $E \lesssim -75$ MeV can be attributed to a proper inclusion of SRC, since much of the spectral strength at these energies comes

Table 6.1: Neutron sp strength for the various ℓj combinations.

ℓj	DOM	CDBonn
$s_{1/2}$	3.74	3.63
$p_{1/2}$	2.02	1.87
$p_{3/2}$	4.15	3.74
$d_{3/2}$	3.69	3.76
$d_{5/2}$	5.83	5.56
$f_{5/2}$	0.65	0.20
$f_{7/2}$	1.27	0.25

from high-momentum components so reflects the behavior of the spectral function in Fig. 6.2. Another important difference is that the sp strength decreases more quickly with increasing ℓ in the microscopic approach than in the DOM. This feature has important consequences for the number of particles calculated from the corresponding spectral functions according to

$$N_{calc} = \sum_{\ell j}(2j+1)\int_{-\infty}^{\varepsilon_F^-} dE\ S_{\ell j}(E). \tag{6.24}$$

The total particle number calculated with the CDBonn spectral strength distributions converges well with increasing ℓ. When the two partial waves with $\ell = 4$ are included the number of neutrons is $N_{calc} = 19.3$. The corresponding DOM result exhibits a much slower convergence as illustrated in Fig. 6.3, and crosses 20 already at the $f_{5/2}$ orbit [30]. Table 6.1 shows the sp strength in each ℓj-channel considered in the DOM and CDBonn analyses. In general, the CDBonn sp strengths are smaller, especially for the $\ell = 3$ states, which are empty in the IPM.

This difference in convergence is arguably due to the fact that the imaginary part of the microscopic self-energy is nonlocal whereas the imaginary part of the DOM potential is purely local. As in the case of the FRPA, the imaginary part of the present microscopic self-energy shows a substantial reduction of strength with increasing ℓ, especially for negative energies. This reduction can be seen in Fig. 6.15 of

Sec. 6.2.7 (which will be discussed in more detail later) and appears to be due in large part to nonlocality. Since the existence of an imaginary part at negative energies is responsible for the occupation of states that are empty in the IPM picture, the weaker sp strength in the CDBonn self-energy for the higher ℓ-channels is a consequence of a weaker imaginary part.

Table 6.2 compares the sp strength in the ℓ-channels up to $\ell = 3$. The columns labeled "occupied" show the sp strength of the orbits that are fully occupied in the IPM, which for ^{40}Ca are the $0s_{1/2}$, $1s_{1/2}$, $0p_{3/2}$, $0p_{1/2}$, $0d_{5/2}$ and $0d_{3/2}$ states. The sp strengths associated with these states were obtained from their respective occupation numbers. Referring to the table, one can see that the DOM and CDBonn calculations give similar results for the "occupied" states. Indeed, summing up the strengths, the DOM gives 17.9 particles and the CDBonn gives 18.1 particles.

The columns labeled "empty" in Table 6.2 show the sp strength of the orbits that are empty in the IPM, such as the $0f_{7/2}$, $1p_{3/2}$ or $2s_{1/2}$ states. These sp strengths were obtained by subtracting the sp strengths of the "occupied" states from the total sp strengths, which are given in Table 6.1. Clearly, the reason for the lack of convergence in particle number in the DOM is because the imaginary part of the potential is too strong at negative energies. The DOM imaginary potential below ε_F is responsible for the occupation of 3.44 particles which are empty in the IPM, while the microscopic calculation generates only 0.88 particles of these "empty" states below ε_F. This latter number would actually be somewhat higher if LRC were fully incorporated, but based on the results of Ch. 5, the $\ell = 0, 1$ orbits would be the ones most affected and would probably be more in line with the DOM results for these orbits (see *e.g.* Fig. 5.6).

The last column in Table 6.2 shows the ratio of the DOM "empty" sp strength to the CDBonn "empty" sp strength for each ℓ orbit. The ratio increases with ℓ indicating that the absorption in the microscopic calculation decreases with increasing ℓ, since the DOM absorption does not depend on ℓ. All these things lead to the conclusion that the nonlocality of the imaginary part of the self-energy plays an important role in generating the correct number of particles from a DOM self-energy.

Table 6.2: Neutron sp strength for different ℓ states up to $\ell = 3$.

	"occupied"		"empty"		
ℓ	DOM	CDBonn	DOM	CDBonn	Ratio
0	3.60	3.56	0.14	0.05	2.8
1	5.48	5.41	0.69	0.20	3.5
2	8.88	9.13	0.68	0.18	3.8
3			1.93	0.45	4.3

6.2.2 Quasiholes and quasiparticles

The quasihole energies are shown in Table 6.3. They were obtained by solving Eq. (6.12) but disregarding the imaginary part. The results for the static contribution of the self-energy (labeled by BHF in the table) are also included. Comparison of these results with the full calculation shows that the inclusion of the dispersive contribution moves the $0s_{1/2}$ state up by almost 13 MeV. The cause of this huge shift must be attributed to the strong energy dependence of the diagram (c) in Fig. 6.1 which is very repulsive at the solution of the $0s_{1/2}$ eigenvalue. For other quasihole energies substantially smaller corrections of both signs are obtained. While not including the imaginary part of the self-energy does not yield the correct normalization for the $0s_{1/2}$ state, the energy in the table is consistent with the location of the corresponding peak in Fig. 6.3. Results for the DOM self-energy employed in Ref. [30] are also included in the table as well as the experimental location of the sp orbits near the Fermi energy.

The particle-hole gap of the CDBonn self-energy is more than 10 MeV, substantially larger than for the DOM at 6.1 MeV which is a little below the experimental result of 6.8 MeV. A common issue with microscopic self-energies is the underestimate of the spin-orbit splitting near the Fermi energy. For example, the splitting of the d-states below the Fermi energy is only 4 MeV. In comparison, the experimental splitting is 6.7 MeV, and the DOM generates 5.7 MeV for this quantity. Relativistic effects and core polarization [104] or the importance of three-body forces [105] are usually

Table 6.3: Quasihole energies for neutron orbits in ^{40}Ca. The second column shows the results from using the Hartree-Fock part only and third column the results from including the 2p1h and 2h1p terms in the self-energy. We also include DOM results and the position of the experimental sp levels near the Fermi energy. Published in Ref. [33].

orbit	BHF [MeV]	Full [MeV]	DOM [MeV]	Exp. [MeV]
$0s_{1/2}$	-56.1	-43.6	-56.1	
$0p_{3/2}$	-37.4	-33.9	-39.6	
$0p_{1/2}$	-34.7	-31.7	-34.9	
$0d_{5/2}$	-20.4	-21.8	-21.6	-22.3
$1s_{1/2}$	-18.1	-19.6	-17.4	-18.3
$0d_{3/2}$	-16.0	-17.8	-15.9	-15.6
$0f_{7/2}$	-4.3	-7.1	-9.8	-8.4
$1p_{3/2}$	-2.6	-5.1	-7.0	-5.9
$1p_{1/2}$	-1.2	-3.5	-5.4	-4.2

invoked to repair this discrepancy but it should be noted that the fragmentation of sp strength makes the determination of the spin-orbit splitting more ambiguous.

The spectroscopic factors identify the amount of sp strength residing near the Fermi energy and together with occupation numbers are shown in Table 6.4 for the quasiparticle and quasihole states. The spectroscopic factors are calculated according to Eq. (6.14) after solving the Dyson equation (6.12). Occupation numbers for the

Table 6.4: Quasihole (quasiparticle) spectroscopic factors and occupation numbers for the CDBonn (CDB) self-energy compared to the corresponding DOM results. Published in Ref. [33].

orbit	S_{CDB}	S_{DOM}	n_{CDB}	n_{DOM}
$1s_{1/2}$	0.85	0.66	0.91	0.88
$0d_{3/2}$	0.87	0.64	0.92	0.86
$0f_{7/2}$	0.92	0.67	0.02	0.11
$1p_{3/2}$	0.93	0.69	0.02	0.07
$1p_{1/2}$	0.93	0.73	0.02	0.06

quasiparticle or quasihole orbits are obtained by twice folding the momentum space wave function with the one-body density matrix in momentum space, which is given in Eq. (6.22). For the hole states near ε_F there is a reduction of sp strength of a little more than 10% for the CDBonn calculation. This reduction is associated mostly with the effect of SRC. For the particle states, the reduction of the sp strength corresponds to about 10%. It was observed in Ref. [30] that the spectroscopic factors calculated for orbits in the continuum are not reliable (and can be larger than 1) so these are not included in the table.

All CDBonn spectroscopic factors are about 20% larger than in the DOM calculation, which yields spectroscopic factors that are in good agreement with the analysis of the $(e, e'p)$ reaction on ^{40}Ca [106]. Since the DOM includes the coupling to low-lying excitations associated with collective effects of the nuclear surface, this larger reduction simply reflects the important role of LRC. The difference in occupation numbers is less dramatic partially because the strength removed from the quasihole (particle) peaks to lower energy due to LRC in the DOM is recovered when performing the energy integration over the spectral function to obtain the occupation number [24].

6.2.3 Momentum Distribution

The total momentum distribution for neutrons in ^{40}Ca resulting from the CDBonn interaction and calculated according to the equivalent of Eq. (6.18) is shown in Fig. 6.4 by the solid line. All distributions are multiplied by k^2 and normalized such that $4\pi \int dk\ k^2 n(k) = 1$.

The quasihole contribution without the reduction due to spectroscopic factors is shown by the dashed line. Comparison of the full distribution with this mean-field-like contribution (dashed) shows that the many-body wavefunction contains an appreciable presence of high-momentum components.

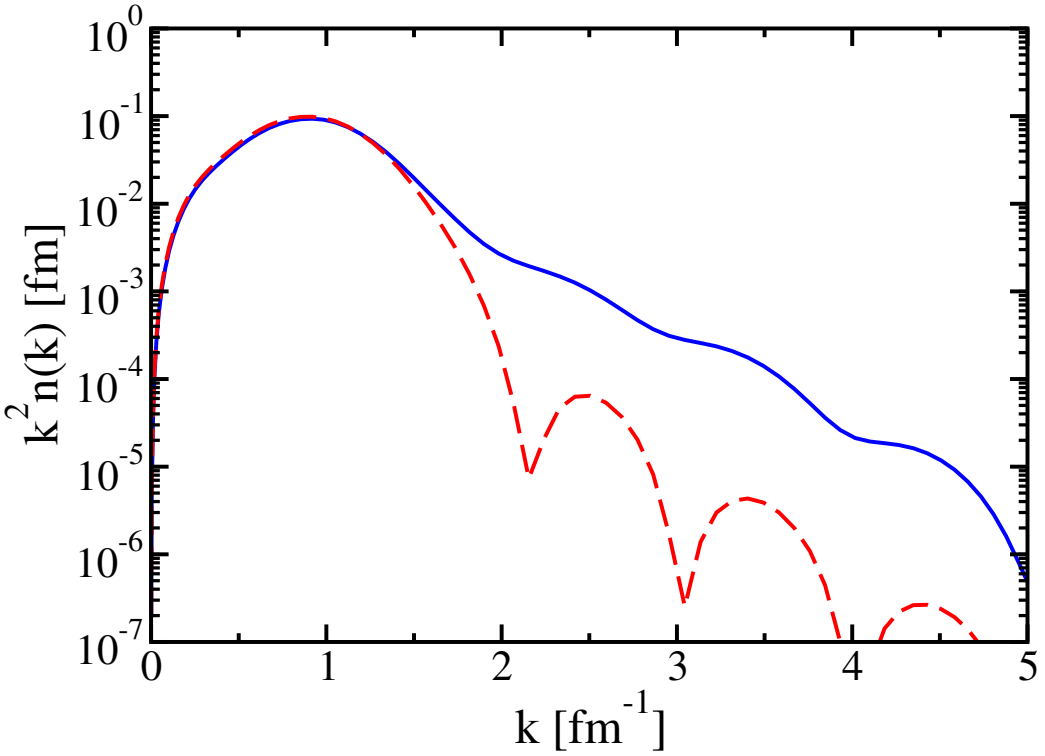

Figure 6.4: Momentum distribution for neutrons in ^{40}Ca weighted by k^2. Solid line represents the total momentum distribution including quasihole and continuum terms. The dashed line represents the quasihole result without reductions from spectroscopic factors. Published in Ref. [33].

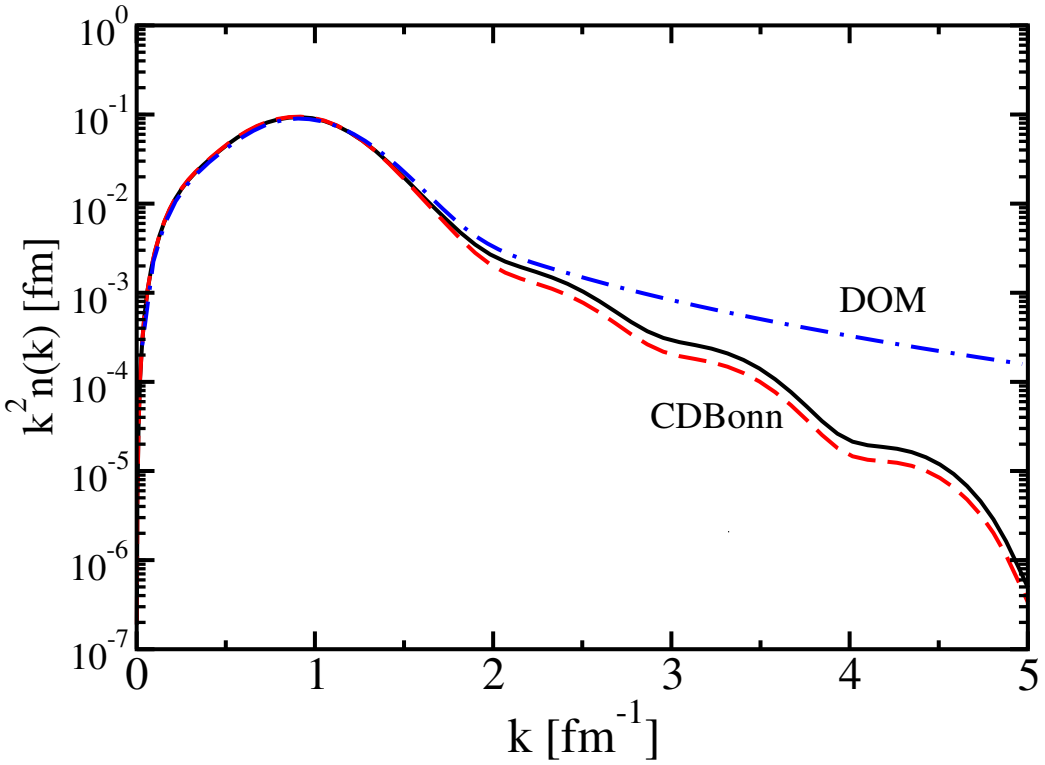

Figure 6.5: CDBonn momentum distribution with $\ell_{max} = 3$ (dashed) and $\ell_{max} = 4$ (solid) compared with the DOM result including all partial waves including $f_{7/2}$ (dash-dot) as obtained in Ref. [30]. The normalization of the curves is given by $4\pi \int dk\ k^2 n(k) = 1$. Published in Ref. [33].

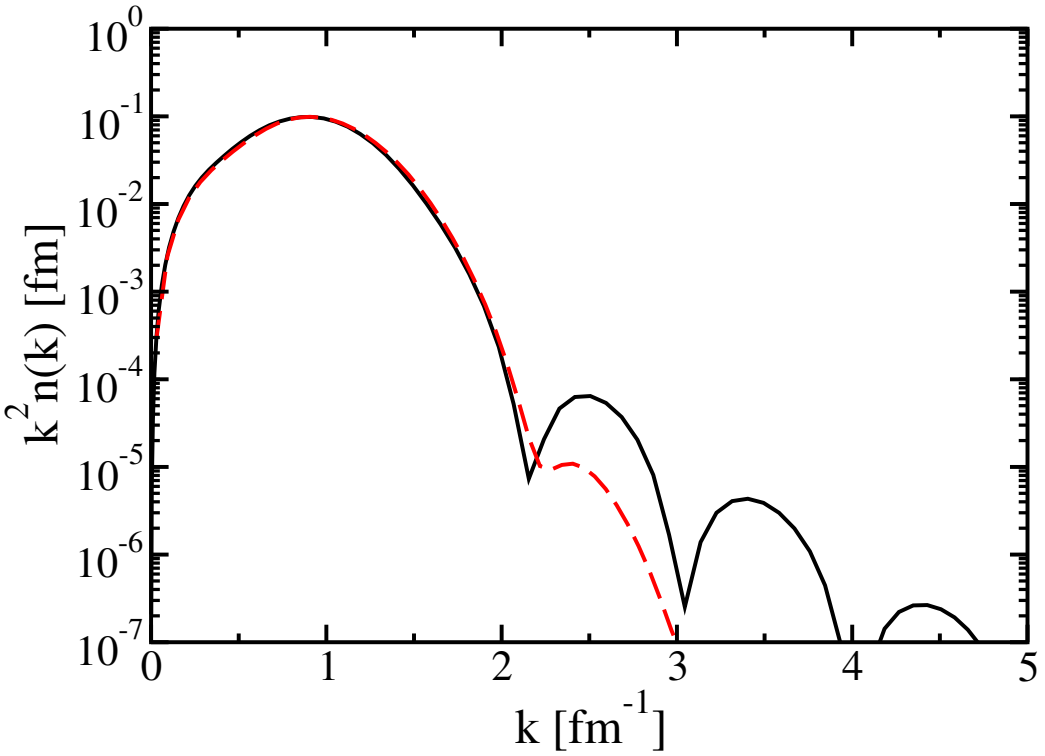

Figure 6.6: Quasihole contribution to the momentum distribution for the CDBonn (solid) compared to the DOM result (dashed). Both distributions are normalized according to $4\pi \int dk\ k^2 n(k) = 1$. Published in Ref. [33].

A comparison with the DOM result (dash-dot) in Fig. 6.5, normalized as in Fig. 6.4, indicates that the DOM self-energy has slightly more high-momentum components than the microscopic one, although the latter has a larger quasihole contribution at high-momentum, as shown Fig. 6.6. The amount of strength above 1.4 fm^{-1} corresponds to 8% for the CDBonn calculation compared to 10% for the DOM.

The convergence of the CDBonn result with orbital angular momentum is also illustrated in Fig. 6.5 exhibiting a satisfactory convergence when the $\ell_{max} = 3$ result (dashed) is compared with the one for $\ell_{max} = 4$ (solid). The convergence is not as good for the DOM result [30], which contains contributions from partial waves only up to and including $\ell = 3$. These results further confirm the importance of a nonlocal representation of the imaginary part of the self-energy which automatically leads to a better convergence with orbital angular momentum.

As discussed in Sec. 6.2.1, the energy dependence of the spectral function of the CDBonn potential in momentum space already suggests that it is a rather soft potential in comparison with the Bonn-B potential [102] that was employed for ^{16}O in Refs. [7, 50, 51]. While the spectroscopic factors for the aforementioned Bonn potentials in these nuclei are similar, the CDBonn potential contains about 4% of strength in the quasihole orbits above 1.4 fm^{-1}, whereas for the Bonn-B potential this amount is much smaller. It would be interesting in the future to investigate the corresponding behavior of a harder and local interaction such as Argonne $V18$ [90].

6.2.4 Natural Orbits

Calculations of natural orbits yield useful information concerning correlations in many-fermion systems, since these orbits exhibit the largest possible occupation numbers for a given ℓj-combination [107]. In the IPM model and the naive shell model the largest occupation is 1 and the natural orbits are then the same as the quasihole wave functions. The amount of deviation from 1 for the states that are fully occupied in the IPM and from 0 for the states that are empty in the IPM is therefore a useful

measure of the relevance of correlations beyond the mean field. Results for natural orbits are obtained by diagonalizing the one-body density matrix, which leads to Eq. (6.23). The resulting natural orbit functions carry information about sp strength located at different energies, whereas quasihole wave functions show the sp strength at a single energy.

Some of the natural orbit functions from the CDBonn density matrix are shown in Figs. 6.7-6.9 in momentum space. In Fig. 6.7 the natural orbit for the $s_{1/2}$ partial wave without a node (corresponding to an occupation of 0.882) is compared with corresponding deeply-bound quasihole (solid) wave function. The natural orbit wave function extends farther out in momentum space reflecting the contribution from lower energies that contain higher momenta. Both wave functions are normalized to unity. In Fig. 6.8 the natural orbit wave function for the $s_{1/2}$ partial wave with one node is compared with the quasihole wave function of the $s_{1/2}$ state near the Fermi energy (solid). Again there is a substantial difference between the two wave functions. The quasihole wave function has a spectroscopic factor of 0.85, while the natural orbit occupation is 0.910. Evidently, most of the $s_{1/2}$ strength with one node in addition to the quasihole strength is concentrated at low momenta, in contrast to the case with no node.

Contrary to the two $s_{1/2}$ results, the $d_{3/2}$ quasihole and natural orbit wave functions are essentially indistinguishable, as shown in Fig. 6.9. A similar result was obtained (in coordinate space) for the DOM calculation of Ref. [30]. This similarity may be due to the presence of only one natural orbit with a large occupation number unlike the $s_{1/2}$ case, although in the DOM calculation of Ref. [30] both quasihole $s_{1/2}$ wave functions were essentially identical to the natural orbit results.

Occupation numbers for natural orbits are shown in Table 6.5 for relevant partial waves. The s and p orbits with $n = 1$ (no node) have somewhat smaller occupations than the corresponding orbits for ^{16}O [51]. This is somewhat unexpected since the effect of SRC for the CDBonn self-energy is slightly weaker than for the one in Ref. [51]. However, the orbits with higher n have more occupation than in Ref. [51].

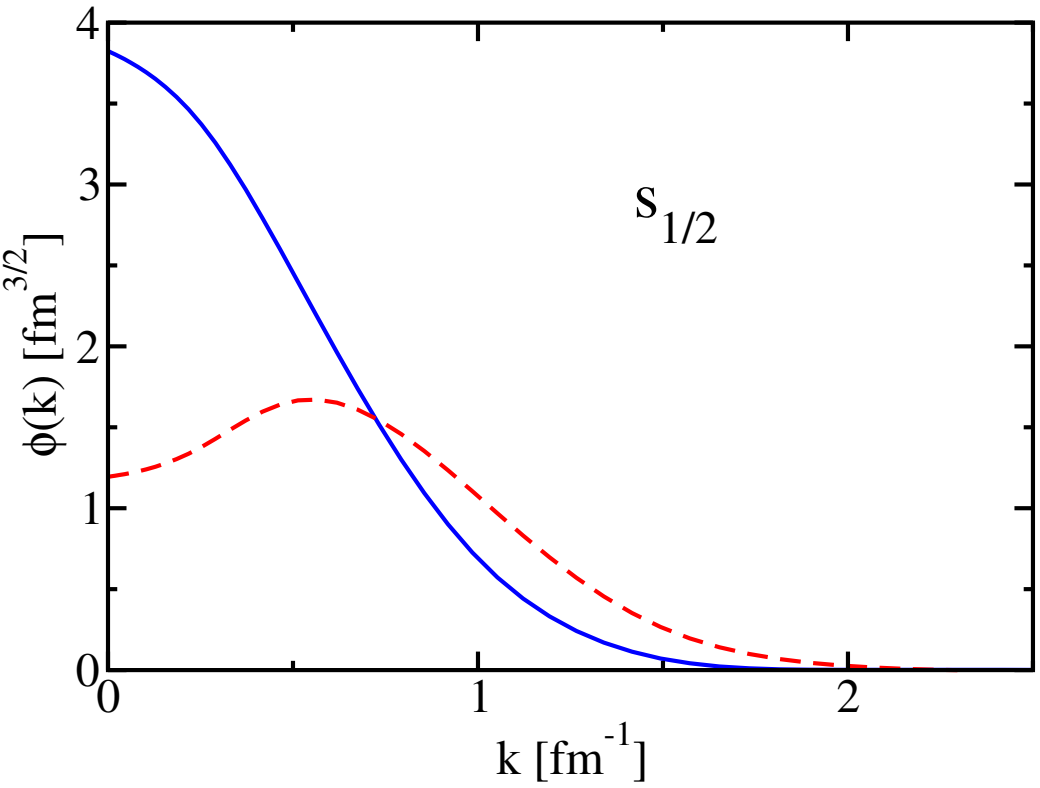

Figure 6.7: Comparison of wave functions for the $s_{1/2}$ quasihole result (solid) and the corresponding natural orbit (dashed) without a node. Published in Ref. [33].

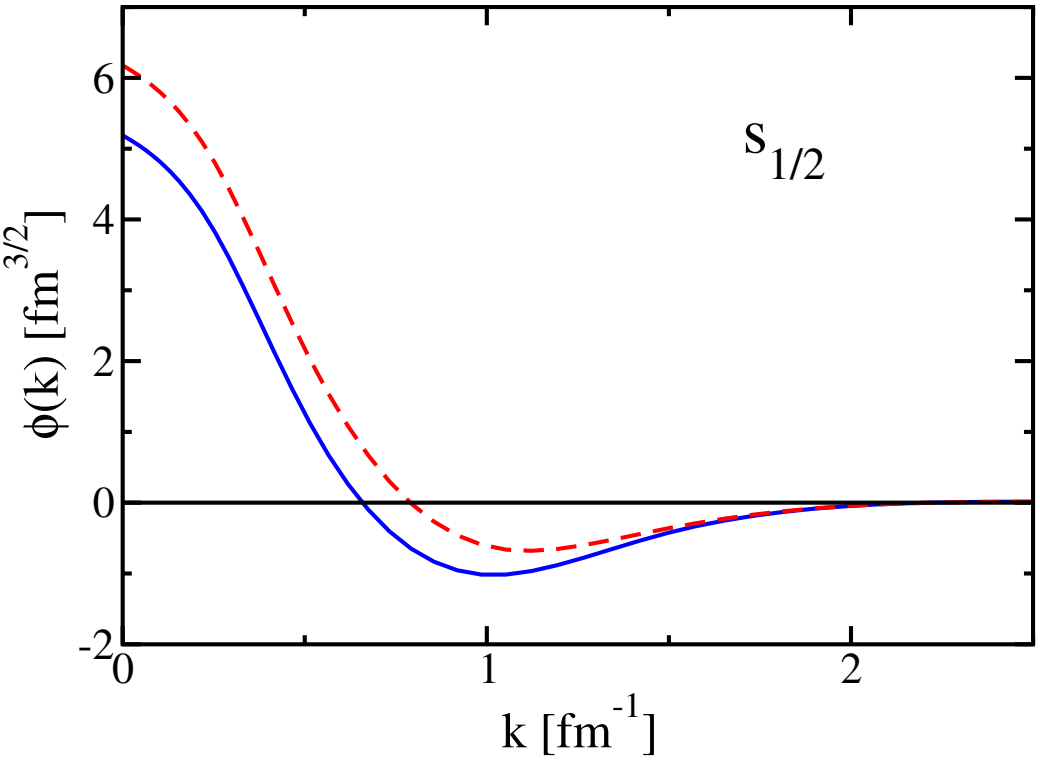

Figure 6.8: As in Fig. 6.7 but showing $s_{1/2}$ wave functions with one node. Published in Ref. [33].

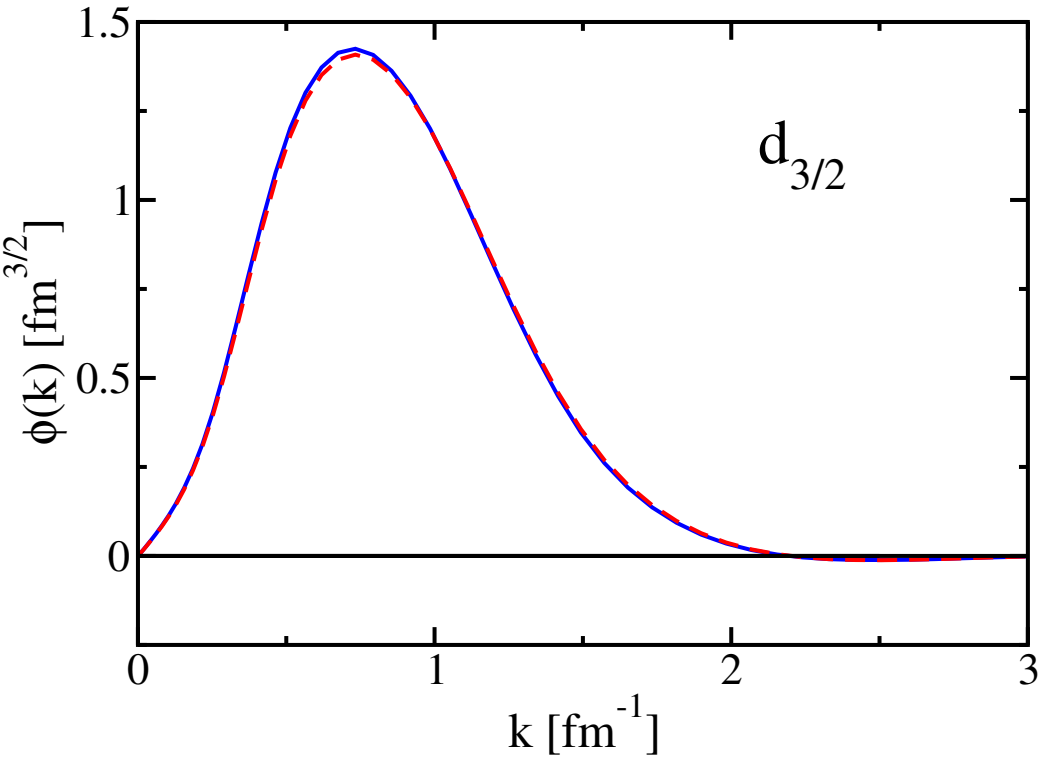

Figure 6.9: As in Fig. 6.7, but with the corresponding $d_{3/2}$ wave functions. Published in Ref. [33].

Table 6.5: Occupation numbers of natural orbits. Published in Ref. [33].

n	$s_{1/2}$	$p_{3/2}$	$p_{1/2}$	$d_{5/2}$	$d_{3/2}$	$f_{7/2}$	$f_{5/2}$
1	0.882	0.902	0.898	0.909	0.919	0.024	0.025
2	0.910	0.025	0.025	0.014	0.015	0.006	0.007
3	0.016	0.007	0.008	0.003	0.004	0.001	0.001
4	0.004	0.001	0.002	0.001	0.001	0.0003	0.0005
5	0.001	0.0004	0.0004	0.0001	0.0002	0.0001	0.0001
6	0.0002	0.0001	0.0001	0.0001	0.0001	$<$ 1e-4	$<$ 1 e-4
Σ_n	1.82	0.94	0.93	0.93	0.94	0.03	0.03

Table 6.6: Occupation numbers of natural orbits calculated with the DOM. Published in Ref. [30].

n	$s_{1/2}$	$p_{3/2}$	$p_{1/2}$	$d_{5/2}$	$d_{3/2}$	$f_{7/2}$	$f_{5/2}$
1	0.926	0.921	0.905	0.899	0.858	0.109	0.064
2	0.881	0.072	0.062	0.037	0.032	0.024	0.020
3	0.032	0.021	0.020	0.015	0.014	0.010	0.010
4	0.015	0.010	0.009	0.007	0.007	0.006	0.005
5	0.007	0.005	0.005	0.004	0.004	0.003	0.003
$\sum_n$	1.86	1.03	1.00	0.96	0.92	0.15	0.10

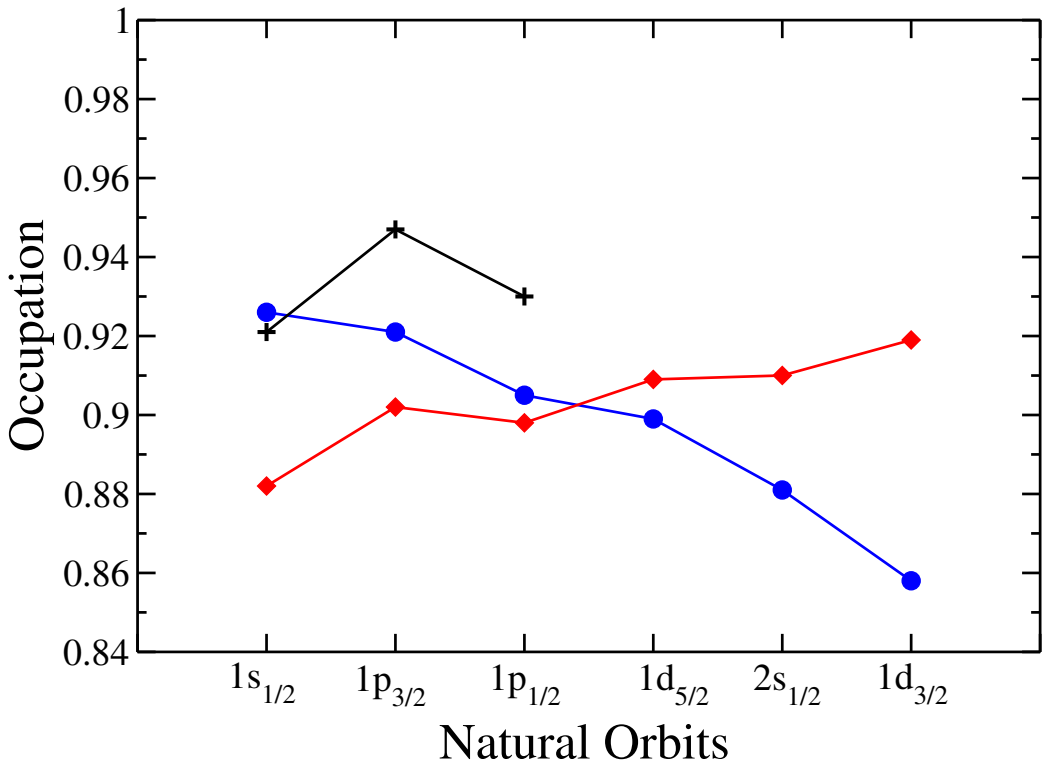

Figure 6.10: Occupation numbers of natural orbits that are fully occupied in the IPM. Results are shown for the CDBonn calculation (diamonds), the DOM calculation (circles), and the microscopic calculation done in Ref. [51] for ^{16}O (plusses).

The DOM results for ^{40}Ca are shown in Table 6.6 (see also Ref. [30]). It is interesting to look at the predominantly occupied orbits organized in the order of increasing energy in the BHF approach (which also gives a maximum occupation of 1). The occupation numbers of the natural orbits arranged in this way are shown in Fig. 6.10 (note that for the natural orbits $n = 1$ corresponds to no node).

Focusing on the CDBonn results (red diamonds) one can see that the inclusion of correlations has a greater effect on the deeply-bound quasihole states. The occupation number increases from 0.882 for the $1s_{1/2}$ natural orbit wave function to 0.919 for the $1d_{3/2}$ orbit. This trend makes physical sense, since SRC become more important at more negative energies, and is also consistent with Figs. 6.7 and 6.8, which show that the natural orbit $1s_{1/2}$ wave function samples more high-momenta than the $2s_{1/2}$ orbit. The occupations for ^{16}O from [51] are also shown in Fig. 6.10 (black plusses).

As already mentioned, they are higher than the CDBonn results, but they follow a similar pattern.

Interestingly, the DOM results (blue circles) show the opposite trend as the CD-Bonn results. Based on the analysis of the DOM spectral functions in k-space in Ch. 3, it would appear that the various ℓj-channels have similar high-momenta content, producing an overall reduction that is independent of energy. The negative slope seen in Fig. 6.10 would then correspond to the effect of LRC, which become less important at more negative energies.

Another interesting thing to note in comparing Tables 6.5 and 6.6 is that the DOM occupation numbers of the predominantly empty orbits are, in general, larger than the CDBonn occupation numbers. This larger occupation is due to the inclusion of LRC in the DOM.

A comparison with natural orbits obtained for finite drops of ^{3}He atoms [108] illustrates the substantial difference between the underlying fermion-fermion interactions. The atom-atom interaction is much more repulsive and has a longer range, and these features lead to occupation numbers as small as 0.54 for the $1s$ state in a drop of 70 ^{3}He atoms. In contrast, the nuclear interaction generates values close to 0.9 in both the DOM and the CDBonn calculations. The difference is therefore mostly related to the much stronger repulsion between ^{3}He atoms which *e.g.* in the liquid at saturation leads to a depletion of the Fermi sea of more than 50% [109]. Nucleon-nucleon interactions typically generate 10-15% depletion due to SRC [96].

6.2.5 Charge Distribution

Although this chapter has focused mainly on neutron results for ^{40}Ca, it is useful to study the charge density distribution obtained for the CDBonn potential. For this purpose, the Coulomb potential was incorporated into the calculations by first transforming the irreducible self-energy to coordinate space. The Coulomb potential from a uniformly charged sphere was then added, and a matrix inversion was performed to

get the propagator as discussed in Ch. 3. The radius of the sphere was taken to be $R_C = 1.31A^{1/3}$, following the DOM analysis. The final charge distribution is shown by the dashed line in Fig. 6.11 and compared to the experimental one obtained from the Fourier-Bessel analysis of Ref. [48].

The mean square radius of the CDBonn distribution is 3.29 fm compared to the experimental result of 3.45 fm taken from Ref. [48]. Microscopic calculations usually underestimate the experimental results (see *e.g.* Ref. [7] for ^{16}O). Adequately incorporating LRC may improve the charge density. A recent microscopic calculation of the matter density in ^{40}Ca also concentrates too much matter near the origin [110] pointing to the importance of comparing many-body calculations with as many experimental quantities as possible for a more detailed understanding of their quality.

The DOM charge density also contains too much charge near the origin [30] even though LRC were incorporated, and the DOM self-energy was constrained to reproduce the mean-square-radius of the charge distribution. It appears therefore that a proper inclusion of SRC, LRC, and nonlocality are all essential for obtaining a charge density that is in better agreement with the data.

6.2.6 Ground-state Energy

From the momentum distribution and the spectral function in k-space, the neutron contribution to the ground state energy per neutron can be calculated by using:

$$\frac{E_n(^{40}\mathrm{Ca})}{N_{calc}} = \frac{1}{2N_{calc}} \sum_{\ell j} (2j+1) \int dk k^2 \frac{\hbar^2 k^2}{2m} n_{\ell j}(k) + \frac{1}{2N_{calc}} \sum_{\ell j} (2j+1) \int dk k^2 \int_{-\infty}^{\varepsilon_F} dE \; E \; S_{\ell j}(k;E), \tag{6.25}$$

where E_n is the total energy from the neutrons, and N_{calc} [see Eq. (6.24)] is the calculated number of neutrons when all partial waves with $\ell \leq 4$ are included. With this limit on the number of partial waves $N_{calc} = 19.3$, the energy per neutron is –8.25 MeV.

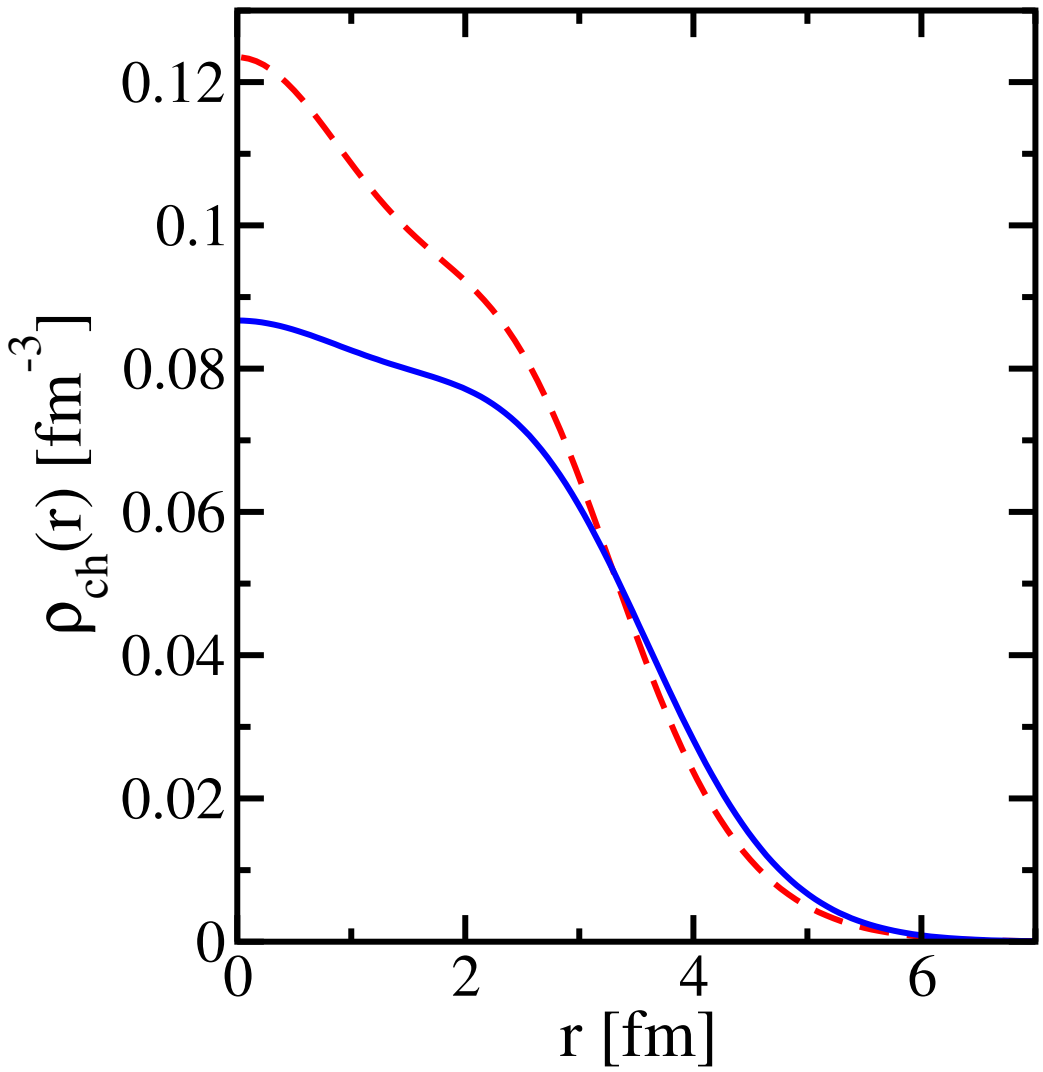

Figure 6.11: Charge density distribution for ^{40}Ca from the CDBonn self-energy (dashed) compared to experiment (solid). Published in Ref. [33].

The energy for the protons was generated in coordinate space, following the same procedure as for the charge distribution calculation. The density matrix and spectral function were then transformed back to momentum space in order to use Eq. (6.25) with E_n replaced by E_p and N_{calc} by the calculated proton number Z_{calc}, which was found to be $Z_{calc} = 19.5$. The resulting energy per proton is –4.91 MeV, and the resulting total energy per particle is $E(^{40}\mathrm{Ca})/A$ = –6.56 MeV. This result is 1.85 MeV per particle more attractive than the DOM result in Ch. 3 (also Ref. [30]), but still more than 2 MeV/A higher than the experimental binding of –8.55 MeV/A. From the results of the spectral functions it is clear that the CDBonn calculations generate more strength in the continuum at very negative energies than in the DOM calculation, demonstrating the importance of these continuum contributions to the total energy.

This importance was also recognized in Ref. [7], where it was shown that the continuum accounts for about two-thirds of the binding even though it represents only about 10% of the particles. Since the CDBonn calculation employed in this chapter involves a different interaction and is for a heavier nucleus, it is instructive to quantify the role of the continuum as compared with what was found in Ref. [7]. The quasihole contributions to the energy of the ground state are well separated from the continuum except for the peak corresponding to the lowest $s_{1/2}$ orbit as shown in Fig. 6.3. The $s_{1/2}$ continuum contribution, then, was assessed by integrating the strength in Eq. (6.25) up to –50 MeV. The total binding from the continuum contributions of all partial waves was found to be –105.88 MeV compared to a total of –159.16. Thus, binding due to the continuum represents 67% of the total binding, and is a very similar result to the ^{16}O calculations of Ref. [7]. It should be mentioned that even though the CDBonn interaction is relatively soft, the cancellation between kinetic energy (419.15 MeV) and potential energy (–578.32 MeV) is quite substantial.

Recent calculations for ^{40}Ca employing the unitary-model-operator approach generate –8.51/A, also using the CDBonn interaction [111]. This result is close to the experimental value. The present calculation of –6.56 MeV/A is almost 2 MeV per par-

ticle less, pointing to the need of additional correlations and an improved treatment of the propagators included in the present self-energy calculation. Only noninteracting propagators were used in the construction of the self-energy and self-consistency was not attempted. The proper treatment of LRC may also be relevant in this case. The FRPA method does not explicitly include high-momentum components so a combination of the current method and the FRPA needs to be developed.

6.2.7 Analysis of CDBonn self-energy

Improving the analysis of elastic scattering data above the Fermi energy and observables related to quantities below the Fermi energy in a DOM framework appears to depend sensitively on the treatment of nonlocality in the imaginary part of the self-energy. Therefore, as in the case of the FRPA analysis in Ch. 5, the properties of the present microscopic self-energy are explored in more detail, in order to see if they may offer guidance on how to implement nonlocality in future DOM parametrizations. A few simple fits were performed to represent the central part of the imaginary part of the CDBonn self-energy in coordinate space at a given energy assuming the same form for the potential given in Ch. 5. In practice, this means that only the $\ell = 0$ self-energy needs to be represented in terms of Eq. (5.16). If the choice of Eq. (5.16) is appropriate, the other ℓ-values will be adequately represented as well.

A fit of the imaginary part at 65 MeV was done partly because it was expected that only at such energies the imaginary part of the microscopic self-energy has real relevance since the role of LRC is expected to be diminished. Figure 6.12 displays the diagonal of the central imaginary part of the self-energy in coordinate space for $\ell = 0$ for the CDBonn potential by the solid line. The fit according to Eq. (5.16) is quite satisfactory and given by the dashed line. Quantitative results for diffuseness a_0, radius r_0, and the nonlocality parameter β are discussed below.

Another useful check on the overall relevance of the parametrization of the nonlocal content of the potential is to integrate over the variable r' in Eq. (5.16) to sample

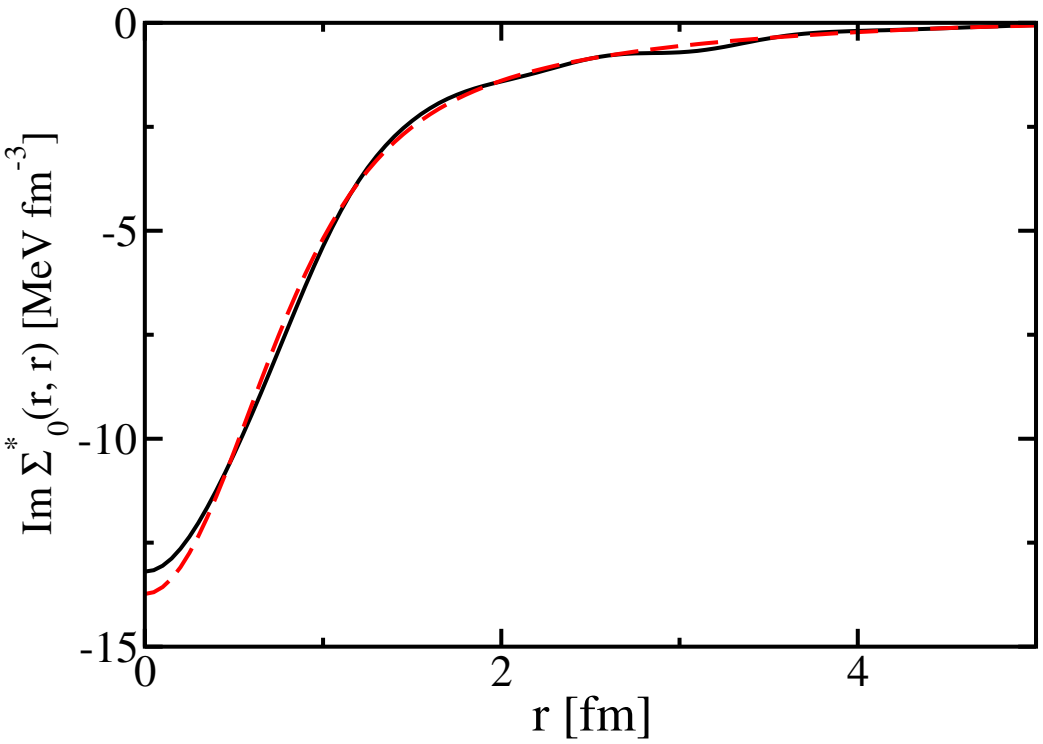

Figure 6.12: Diagonal part of CDBonn imaginary self-energy at 65 MeV (solid), and the corresponding parametrized self-energy (dashed). The results shown are for $\ell = 0$. Published in Ref. [33].

the nondiagonal components and compare with the corresponding integral for the CDBonn self-energy. The result of this procedure is identified by Σ^*_{int} and shown in Fig. 6.13 as a function of r for the parametrization (dashed) and CDBonn self-energy (solid) for orbital angular momentum $\ell = 0$.

This more stringent test including the sampling of non-diagonal components of the self-energy, still yields a satisfactory representation of the microscopic potential. It is interesting to note that the shape of the "local" potential is more reminiscent of a standard volume absorption.

As was seen in Ch. 5, another useful quantity to gauge the characteristic of an absorptive potential is the volume integral. For local potentials this quantity is well-constrained by experimental cross sections [23, 24]. As in Ch. 5 the volume integral

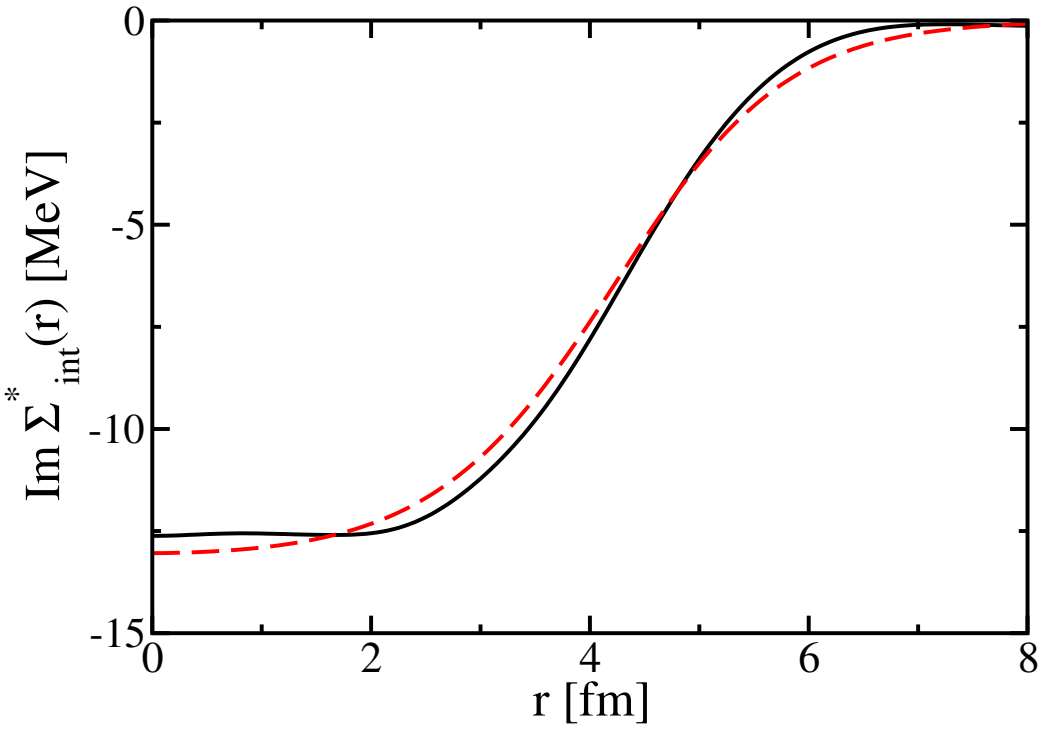

Figure 6.13: CDBonn imaginary self-energy at 65 MeV integrated over r' (solid), and the corresponding integrated parametrized self-energy (dashed). The results shown are for $\ell = 0$. Published in Ref. [33].

for a given orbital angular momentum ℓ is defined by

$$J_W^\ell(E) = 4\pi \int dr\ r^2 \int dr' r'^2\ \mathrm{Im}\ \Sigma_\ell^*(r, r'; E). \tag{6.26}$$

For a local potential it reduces to the standard definition of the volume integral.

The implied ℓ-dependence of the chosen nonlocal potential leads to predictions for higher ℓ-values for this quantity once a fit to the $\ell = 0$ component of the self-energy has been made. The result of the corresponding volume integrals per nucleon are shown in Fig. 6.14 as a function of the ℓ-values considered for the CDBonn self-energy. The agreement between the CDBonn results (dots) and the predictions based on Eq. (5.16) appears very satisfactory and may be useful to extract the properties of the CDBonn self-energy for even higher ℓ-values without recourse to an explicit calculation.

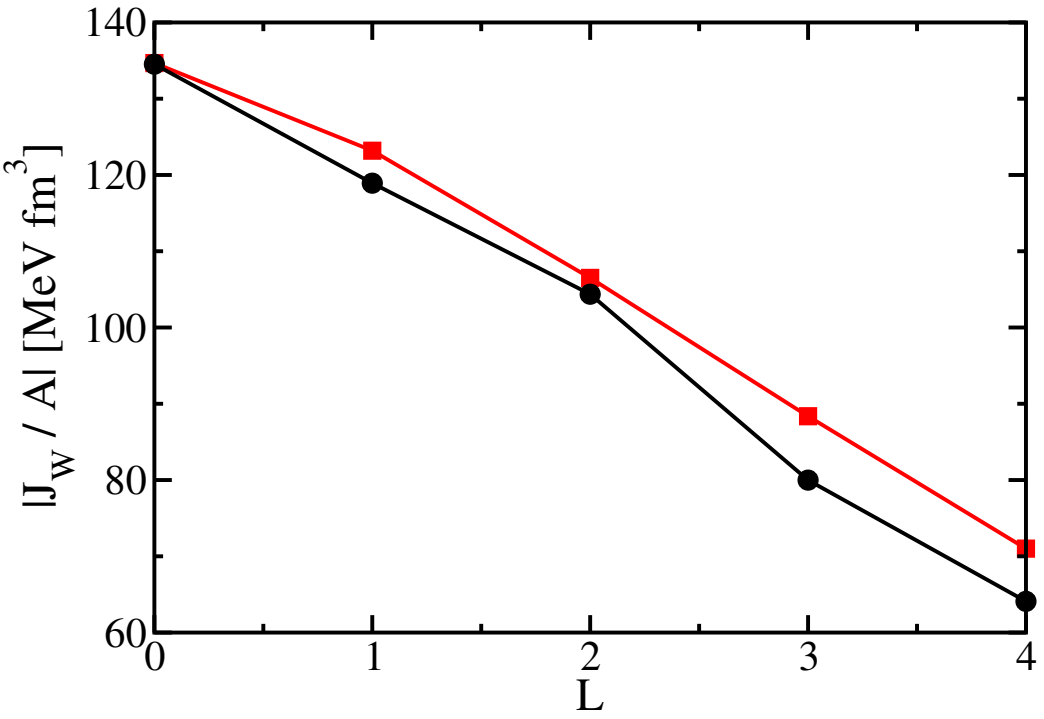

Figure 6.14: Imaginary volume integrals for the CDBonn self-energy at 65 MeV (circles), and the corresponding result for the parametrized self-energy (squares). Published in Ref. [33].

The properties of the imaginary part of the CDBonn self-energy in terms of its nonlocality content are summarized in Table 6.7 for four different energies, one below and three above the Fermi energy. In all cases a substantial imaginary part of the CDBonn self-energy is present at the chosen energies. The parameters are fitted at each energy to reproduce the essential properties of the self-energy including the volume integral for $\ell = 0$, as discussed above for the case of 65 MeV.

The fits to the self-energy at the higher energies generate standard values for the diffuseness, but the fits for 49 and -76 MeV generate substantially larger values. The radius parameter is quite small below the Fermi energy but yields rather standard values at positive energy. The value of the nonlocality parameter is quite a bit larger than typically assumed for real nonlocal potentials. Wave function corrections for nonlocality in the analysis of $(e, e'p)$ reactions typically assume values of $\beta = 0.85$ fm [2]. The DOM analysis of Ref. [30] (also discussed in Ch. 3) yielded a value

Table 6.7: Parameters from nonlocal fits to the imaginary part of the proton self-energy at different energies. W_0 is in MeV, r_0, a_0, β are in fm, and J_W is in units of MeV fm^3. Published in Ref. [33].

Energy MeV	W_0 MeV	r_0 fm	a_0 fm	β fm	$\lvert J_W/A\rvert$	$\lvert J_W/A\rvert$ [CDBonn]
-76	36.30	0.90	0.90	1.33	193	193
49	6.51	1.25	0.91	1.43	73	73
65	13.21	1.27	0.70	1.29	135	135
81	23.90	1.22	0.67	1.21	215	215

of 0.91 fm.

The nonlocality parameter decreases with increasing energy, suggesting a trend to a more localized potential. Since for a local potential there is no ℓ-dependence of the volume integral, the behavior of J_W^ℓ was investigated for different ℓ-values in a wide energy domain. The results of this analysis are shown in Fig. 6.15.

The degree of nonlocality appears to be largest below the Fermi energy with a substantial separation between the different ℓ-values. The result for $\ell = 0$ also demonstrates that it is possible to have the "wrong" sign for the volume integral. This can happen because the microscopic self-energy develops negative lobes off the diagonal and a positive volume integral cannot be guaranteed as a result, as must be the case for a local potential. Although the imaginary part above the Fermi energy is negative, it is conventional to plot the imaginary volume integral as a positive function of energy [22, 24]. At positive energy the volume integrals for different ℓ at first exhibit a spread although not as large as below the Fermi energy. Above 300 MeV however, the curves apparently become similar suggesting a trend to a more local self-energy.

Before concluding, it should be noted that quantities related to scattering were also calculated with the self-energy discussed in this chapter. The reader is referred to Ref. [33] for more details.

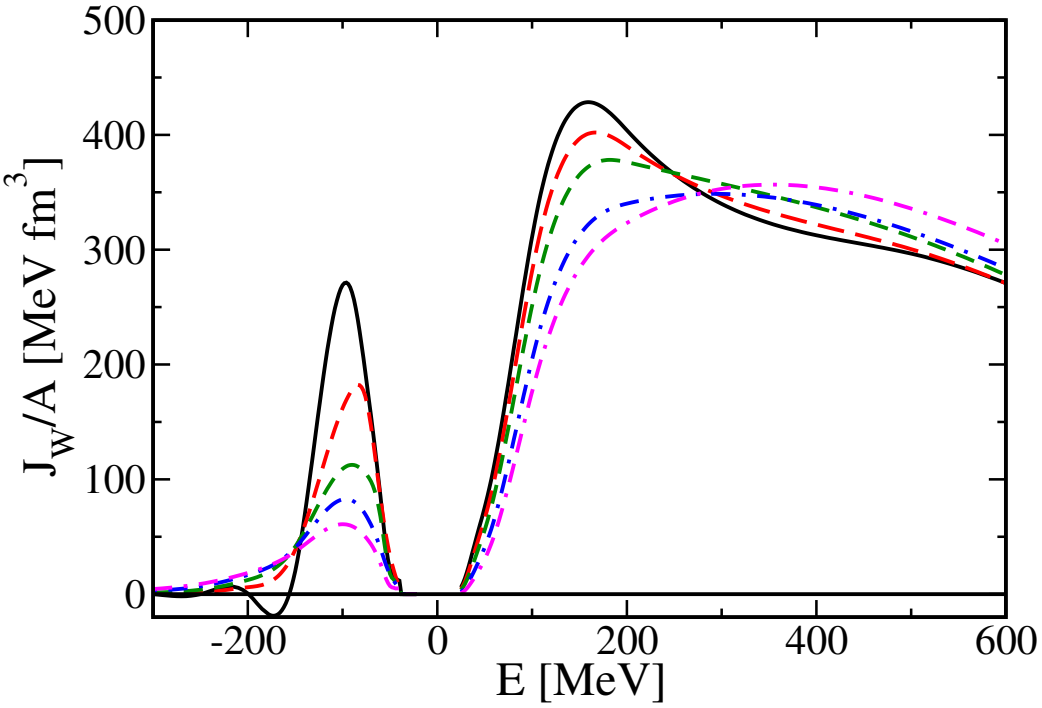

Figure 6.15: Imaginary volume integrals for the CDBonn self-energy as a function of energy for different ℓ-values: $\ell = 0$ (solid), $\ell = 1$ (dashed), $\ell = 2$ (short-dashed), $\ell = 3$ (dash-dot), and $\ell = 4$ (dash-dash-dot). Published in Ref. [33].

6.3 Conclusions

The properties of the microscopic self-energy of nucleons derived from the realistic CDBonn interaction have been studied for ^{40}Ca. The calculation involves a two-step procedure starting with the calculation of a $\mathcal{G}_{NM}$-matrix interaction in nuclear matter for a fixed energy and density. In a second step, the Fermi structure of the finite nucleus is incorporated by expanding the finite-nucleus $\mathcal{G}_{FN}$-matrix in the nuclear matter one, including up to second-order terms. The self-energy is obtained by including the corresponding self-energy terms with imaginary parts above and below the Fermi energy, with associated real parts obtained from the appropriate dispersion relations. The analysis of the solutions of the Dyson equation below the Fermi energy includes spectral functions calculated in momentum space, momentum distributions, quasihole properties (including spectroscopic factors), natural-orbit properties, the

nuclear charge density, and the energy of the ground state of ^{40}Ca. An important motivation for the present work is to generate insight from microscopic calculations what functional forms of the nucleon self-energy can be employed fruitfully in the analysis of experimental data in the DOM framework. Recent DOM work has also focused on ^{40}Ca.

Nucleon spectral functions for the CDBonn potential exhibit similar features as those from earlier work for ^{16}O using the Bonn-B potential although the former interaction appears somewhat softer. This leads to a less pronounced presence of high-momentum components at very negative energies. The energy distribution of these momenta is somewhat different than the one generated by the DOM self-energy although the fraction of high-momentum particles is about 10% in both calculations.

Since noninteracting intermediate states are employed in the CDBonn self-energy and therefore LRC are not well incorporated, there is no imaginary part in a substantial region around the Fermi energy. As a result, only the lowest $s_{1/2}$ state is broadened in accordance with experiment, whereas all other quasihole states are represented by discrete states. The DOM calculation exhibits a more realistic distribution of the sp strength including appropriate widths for p-states as well. The location of the quasihole states in the CDBonn calculation is in reasonable agreement with experiment but the particle-hole gap is larger than experiment. The associated spectroscopic factors are close to 0.9 consistent with the 10% fraction of high-momentum nucleons. The DOM spectroscopic factors are about 0.2 smaller since the DOM self-energy includes a strong coupling to the nuclear surface leading to better agreement with the analysis of $(e, e'p)$ reactions.

The calculation of natural orbits demonstrates that the largest occupation numbers are close to 0.9 very similar to a recent DOM calculation even though substantial differences in spectroscopic factors occur, as discussed above. It appears that nuclear natural orbits always generate such occupation numbers in contrast with finite drops of ^{3}He atoms, where they can be substantially smaller in accordance with the much stronger repulsion of the underlying interaction.

The nuclear charge density from the CDBonn self-energy exhibits too small a radius and too much charge at the origin but is otherwise not too dissimilar from the DOM results. Future work along these lines will have to include, for example, a better treatment of self-consistency as it is nowadays possible for nuclear matter calculations [96]. An important difference however, is the presence of a substantial nonlocal imaginary self-energy below the Fermi energy in the microscopic calculations. This leads to a good convergence with orbital angular momentum for the number of particles which amounts to 19.3 neutrons when $\ell_{max} = 4$. No such convergence is obtained with DOM calculations on account of the locality of the imaginary self-energy, thereby overestimating the number of particles. Thus, it seems that the introduction of nonlocality in the imaginary DOM potentials in the future is an essential ingredient that may also lead to a much better description of the nuclear charge density.

The distribution of high-momentum nucleons from the CDBonn calculation leads to their large contribution of 67% to the energy per particle in agreement with earlier observations for ^{16}O. The more realistic distribution of high-momenta leads to about 2 MeV more binding per nucleon than from the DOM self-energy while still underbinding by 2 MeV the experimental result, pointing to the need of an improved treatment of intermediate states in the self-energy and the consideration of higher-order contributions in the nuclear-matter $\mathcal{G}_{NM}$-matrix interaction.

Finally, an analysis of the nonlocality of the imaginary part to the CDBonn self-energy reveals that its main properties can be quite well represented by a gaussian nonlocality. Typical nonlocality parameters are somewhat larger than those found in the literature. Volume integrals indicate that nonlocality is very important below the Fermi energy. Above the Fermi energy, it is initially substantial but appears to weaken at higher energies.

Chapter 7

Summary and Outlook

The focus of this thesis has been to highlight the connection of the DOM with the irreducible nucleon self-energy from Green's function theory and to improve this connection. It was shown in Ch. 3 that the explicit treatment of nonlocality greatly improves the correspondence between the DOM potential and the nucleon self-energy. However, only the volume HF term was made nonlocal, and it was argued that making the imaginary part of the potential nonlocal would lead to further improvements, such as a better convergence of particle number.

Comparison with bound-state data, such as the charge distribution, particle number, and the energy per particle was quite fruitful. In particular, this comparison led to the conclusion that the DOM does not yet properly describe SRC. In order to provide a proper description of SRC, it may be necessary in the future to make the geometry of the potential dependent on energy, but this would be much more computationally expensive since the dispersion relation would have to be evaluated for each value of position.

Application of the DOM to (d, p) transfer reactions highlighted the ability of the DOM to describe nuclear structure and incorporate the effects of correlations near the nuclear surface. Overall, the DOM potentials generated angular distributions comparable to the CH89 global optical-potential, which is often used in the analysis of transfer reactions. However, the DOM potentials generated more realistic spectro-

scopic factors, which were more in line with $(e, e'p)$ results.

One motivation for improving the DOM potentials is to provide more reliable extrapolations to unstable nuclei. Based on results in Ch. 3, the DOM appears to be flexible enough to incorporate new physics that may appear in exotic nuclei. For example, the DOM appears capable of describing coupling to the continuum. In addition, using a DOM potential extrapolated to ^{132}Sn in an analysis of the $^{132}\mathrm{Sn}(d,p)^{133}\mathrm{Sn}$ transfer reaction produced an angular distribution consistent with the data.

Comparison of the DOM with microscopic calculations of the self-energy yielded a number of insights. For example, the FRPA self-energy exhibited a parity dependence that changes with increasing neutron number and is related to changing shell structure. In contrast, the DOM has no ℓ-dependence apart from the spin-orbit potential. The parity dependence is particularly pronounced in ^{40}Ca and may at least partially explain why elastic proton scattering on this nucleus at low energies is difficult to describe. Comparison with the FRPA also challenged the assumption made in the DOM that the absorption in the energy region near the Fermi energy is symmetric about the Fermi energy. The tensor force was also found to have a significant effect on the absorption.

Comparison with a finite $\mathcal{G}$-matrix calculation employing the CDBonn potential reinforced the conclusion in Ch. 3 that the DOM does not yet properly take into account SRC. More work needs to be done, though, in order to gain insight from this calculation on how to incorporate SRC in the DOM. Both the FRPA and the $\mathcal{G}$-matrix calculations emphasized the importance of the nonlocality of the imaginary potential.

A major goal of this thesis is to make steps toward establishing a good method for obtaining an empirical self-energy that can then be used to make reliable extrapolations to the limits of stability. The empirical self-energy must be able to describe both nuclear reactions and nuclear structure. Therefore, it is important to constrain the empirical self-energy with both scattering and bound-state data. Currently DOM potentials are not constrained well at negative energies. It was shown in this thesis

Table 7.1: Changes to the DOM that are expected to improve the description of data associated with negative energies.

Data to fit	Nonlocal HF (Ch. 3)	Nonlocal Im. (Ch. 5, 6)	Better SRC (Ch. 3, 6)
Charge distribution	Normalization	Charge at origin	Charge at origin
Particle number	Normalization	Convergence with ℓ	
Ground-state energy	Normalization		High momenta at more negative energies

that nonlocality is especially important for describing observables associated with ground-state properties and thus nuclear structure. Table 7.1 summarizes how incorporating nonlocality and an improved treatment of SRC are expected to improve the description of data associated with negative energies.

An important next step is to create an implementation of the DOM that uses truly nonlocal potentials for both the real and imaginary parts; furthermore, this implementation must be able to fit both scattering and bound-state data simultaneously. Work in the theory group here at Washington University is currently being done in this direction. Another important next step is to be able to include the tensor force, which has a significant effect on nuclear structure of rare isotopes. Plans for such a project are currently being set in place.

In conclusion, taking the relation of the dispersive optical model with the self-energy opens up the possibility of a method of obtaining an empirical self-energy that can readily incorporate feedback from both theory and experiment. This dynamic interaction with theory and experiment provides a way to systematically improve the description of the empirical self-energy; this, along with the importance of the dispersion relation in connecting nuclear reactions and nuclear structure suggests that the "Dispersive Self-energy Method" is an apt name for this approach.

Bibliography

[1] M. Goeppert-Mayer, *Phys. Rev.*, **75**, 1969 (1949).

[2] J. W. A. den Herder *et al.*, *Nucl. Phys.*, **A490**, 507 (1988).

[3] G. van der Steenhoven, *Nucl. Phys. A*, **527**, 17c (1991).

[4] E. N. M. Quint, Ph.D. thesis, NIKHEF, Amsterdam (1988).

[5] L. Lapikás, *Nucl. Phys.*, **A553**, 297c (1993).

[6] G. J. Kramer, H. P. Blok and L. Lapikás, *Nucl. Phys.*, **A679**, 267 (2001).

[7] H. Müther, A. Polls and W. H. Dickhoff, *Phys. Rev. C*, **51**, 3040 (1995).

[8] W. H. Dickhoff and C. Barbieri, *Prog. Part. Nucl. Phys.*, **52**, 377 (2004).

[9] C. Barbieri, *Phys. Rev. Lett.*, **103**, 202502 (2009).

[10] P. G. Hansen and J. A. Tostevin, *Annu. Rev. Nucl. Part. Sci.*, **53**, 219 (2003).

[11] A. Gade and T. Glasmacher, *Prog. Part. Nucl. Phys.*, **60**, 161 (2008).

[12] I. Tanihata *et al.*, *Phys. Rev. Lett.*, **55**, 2676 (1985).

[13] E. Becheva *et al.*, *Phys. Rev. Lett.*, **96**, 012501 (2006).

[14] Brookhaven National Laboratory , Chart of nuclides, `http://www.nndc.bnl.gov/chart/reColor.jsp?newColor=sn` (2011).

[15] F. D. Becchetti Jr. and G. W. Greenlees, *Phys. Rev.*, **182**, 1190 (1969).

[16] R. L. Varner *et al.*, *Phys. Rep.*, **201**, 57 (1991).

[17] A. J. Koning and J. P. Delaroche, *Nucl. Phys. A*, **713**, 231 (2003).

[18] R. C. Johnson, *AIP Conf. Conf. Procs.*, **79**, 128 (2005).

[19] N. B. Nguyen, F. M. Nunes and R. C. Johnson, *Phys. Rev. C*, **82**, 014611 (2010).

[20] K. L. Jones *et al.*, *Phys. Rev. C*, **84**, 034601 (2011).

[21] C. Mahaux and R. Sartor, *Phys. Rev. Lett.*, **57**, 3015 (1986).

[22] C. Mahaux and R. Sartor, *Adv. Nucl. Phys.*, **20**, 1 (1991).

[23] R. J. Charity, J. M. Mueller, L. G. Sobotka and W. H. Dickhoff, *Phys. Rev. C*, **76**, 044314 (2007).

[24] J. M. Mueller, R. J. Charity, R. Shane, L. G. Sobotka, S. J. Waldecker, W. H. Dickhoff, A. S. Crowell, J. H. Esterline, B. Fallin, C. R. Howell, C. Westerfeldt, M. Youngs, B. J. Crowe, III and R. S. Pedroni, *Phys. Rev. C*, **83**, 064605 (2011).

[25] R. J. Charity, L. G. Sobotka and W. H. Dickhoff, *Phys. Rev. Lett.*, **97**, 162503 (2006).

[26] J. S. Bell and E. J. Squires, *Phys. Rev. Lett.*, **3**, 96 (1959).

[27] H. Feshbach, *Ann. Phys.*, **5**, 357 (1958).

[28] H. Feshbach, *Ann. Phys.*, **19**, 287 (1962).

[29] J. Amos *et al.*, *Adv. Nucl. Phys.*, **25**, 275 (2000).

[30] W. H. Dickhoff, D. Van Neck, S. J. Waldecker, R. J. Charity and L. G. Sobotka, *Phys. Rev. C*, **82**, 054306 (2010).

[31] N. B. Nguyen *et al.*, *Phys. Rev. C*, **84**, 044611 (2011).

[32] S. J. Waldecker, C. Barbieri and W. H. Dickhoff, *Phys. Rev. C*, **84**, 034616 (2011).

[33] H. Dussan, S. J. Waldecker, W. H. Dickhoff, H. Müther and A. Polls, *Phys. Rev. C*, **84**, 044319 (2011).

[34] S. C. Pieper and R. B. Wiringa, *Ann. Rev. of Nuc. and Part. Science*, **51**, 53 (2001).

[35] M. Bender, P.-H. Heenen and P.-G. Reinhard, *Rev. Mod. Phys.*, **75**, 121 (2003).

[36] W. H. Dickhoff and D. Van Neck, *Many-Body Theory Exposed!, 2nd edition*, World Scientific, New Jersey (2008).

[37] F. Perey and B. Buck, *Nucl. Phys.*, **32**, 353 (1962).

[38] H. Fiedeldey, *Nucl. Phys.*, **77**, 149 (1966).

[39] J. W. Negele and K. Yazaki, *Phys. Rev. Lett.*, **47**, 71 (1981).

[40] A. Nadasen *et al.*, *Phys. Rev. C*, **23**, 1023 (1981).

[41] B. A. Brown, S. E. Massen and P. E. Hodgson, *J. Phys. G: Nucl. Phys.*, **5**, 1655 (1979).

[42] G. Jacob and T. A. J. Maris, *Rev. Mod. Phys.*, **38**, 121 (1966).

[43] G. Jacob and T. A. J. Maris, *Rev. Mod. Phys.*, **45**, 6 (1973).

[44] S. Frullani and J. Mougey, *Adv. Nucl. Phys.*, **14**, 1 (1984).

[45] C. Barbieri and W. H. Dickhoff, *Phys. Rev. C*, **63**, 034313 (2001).

[46] C. Barbieri and W. H. Dickhoff, *Phys. Rev. C*, **65**, 064313 (2002).

[47] J. Mougey, M. Bernheim, A. Bussiére, A. Gillebert, P. X. Ho, M. Priou, D. Royer, I. Sick and G. Wagner, *Nucl. Phys.*, **A262**, 461 (1976).

[48] H. de Vries, C. W. de Jager and C. de Vries, *At. Data Nucl. Data Tables*, **36**, 495 (1987).

[49] I. Sick *et al.*, *Phys. Lett.*, **88B**, 245 (1979).

[50] H. Müther and W. H. Dickhoff, *Phys. Rev. C*, **49**, R17 (1994).

[51] A. Polls, H. Müther and W. H. Dickhoff, *Nucl. Phys.*, **A594**, 117 (1995).

[52] D. Rohe *et al.*, *Phys. Rev. Lett.*, **93**, 182501 (2004).

[53] H. Müther and I. Sick, *Phys. Rev. C*, **70**, 041301(R) (2004).

[54] A. M. Lane, *Nucl. Phys.*, **35**, 676 (1962).

[55] R. Shane, Ph.D. thesis, Washington University in St. Louis (2011).

[56] A. Gade *et al.*, *Phys. Rev. C*, **77**, 044306 (2008).

[57] O. Jensen *et al.*, *Phys. Rev. Lett.*, **107**, 032501 (2011).

[58] G. Hagen, T. Papenbrock and M. Hjorth-Jensen, *Phys. Rev. Lett.*, **104**, 182501 (2010).

[59] R. Morlock, *Phys. Rev. Lett.*, **79**, 3837 (1997).

[60] M. Waroquier, J. Sau, K. Heyde, P. Van Isacker and H. Vincx, *Phys. Rev. C*, **19**, 1983 (1979).

[61] M. Belleguic *et al.*, *Phys. Rev. C*, **72**, 054316 (2005).

[62] K. L. Jones *et al.*, *Nature Letters*, **465**, 454 (2010).

[63] A. Gade *et al.*, *Phys. Rev. C*, **77**, 044306 (2008).

[64] T. Uesaka *et al.*, *Nucl. Instrum. Methods Phys. Res.*, **Sect. A 526**, 186 (2004).

[65] A. H. Wuosmaa *et al.*, *Phys. Rev. Lett.*, **105**, 132501 (2010).

[66] J. Lee *et al.*, *Phys. Rev. Lett.*, **104**, 112701 (2010).

[67] J. Lee *et al.*, *Phys. Rev. C*, **83**, 014606 (2011).

[68] R. C. Johnson and P. J. R. Soper, *Phys. Rev. C*, **1**, 976 (1970).

[69] R. C. Johnson and P. C. Tandy, *Nucl. Phys. A*, **235**, 56 (1974).

[70] F. M. Nunes and A. Deltuva, *Phys. Rev. C*, **84**, 034607 (2011).

[71] R. V. Reid, *Ann. Phys. (N.Y.)*, **50**, 411 (1968).

[72] M. Igarashi *et al.*, computer program TWOFNR (version, 2008).

[73] I. J. Thompson, *Comput. Phys. Rep.*, **7**, 167 (1988).

[74] F. J. E. et. al., *Nucl. Phys. A*, **506**, 159 (1990).

[75] K. H. et. al, *Nucl. Phys. A*, **419**, 530 (1984).

[76] J. Rapaport, A. Sperduto and M. Salomaa, *Nucl. Phys. A*, **197**, 337 (1972).

[77] W. D. Metz *et al.*, *Phys. Rev. C*, **12**, 827 (1975).

[78] Y. Uozumi *et al.*, *Nucl. Phys. A*, **576**, 123 (1994).

[79] G. M. Crawley, B. V. N. Rao and D. L. Powell, *Nucl. Phys. A*, **112**, 223 (1968).

[80] D. G. Kovar, N. Stein and C. K. Bockelman, *Nucl. Phys. A*, **231**, 266 (1974).

[81] J. Lee *et al.*, *Phys. Rev. C*, 064320 (2007).

[82] D. Y. Pang, F. M. Nuñes and A. M. Mukhamedzhanov, *Phys. Rev. C*, **75**, 024601 (2007).

[83] F. Capuzzi and C. Mahaux, *Ann. Phys.*, **245**, 147 (1996).

[84] J. Escher and B. K. Jennings, *Phys. Rev. C*, **66**, 034313 (2002).

[85] C. Barbieri, D. Van Neck and W. H. Dickhoff, *Phys. Rev. A*, **76**, 052503 (2007).

[86] C. Barbieri and M. Hjorth-Jensen, *Phys. Rev. C*, **79**, 064313 (2009).

[87] C. Barbieri and L. Lapikás, *Phys. Rev. C*, **70**, 054612 (2004).

[88] G. E. Brown and M. Rho, *Nucl. Phys.*, **A372**, 397 (1981).

[89] G. W. Greenlees, G. J. Pyle and Y. C. Tang, *Phys. Rev.*, **171**, 1115 (1968).

[90] R. B. Wiringa, V. G. J. Stoks and R. Schiavilla, *Phys. Rev. C*, **51**, 38 (1995).

[91] D. R. Entem and R. Machleidt, *Phys. Rev. C*, **68**, 041001 (2003).

[92] N. K. Timofeyuk, *Phys. Rev. Lett.*, **103**, 242501 (2009).

[93] C. Barbieri, in F. Cerutti and A. Ferrari (editors), *12th International Conference on Nuclear Reaction Mechanisms*, CERN Proceedings, Geneva (2010), volume 001, 137, iSBN: 9789290833390; arXiv:0909.0336.

[94] F. M. Nunes, A. Deltuva and J. Hong, *Phys. Rev. C.*, **83**, 034610 (2011).

[95] T. Frick, H. Müther, A. Rios, A. Polls and A. Ramos, *Phys. Rev. C*, **71**, 014313 (2005).

[96] A. Rios, A. Polls and W. H. Dickhoff, *Phys. Rev. C*, **79**, 064308 (2009).

[97] T. Otsuka, T. Suzuki, R. Fujimoto, H. Grawe and Y. Akaishi, *Phys. Rev. Lett.*, **95**, 232502 (2005).

[98] D. Bonatsos and H. Müther, *Nucl. Phys.*, **A496**, 23 (1989).

[99] M. Borromeo, D. Bonatsos, H. Müther and A. Polls, *Nucl. Phys.*, **A539**, 189 (1992).

[100] R. Machleidt, F. Sammarruca and Y. Song, *Phys. Rev. C*, **53**, R1483 (1996).

[101] R. Machleidt, *Phys. Rev. C*, **63**, 024001 (2001).

[102] R. Machleidt, *Adv. Nucl. Phys.*, **19**, 1 (1989).

[103] A. Ramos, A. Polls and W. H. Dickhoff, *Nucl. Phys.*, **A503**, 1 (1989).

[104] L. Zamick, D. C. Zheng and H. Müther, *Phys. Rev. C*, **45**, 2763 (1992).

[105] S. C. Pieper and V. R. Pandharipande, *Phys. Rev. Lett.*, **70**, 2541 (1993).

[106] G. J. Kramer *et al.*, *Phys. Lett. B*, **227**, 199 (1989).

[107] L. Schäfer and H. Weidenmüller, *Nucl. Phys.*, **A174**, 1 (1971).

[108] D. S. Lewart, V. R. Pandharipande and S. C. Pieper, *Phys. Rev. B*, **37**, 4950 (1988).

[109] F. Mazzanti, A. Polls, J. Boronat and J. Casulleras, *Phys. Rev. Lett.*, **92**, 085301 (2004).

[110] G. Hagen, T. Papenbrock, D. J. Dean and M. Hjorth-Jensen, *Phys. Rev. Lett.*, **101**, 092502 (2008).

[111] S. Fujii, R. Okamoto and K. Suzuki, *Phys. Rev. Lett.*, **103**, 182501 (2009).